On the non-normality and sensitivity of the linear stability equations in boundary layer flow

bi-orthogonality, pseudospectra and mode sensitivity

On the non-normality and sensitivity of the linear stability equations in boundary layer flow

bi-orthogonality, pseudospectra and mode sensitivity

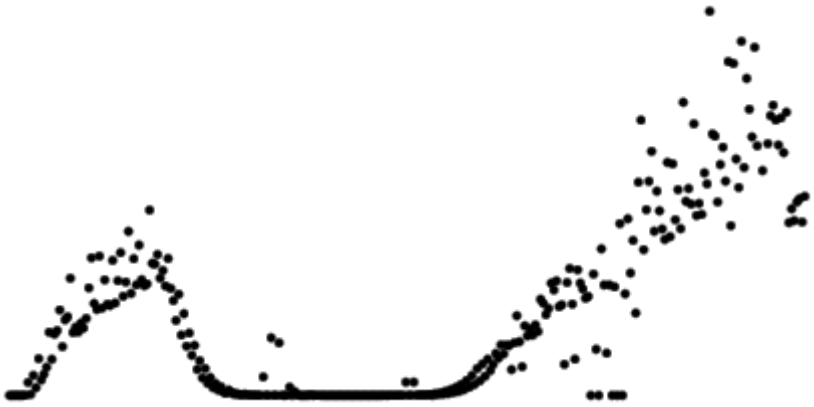

M.Sc. Thesis

by

F.J.M. Kessels

Daily supervisor:

Dr. ir. K. J. Groot

Adviser: Dr. ir. B. W. van Oudheusden

”Those who find it worthy of remark that the word ’eigenvalue’ is a blend of two languages may take pleasure in noting that ’pseudo-eigenvalue’, for better or worse, is a combination of three”.

L.N. Trefethen

Contents

1

Introduction

1.1. On topic and motivation

Linear Stability Theory (LST) is concerned with the analysis of small-amplitude perturbations as superimposed on base flows over or through certain geometries, and is used to study laminar-to-turbulent transition. This transition from laminar to turbulent flow typically originates from the onset of instabilities in the laminar flow. It is to that end that LST has been employed to provide – e.g. users of the e^N-method ([28], [22]) with – a first indication of transition through mode amplification determined by the eigenvalues.

The growth 'contained' in just the eigenvalues is however incomplete for most shear force driven flows [26]. For example, the predicted onset of instability from eigenvalues analyses did not match the onset of instability observed in experiments for a Couette, Poiseuille or a Blasius boundary layer flow [26]. Notably, for the Couette flow the eigenvalues predicted a stable flow [17], whereas experimental data indicated that transition would occur even for relatively low Reynolds numbers [10, 24]. Originally, it was thought that the non-linear terms, dropped from the linearised equations, should then be investigated to explain for this difference. Linear algebra indicates however that this discrepancy may also be attributed to growth contained in the eigenvectors: even if the eigenvalues dictate a stable regime, "*inputs [...] may be amplified by arbitrarily large factors if the eigenfunctions are not orthogonal to one another*" [26]. LST could be used to describe this algebraic (i.e. transient) growth due to the non-normality of the system [21]. Transient growth in this regard relates to the *short-time* behaviour of the LST operator. Such transient growth may occur even if the eigenvalues predict stable decay of any perturbation, as exemplified by the Couette flow eigenvalue spectrum [17]. Whilst this is interesting from a laminar-turbulent transitional flow perspective, the non-normality of the system does bear complications for the analyst. Firstly, the set of eigenmodes is not orthogonal, which complicates further response analyses. Secondly, as noted by Schmid et al. [21], the non-normality of the operator may result in large sensitivity of eigenvalues to small perturbations of the operator. Schmid et al. [21] even concluded that as a result of non-normality "*the study of the sensitivity of the spectra of hydrodynamic stability operators is as essential as the study of their spectra alone*".

1.2. Aim of the research

As the eigenvectors of the LST operators are non-orthogonal, (1) obtaining further insight into the response to a disturbance, or (2) employing these modes as basis functions in a deterministic approach, or control functions in a feedback loop, is complicated. Inherent to the inner product definition of the adjoint, with its bilinear characteristics, bi-orthogonality relations may be derived for the direct and adjoint sets of eigenvectors [20]. A **first aim** of this work is hence to assess whether we can derive bi-orthogonality relations demonstrating that the adjoint LST eigenvectors are orthogonal to the direct eigenvectors; thereby resolving the non-orthogonality complication.

1

Furthermore, stability results are notoriously sensitive to perturbations (see a.o.[15]). Yet, often the eigenvalue spectra are used to describe system behaviours. In particular, these eigenvalues are used to indicate whether a system would be asymptotically stable or unstable for $t \to \infty$. Consequently, we wish to gain insight into what happens to the eigenvalue spectrum of the current LST operators for boundary layer flow when presented with a (matrix) perturbation. In practice these might be perturbations that arise due to e.g. numerical error or errors in the input data. Numerical errors may, for example, be related to generic operator perturbations of a certain order of accuracy, whilst measurement errors could be related to systematic deviations in a streamwise velocity base flow profile.

In [5] the required accuracy of a basic state is investigated so as to ensure a certain order of accuracy of the stability results. In more detail, they discuss the ramifications with regards to the propagation of numerical errors into the stability results. For which the numerical errors were related to the (convergence of the) numerical schemes used to obtain this basic state. In this work we wish to take this one step further, and as such a **second aim** is to determine the sensitivity of the compressible and incompressible LST operators to specific perturbations in the base flow profile. Or put differently: we wish to investigate *how* the eigenvalue spectrum of the LST operator in the TU Delft stability code is affected by specific perturbations in the base flow profile.

Scope: The use of LST is mainly restricted to the types of responses associated with amplification mechanisms. We will further restrict this scope to two-dimensional flows and streamwise instability. This is in line with the Squire theorem which states that two-dimensional wave amplification will start at a Reynolds number lower than any 3D wave [1], for which the Tollmien-Schlichting direction can be considered the most unstable direction. Arnal & Casalis [1] also indicate that transition can be assumed to be triggered either by streamwise or crossflow instability.

1.3. Physics of transitional flow

Transition pertains to the region or process in which a laminar flow evolves into a chaotic turbulent flow. This drastically changes the flow's characteristics, e.g. the skin friction for a flow over an aerofoil.

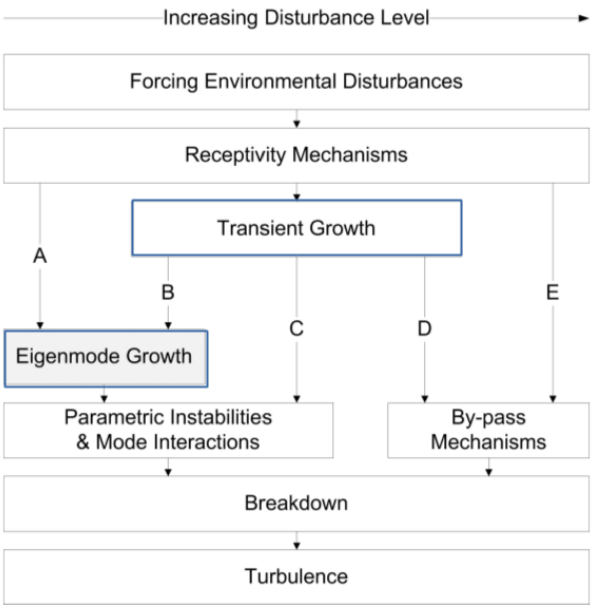

Figure 1.1: Graphic showing the stages of transition, after [16] (in [4]). Those mechanisms that can be represented by LST are highlighted in blue.

In transitioning from laminar to turbulent flow, it is generally thought that the flow evolves

through a number of flow states [16]. Each of theses states represents increased complexity of the flow and its inherent parameters. This work only relates to the early stages of transition as described by the eigenmode growth and transient growth mechanisms, which occur before the onset of secondary instabilities. In Figure 1.1 the stages of transition for a wall-bounded flow are represented graphically [16]. The transition paths A-E all start with a disturbance of a certain amplitude. This disturbance is then entrained in the boundary layer. The process by which disturbances are entrained into the boundary layer and may generate instability waves is called *boundary layer receptivity*. The topic of receptivity is not considered here, but it is important to remember that receptivity forms a starting point for the transition stages related to LST. Additionally, keep in mind that the adjoint eigenfunctions allow the projection of a given disturbance onto the eigenbasis. Therefore the approach used here may be deployed for receptivity analyses. See Saric [18], Kerschen [7] or Morkovin [12]) for more information on boundary layer receptivity. For example, Kerschen [7] makes a distinction between natural and forced disturbances, their intrinsic wavelengths and the physical processes involved.

The amplitude of a disturbance as mentioned previously is an important consideration in LST (and also Figure 1.1). For example, after experiencing transient growth, the transition would follow path B only if the disturbance remains of $\mathcal{O}(\epsilon)$. Should the disturbance grow such that it is of $\mathcal{O}(1)$, it could trigger non-linear bypass mechanisms. Similarly, if an initial disturbance entrained in the boundary layer is large enough, then by-pass mechanisms would be at play rather than eigenmode growth. This is a consideration to keep in mind when imposing perturbations on e.g. a base flow profile. See [13] for more information on bypass mechanisms and see Reshotko [16] and/or Pinna [14] for a more detailed description of the transition paths presented in Figure 1.1.

1.4. Non-normality

Formally a matrix may be considered normal if it commutes with its adjoint:

$$\mathbf{A}^{+}\mathbf{A} = \mathbf{A}\mathbf{A}^{+} \tag{1.1}$$

The adjoint matrix $\mathbf{A}^{+}$ is here defined as the complex conjugate transpose, or the hermitian, of $\mathbf{A}$. That is, $\mathbf{A}^{+} = \bar{\mathbf{A}^{\mathbf{T}}}$. Equivalently, a matrix $\mathbf{A}$ is normal if, and only if, it has an orthonormal basis of eigenvectors. The LST operators do not meet this criterion. It is through these non-orthogonal eigenvectors that the LST results may exhibit transient growth.

In analogy to the well-known three-axes X,Y,Z coordinate system, having an orthogonal basis of eigenvectors would yield a coordinate system that could perfectly describe the dynamical system through scalar amplification along the individual axes. The non-orthogonality yields a coordinate system with eigenvectors that are oblique. In our X,Y,Z example two vectors would not e.g. span the X-Y plane, but both vectors could for example lie within this original X-Y plane. Casually speaking this may lead to a certain 'overlap' in information when describing the dynamical system in terms of the eigenvectors. Additionally, if in a asymptotically stable system one eigenvector decays at a rate different from an eigenvector oblique to it, the resultant of the 'parallelogram' spanned by the eigenvectors may yield short-term growth: transient growth. See also the sketch of Schmid & Henningson [20] in Figure 1.2 which shows this aspect.

The adjoint eigenvectors are known to form a set of vectors that is so-called bi-orthogonal to the direct eigenvectors. Examples of this are the bi-orthogonality relations for the Orr-Sommerfeld equations by Schmid & Henningson in [20]. They derived an orthogality weight for which the two sets of eigenvectors would be orthogonal.

Measures to determine the (extent of) non-normality of a matrix include computing the numerical range, pseudospectra or the departure from normality (a.o. [27]). The relative non-normality of an operator could be described from the definition of normality:

$$||\mathbf{A}^{+}\mathbf{A} - \mathbf{A}\mathbf{A}^{+}|| \tag{1.2}$$

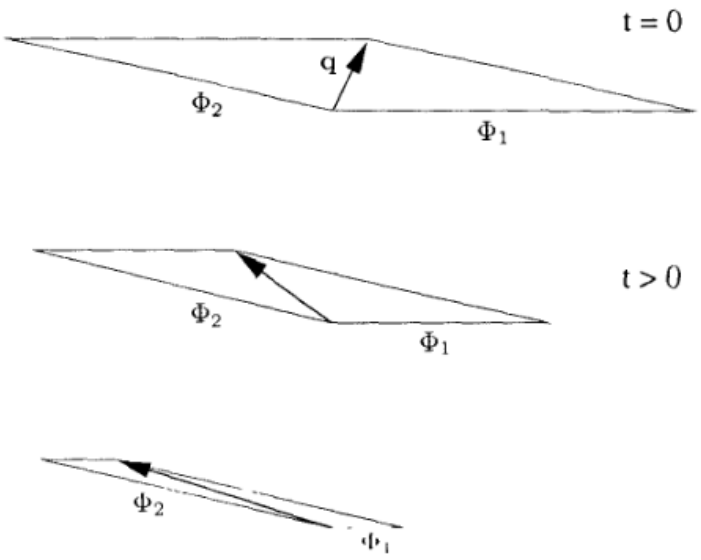

Figure 1.2: Sketch from Schmid & Henningson in [20], indicating the process of transient growth for non-orthogonal eigenvectors.

Alternatively a measure of non-normality could be obtained using the Frobenius norm ([2]):

$$dep_F(\mathbf{A}) = \sqrt{||\mathbf{A}||_F^2 - \sum_{j=1}^{n} |\lambda_j|^2} \tag{1.3}$$

However these scalar measures are found not to be of much use in practice [2]. The numerical range and pseudospectra on the other hand are generally considered to be effective tools to study the non-normality of the system, as exemplified by research by a.o. [27], [21] and [15].

1.4.1. Numerical range

Essentially the numerical range provides a set of values in the complex plane that replaces the eigenvalue spectrum. This new set $W(\mathbf{A})$ is the set of all the Rayleigh quotient eigenvalue estimates. Formally:

$$W(\mathbf{A}) = x^* \mathbf{A} x : ||x|| = 1 \tag{1.4}$$

for which the original eigenvalue spectrum forms a subset of $W(\mathbf{A})$. Whilst the numerical range does provide interesting information with regards to e.g. the numerical abscissa and hence (in)stability information of the system; the numerical range itself can be rather large, especially for systems like the LST operators [2]. Beyond the numerical abscissa this then leaves relatively little room for interpretation or analysis of the resulting spectrum due to the sheer size of the range.

1.4.2. Pseudospectra

The pseudospectrum of matrix $\mathbf{A}$ may be defined by the set:

$$\sigma_\epsilon = z \in \mathbb{C} : z \in \sigma(\mathbf{A} + \mathbf{E}) \quad \text{for some} \quad \mathbf{E} \in \mathbb{C}^{n \times n} \quad \text{with} \quad ||\mathbf{E}|| < \epsilon \tag{1.5}$$

for which the original eigenvalue spectrum forms a subset of $\sigma_\epsilon(\mathbf{A})$.
For the generalised eigenvalue problem the pseudospectrum may be defined as ([3, 2]):

$$\sigma_\epsilon(\mathbf{A}, \mathbf{B}) = z \in \mathbb{C} : z \in \sigma(\mathbf{A} + \mathbf{E_0})x = z(\mathbf{A} + \mathbf{E_1})x \quad \text{for some} \quad x \neq 0 \quad \text{with} \quad ||\mathbf{E}||_0 < \epsilon\alpha_0, ||\mathbf{E}||_1 < \epsilon\alpha_1 \tag{1.6}$$

A well-known application to compute pseudospectra is 'Eigtool', as developed by Thomas G. Wright at the Oxford University Computing Laboratory [29] and which makes use of algorithms described in [25, 27]. Eigtool is a MATLAB package for computing pseudospectra of both dense and sparse matrices. Unfortunately, the tool may only be used for a single operator $\mathbf{A}$ and cannot compute spectra for a generalised eigenvalue problem (GEP) such as for the LST operators.

Spanning a d-dimensonal invariant subspace may yield a single matrix $U'^{*}\mathbf{A}_{eigtool}U$ from the dominant eigenvalues of the GEP's $\mathbf{A}, \mathbf{B}$ matrices and an orthonormal basis U constructed from the eigenvectors of the d-dimensional subspace. However doing so relies on being able to invert $\mathbf{B}$ and/or to compute $\mathbf{A}_{eigtool} = \mathbf{B}\backslash\mathbf{A}$ in Matlab, which is infeasible given the (near) singularity and ill-conditioning of the LST operators.

1.5. Method used to approach the objectives

Recall that the aims of the thesis are to:

1 assess whether we can derive bi-orthogonality relations such that the adjoint LST eigenvectors are orthogonal to the direct eigenvectors, for both the compressible and incompressible LST equations

2 determine how the eigenvalue spectrum of the LST operator is affected by specific perturbations in the base flow profile

Taking into account the limitations described in the previous section for the LST equations, we will:

I Derive the adjoint system for the incompressible and compressible LST equations

II Derive, implement and assess bi-orthogonality relations using the adjoint eigenvectors

III Compute pseudospectra for the incompressible and compressible LST equations for a perturbed generalised eigenvalue problem $(A + E)\mathbf{q} = \omega(B + E)\mathbf{q}$, with $E \sim \mathcal{O}(\epsilon)$

IV Compute eigenspectra for the incompressible and compressible LST equations for a perturbed streamwise velocity base flow profile $u(y) + E(y)$, with $E \quad \mathcal{O}(\epsilon)$

1.6. Lay-out of the thesis

In this thesis we will first discuss Linear Stability Theory, the governing equations ánd solving those equations in Chapter 2. Chapter 3 will present the derivations of the adjoint LST operators, compressible and incompressible, to be used for the bi-orthogonality relations that are derived in Chapter 4. Chapter 4 will further discuss the numerical implementation of said biorthogonality relations for the compressible and incompressible LST equations. Subsequently, in Chapter 5 the 'original' temporal eigenvalue spectra will be characterised, and pseudospectra will be presented for a perturbed generalised eigenvalue problem for both the incompressible and compressible LST operators, respectively. Chapter 6 will present temporal eigenspectra of the incompressible and compressible LST operators for perturbations of the streamwise velocity base flow profile. These perturbations will be imposed (1) on the entire profile, (2) in the wall region, (3) in a middle region and (4) on the top-layer at the edge of the flow profile. Finally, we will present our conclusions and recommendations in Chapter 7.

2

Linear Stability Theory

In this chapter we will first briefly discuss the basic premise of Linear Stability Theory in Section 2.1. The governing equations and the inherent simplifications are presented in Section 2.2. How we solve those equations is dealt with in Sections 2.3 and 2.4.

2.1. Basic premise

The basic premise of stability theory lies in the decomposition of a base flow plus a perturbation of $\mathcal{O}(\epsilon)$ which is introduced into the governing equations (where $\epsilon << 1$). Here, both the complete expression and the base flow equations satisfy the governing equations. Which consequently allows for the subtraction of the terms involving the base flow quantities only(system of $\mathcal{O}(1)$), thereby yielding the perturbation equations (system of $\mathcal{O}(\epsilon)$). The complete system is by many reported as the 'mean-plus-perturbation equations [4]. Note that it is only *after* linearisation of the perturbation equations that these are only applicable up to ϵ away from the equilibrium solution under investigation.
Depending on the flow situation the base flow is – or can be assumed to be – (in)homogeneous in certain directions, which affects the subsequent analysis in that the homogeneous direction(s) may then be evaluated in a spectral manner, whereas the inhomogeneous directions require a differential analysis. The problem can be Fourier transformed.

For a flow inhomogeneous in only one direction, and with a base flow independent of time (e.g. a Blasius developing boundary layer, albeit analysed far from the leading edge of the plate) we arrive at the well-known LST Ansatz (through Fourier analysis) for the perturbation q':

$$q'(x,y,z,t) = \tilde{q}(y)e^{i\Theta(x,z,t)} + c.c. \tag{2.1}$$

which in our developing boundary layer example represents a parallel flow evaluated locally. Assuming a solution of the form $e^{i\Theta(x,z,t)}$ reduces the initial-boundary-value problem to an eigenvalue problem (EVP).

2.2. Stability equations

The stability equations are often set up as a spatial problem or as a temporal problem. For a spatial problem the frequency ω is real and given and the EVP is solved for the complex spatial wavenumber α. For a temporal problem the spatial wavenumber α is real and given and the EVP is solved for the complex frequency ω. It is of course not necessary to choose for either problem, as the 'full' problem would allow both the spatial and temporal modes to grow/decay in time. In this work we will restrict ourselves to the temporal problem, in light of its analogy with the stability issue of flow disturbances in time, e.g. the growth of the Tollmien-Schlichting mode over time.

The simplifications for the LST stability equations we will use in this project – obtained by means of the Ansatz as described in 2.1 – amount to *linearised* equations, evaluated *locally*, spectral treatment (i.e. *homogeneous*) in all directions (and time) except for the differentially evaluated (i.e. *inhomogeneous*) y-direction.

Below the corresponding compressible LST stability equations are given – in Cartesian coordinates – for compressible continuity, momentum and energy [4, 14].

Continuity:

$$\begin{aligned} &-\frac{i\,\beta\,\tilde{T}\,\overline{P}\,\overline{W}}{\overline{T}} + i\,\beta\,\tilde{p}\,\overline{W} - \frac{i\,\alpha\,\tilde{T}\,\overline{P}\,\overline{U}}{\overline{T}} + i\,\alpha\,\tilde{p}\,\overline{U} - \frac{\tilde{v}\,\overline{P}\,\overline{T}_y}{\overline{T}} \\ &+\frac{i\,\omega\,\tilde{T}\,\overline{P}}{\overline{T}} - i\,\omega\,\tilde{p} + \tilde{v}\,\overline{P}_y + i\,\beta\,\tilde{w}\,\overline{P} + \tilde{v}_y\,\overline{P} + i\,\alpha\,\tilde{u}\,\overline{P} = 0 \end{aligned} \tag{2.2}$$

x-Momentum:

$$\begin{aligned} &\frac{i\,\beta\,\gamma\,\tilde{u}\,M^2\,\overline{P}\,\overline{W}}{\overline{T}} + \frac{\gamma\,\tilde{v}\,M^2\,\overline{P}\,\overline{U}_y}{\overline{T}} + \frac{i\,\alpha\,\gamma\,\tilde{u}\,M^2\,\overline{P}\,\overline{U}}{\overline{T}} - \frac{i\,\gamma\,\omega\,\tilde{u}\,M^2\,\overline{P}}{\overline{T}} = \frac{\tilde{T}\,\overline{\mu}_{\overline{T}}\,\overline{U}_{y\,y}}{Re} \\ &+\frac{\tilde{T}\,\overline{\mu}_{\overline{T}\,\overline{T}}\,\overline{T}_y\,\overline{U}_y}{Re} + \frac{\tilde{T}_y\,\overline{\mu}_{\overline{T}}\,\overline{U}_y}{Re} + \frac{i\,\alpha\,\tilde{v}\,\overline{\mu}_{\overline{T}}\,\overline{T}_y}{Re} + \frac{\tilde{u}_y\,\overline{\mu}_{\overline{T}}\,\overline{T}_y}{Re} - i\,\alpha\,\tilde{p} - \frac{\alpha\,\beta\,\tilde{w}\,\overline{\mu}}{Re} + \frac{i\,\alpha\,\tilde{v}_y\,\overline{\mu}}{Re} \\ &+\frac{\tilde{u}_{y\,y}\,\overline{\mu}}{Re} - \frac{\beta^2\,\tilde{u}\,\overline{\mu}}{Re} - \frac{2\,\alpha^2\,\tilde{u}\,\overline{\mu}}{Re} - \frac{\alpha\,\beta\,\tilde{w}\,\overline{\lambda}}{Re} + \frac{i\,\alpha\,\tilde{v}_y\,\overline{\lambda}}{Re} - \frac{\alpha^2\,\tilde{u}\,\overline{\lambda}}{Re} \end{aligned} \tag{2.3}$$

y-Momentum:

$$\begin{aligned} &\frac{i\,\beta\,\gamma\,\tilde{v}\,M^2\,\overline{P}\,\overline{W}}{\overline{T}} + \frac{i\,\alpha\,\gamma\,\tilde{v}\,M^2\,\overline{P}\,\overline{U}}{\overline{T}} - \frac{i\,\gamma\,\omega\,\tilde{v}\,M^2\,\overline{P}}{\overline{T}} = \frac{i\,\beta\,\tilde{T}\,\overline{\mu}_{\overline{T}}\,\overline{W}_y}{Re} + \frac{i\,\alpha\,\tilde{T}\,\overline{\mu}_{\overline{T}}\,\overline{U}_y}{Re} \\ &+\frac{2\,\tilde{v}_y\,\overline{\mu}_{\overline{T}}\,\overline{T}_y}{Re} + \frac{i\,\beta\,\tilde{w}\,\overline{\lambda}_{\overline{T}}\,\overline{T}_y}{Re} + \frac{\tilde{v}_y\,\overline{\lambda}_{\overline{T}}\,\overline{T}_y}{Re} + \frac{i\,\alpha\,\tilde{u}\,\overline{\lambda}_{\overline{T}}\,\overline{T}_y}{Re} - \tilde{p}_y + \frac{i\,\beta\,\tilde{w}_y\,\overline{\mu}}{Re} + \frac{2\,\tilde{v}_{y\,y}\,\overline{\mu}}{Re} \\ &-\frac{\beta^2\,\tilde{v}\,\overline{\mu}}{Re} - \frac{\alpha^2\,\tilde{v}\,\overline{\mu}}{Re} + \frac{i\,\alpha\,\tilde{u}_y\,\overline{\mu}}{Re} + \frac{i\,\beta\,\tilde{w}_y\,\overline{\lambda}}{Re} + \frac{\tilde{v}_{y\,y}\,\overline{\lambda}}{Re} + \frac{i\,\alpha\,\tilde{u}_y\,\overline{\lambda}}{Re} \end{aligned} \tag{2.4}$$

z-Momentum:

$$\begin{aligned} &\frac{\gamma\,\tilde{v}\,M^2\,\overline{P}\,\overline{W}_y}{\overline{T}} + \frac{i\,\beta\,\gamma\,\tilde{w}\,M^2\,\overline{P}\,\overline{W}}{\overline{T}} + \frac{i\,\alpha\,\gamma\,\tilde{w}\,M^2\,\overline{P}\,\overline{U}}{\overline{T}} - \frac{i\,\gamma\,\omega\,\tilde{w}\,M^2\,\overline{P}}{\overline{T}} = \frac{\tilde{T}\,\overline{\mu}_{\overline{T}}\,\overline{W}_{y\,y}}{Re} \\ &+\frac{\tilde{T}\,\overline{\mu}_{\overline{T}\,\overline{T}}\,\overline{T}_y\,\overline{W}_y}{Re} + \frac{\tilde{T}_y\,\overline{\mu}_{\overline{T}}\,\overline{W}_y}{Re} + \frac{\tilde{w}_y\,\overline{\mu}_{\overline{T}}\,\overline{T}_y}{Re} + \frac{i\,\beta\,\tilde{v}\,\overline{\mu}_{\overline{T}}\,\overline{T}_y}{Re} - i\,\beta\,\tilde{p} + \frac{\tilde{w}_{y\,y}\,\overline{\mu}}{Re} - \frac{2\,\beta^2\,\tilde{w}\,\overline{\mu}}{Re} \\ &-\frac{\alpha^2\,\tilde{w}\,\overline{\mu}}{Re} + \frac{i\,\beta\,\tilde{v}_y\,\overline{\mu}}{Re} - \frac{\alpha\,\beta\,\tilde{u}\,\overline{\mu}}{Re} - \frac{\beta^2\,\tilde{w}\,\overline{\lambda}}{Re} + \frac{i\,\beta\,\tilde{v}_y\,\overline{\lambda}}{Re} - \frac{\alpha\,\beta\,\tilde{u}\,\overline{\lambda}}{Re} \end{aligned} \tag{2.5}$$

Energy:

$$\begin{aligned}
&\frac{i\,\beta\,\gamma\,\tilde{T}\,M^2\,\overline{P}\,\overline{W}}{\overline{T}} + \frac{i\,\alpha\,\gamma\,\tilde{T}\,M^2\,\overline{P}\,\overline{U}}{\overline{T}} + \frac{\gamma\,\tilde{v}\,M^2\,\overline{P}\,\overline{T}_y}{\overline{T}} - \frac{i\,\gamma\,\omega\,\tilde{T}\,M^2\,\overline{P}}{\overline{T}} \\
&= \frac{(\gamma-1)\,\tilde{T}\,M^2\,\overline{\mu}_{\overline{T}}\left(\overline{W}_y\right)^2}{Re} + \frac{2\,(\gamma-1)\,\tilde{w}_y\,M^2\,\overline{\mu}\,\overline{W}_y}{Re} + \frac{2\,i\,\beta\,(\gamma-1)\,\tilde{v}\,M^2\,\overline{\mu}\,\overline{W}_y}{Re} \\
&+ i\,\beta\,(\gamma-1)\,M^2\,\tilde{p}\,\overline{W} + \frac{(\gamma-1)\,\tilde{T}\,M^2\,\overline{\mu}_{\overline{T}}\left(\overline{U}_y\right)^2}{Re} + \frac{2\,i\,\alpha\,(\gamma-1)\,\tilde{v}\,M^2\,\overline{\mu}\,\overline{U}_y}{Re} \\
&+ \frac{2\,(\gamma-1)\,\tilde{u}_y\,M^2\,\overline{\mu}\,\overline{U}_y}{Re} + i\,\alpha\,(\gamma-1)\,M^2\,\tilde{p}\,\overline{U} + \frac{\tilde{T}\,\overline{k}_{\overline{T}}\,\overline{T}_{y\,y}}{Pr\,Re} + \frac{\tilde{T}\,\overline{k}_{\overline{T}\,\overline{T}}\left(\overline{T}_y\right)^2}{Pr\,Re} \\
&+ \frac{2\,\tilde{T}_y\,\overline{k}_{\overline{T}}\,\overline{T}_y}{Pr\,Re} + \frac{\tilde{T}_{y\,y}\,\overline{k}}{Pr\,Re} - \frac{\beta^2\,\tilde{T}\,\overline{k}}{Pr\,Re} - \frac{\alpha^2\,\tilde{T}\,\overline{k}}{Pr\,Re} \\
&- i\,(\gamma-1)\,\omega\,M^2\,\tilde{p} + (\gamma-1)\,\tilde{v}\,M^2\,\overline{P}_y
\end{aligned} \tag{2.6}$$

For these compressible equations a calorically perfect gas is assumed and the transport coefficients λ, μ and k are considered to be functions of temperature. Sutherland's law is applied for the first coefficient of viscosity. Note that in the TU Delft stability code the continuity equation as presented above is divided by $\bar{\rho} = \gamma M^2 \bar{p}/\bar{T}$ to improve the Frobenius norm of the LST operator [5].

Homogeneous boundary conditions are usually applied for the perturbation amplitudes $\tilde{u}$, $\tilde{v}$, $\tilde{w}$ both at the wall and at the free-stream boundary [4, 14, 5]. Note that the latter is due to the choice of the boundary layer flow test case in this work. A compatibility condition may be applied for the pressure perturbation amplitude $\tilde{p}$. For the temperature perturbation, amplitude it is justified to apply a homogeneous boundary condition for unsteady perturbation solutions, $\mathcal{R}(\omega) \neq 0$ [5].

Similarly, the incompressible LST stability equations are given below – in Cartesian coordinates – for incompressible continuity and momentum [4, 14].

Continuity:

$$i\beta\tilde{w} + \tilde{v_y} + i\alpha\tilde{u} = 0 \tag{2.7}$$

x-Momentum:

$$i\beta\tilde{u}\overline{W} + \tilde{v}\overline{U}_y + i\alpha\tilde{u}\overline{U} - i\omega\tilde{u} = -i\alpha\tilde{p} + \frac{\tilde{u}_{yy}}{Re} - \frac{\beta^2\tilde{u}}{Re} - \frac{\alpha^2\tilde{u}}{Re} \tag{2.8}$$

y-Momentum:

$$i\beta\tilde{v}\overline{W} + i\alpha\tilde{v}\overline{U} - i\omega\tilde{v} = -\tilde{p_y} + \frac{\tilde{v}_{yy}}{Re} - \frac{\beta^2\tilde{v}}{Re} - \frac{\alpha^2\tilde{v}}{Re} \tag{2.9}$$

z-Momentum:

$$\tilde{v}\overline{W_y} + i\beta\tilde{w}\overline{W} + i\alpha\tilde{w}\overline{U} - i\omega\tilde{w} = -i\beta\tilde{p} + \frac{\tilde{w}_{yy}}{Re} - \frac{\beta^2\tilde{w}}{Re} - \frac{\alpha^2\tilde{w}}{Re} \tag{2.10}$$

As with the compressible equations homogeneous boundary conditions are usually applied for the perturbation amplitudes $\tilde{u}$, $\tilde{v}$, $\tilde{w}$ both at the wall and at the free-stream boundary [4, 14, 5]. A compatibility condition may be applied for the pressure perturbation amplitude $\tilde{p}$.

2.2.1. Global instability and PSE

In the linear stability equations presented above we only evaluated the y-direction differentially. As a result the solution can only represent inhomogeneous behaviour in the y-direction. The other directions are restricted to modal behaviour. Hence, we essentially have a unidimensional mean flow, and more importantly: unidimensional eigenfunctions. Taking into account a further spatial direction would yield a BiGlobal analysis, in which we basically assess the flow stability in a plane. In a similar vein TriGlobal analysis relates to the flow stability in a volume. Including extra differential spatial directions allows for the representation of more physical phenomena than in the current LST method, e.g. spanwise vorticity for the BiGlobal case. For more information on global instability see Theofilis [23], and for an extensive introduction to BiGlobal analysis and the corresponding equations see [4].

Another main assumption in the LST equations is that of a *local* flow. It is possible to eliminate the *local* assumption and solve the equations by marching in space instead of solving them separately for each location. This approach would constitute Parabolised Stability Equations (PSE) and could be performed irrespective of the choice on differential/spectral directions (e.g. Uni-, Bi- or TriGlobal PSE). Obviously this would increase the accuracy of the representation of the test case, as it allows for the use of the time history of the flow, e.g. curvature of an airfoil suddenly *can* be accounted for.

These more involved analyses are however considered outside the scope of this thesis. Needless to say, improving the accuracy of the analysis and the increased number physical phenomena that can be captured by the BiGlobal/TriGlobal and PSE is indeed very interesting. However it adds a complexity to the equations themselves and an increasing sensitivity to boundary/initial conditions that may cloud the interpretation of the stability results in light of the aims of this study. The effect of the choice of boundary conditions, or even the initial disturbances, is not easily distinguished from the effect of a perturbation imposed deliberately.

2.3. Numerical methods

The stability equations will be solved using the verified TU Delft stability code [5] (originating from [4]). Below we will detail the systems of equations (Section 2.3.1), the discretisation method (Section 2.3.2), and how we will solve the eigenvalue problems. An additional note is included on the spurious modes that can be observed in the stability results of the TU Delft code (Section 2.4.1).

2.3.1. LST operators

The systems of equations following from the governing LST equations are set up as follows, for the generalised eigenvalue problem (GEP) $(\mathbf{A} - \omega\mathbf{B})\tilde{q} = \mathbf{0}$:

Incompressible:

$$\begin{bmatrix} [\text{X-MOMENTUM}] \\ [\text{Y-MOMENTUM}] \\ [\text{Z-MOMENTUM}] \\ [\text{CONTINUITY}] \end{bmatrix} \begin{bmatrix} \tilde{u} \\ \tilde{v} \\ \tilde{w} \\ \tilde{p} \end{bmatrix} = \mathbf{0} \tag{2.11}$$

Compressible:

$$\begin{bmatrix} [\text{X-MOMENTUM}] \\ [\text{Y-MOMENTUM}] \\ [\text{Z-MOMENTUM}] \\ [\text{ENERGY}] \\ [\text{CONTINUITY}] \end{bmatrix} \begin{bmatrix} \tilde{u} \\ \tilde{v} \\ \tilde{w} \\ \tilde{T} \\ \tilde{p} \end{bmatrix} = \mathbf{0} \tag{2.12}$$

The system of equations determined by $(\mathbf{A}-\omega\mathbf{B})$ forms the operator, or function, that acts on the variables defined in $\tilde{q}$.
Note from the stability equations that the temporal EVP $(\mathbf{A}-\omega\mathbf{B})$ yields a 'straight-forward' linear EVP, whilst the spatial EVP would yield a quadratic EVP given the terms α^2. That is: $(\mathbf{A}-\alpha\mathbf{B}-\alpha^2\mathbf{C})=0$. To be able to solve such a polynomial problem would require linearising the system of equations by augmenting it such that we solve for $\tilde{q}_{quadratic}=\begin{bmatrix}\alpha\tilde{q}\\ \tilde{q}\end{bmatrix}$.

For the temporal LST problem in this study homogeneous boundary conditions are applied for the perturbation amplitudes $\tilde{u}$, $\tilde{v}$, $\tilde{w}$ both at the wall and at the free-stream boundary. Using the linearised y-momentum and the pressure gradient term in said y-momentum equation a compatibility condition is applied for the pressure perturbation, which yields the following system of equations (compressible case):

$$\begin{bmatrix}\text{[X-MOMENTUM]}\\ \text{[Y-COMPATIBILITY EDGE]}\\ \text{[Y-MOMENTUM]}\\ \text{[Y-COMPATIBILITY WALL]}\\ \text{[Z-MOMENTUM]}\\ \text{[ENERGY]}\\ \text{[CONTINUITY]}\end{bmatrix}\begin{bmatrix}\tilde{u}\\ \tilde{v}\\ \tilde{w}\\ \tilde{T}\\ \tilde{p}_{\text{edge}}\\ \tilde{p}\\ \tilde{p}_{\text{wall}}\end{bmatrix}=\mathbf{0} \tag{2.13}$$

2.3.2. Chebyshev spectral collocation

The TU Delft stability code employs a Chebyshev spectral collocation method with a set of Gauss-Chebyshev-Lobatto (GCL) nodes, and the mapping introduced by Malik [11].

Spectral collocation essentially uses an expansion of the solution in terms of a finite set of global basis functions. The expansion coefficients are then required to exactly satisfy the differential equation at the collocation nodes in question. This allows for the representation of the derivatives at these nodes. Exactly satisfying the equations at the collocation nodes can be done using a set of discrete delta functions, e.g. Lagrange polynomials.

The main advantage of using a spectral collocation method, as opposed to for example finite differences, is the relatively high accuracy, especially regarding the evaluation of the derivatives. In the spectral collocation method used, the derivative(s) at a certain node are determined using the entire stencil of nodes, whereas e.g. in a finite difference scheme the derivatives are computed using a certain subset of (neighbouring) nodes.

For a more detailed description of the collocation method used see Groot [4]. Or see Hussaini et al. [6] for a review on spectral collocation methods.

2.4. Solving eigenvalue problems

To solve the eigenvalue problems presented by the LST equations we will use the standard function *eig* in Matlab. This function employs the QZ algorithm to determine the full spectrum $\sigma(\mathbf{A},\mathbf{B})$. These results are accurate up to:

$$\epsilon_{eig}=max(\epsilon||\mathbf{A}||_F,||\mathbf{B}||_F) \tag{2.14}$$

This criterion, often referred to as the algorithm precision, may be used to determine whether the spectrum resolved by the QZ algorithm is of the desired accuracy for the Frobenius norm $||\cdot||_F$ and the machine precision ϵ ($\approx 2.2*10^{-16}$ [4]). We will use the above criterion in the subsequent pseudospectra analyses to quantify the reliability of our spectra. When solving the LST EVP for the frequency ω the spectrum (i.e. $\sigma(\mathbf{A},\mathbf{B})$) perturbations may grow exponentially for values of ω for which the imaginary part is positive. Hence, should the spectrum be confined to the lower complex half-plane, the system can be considered linearly stable. In this case small perturbations would decay for $t\to\infty$.

In interpreting the eigenspectrum it is interesting to note that the real phase speed $\mathcal{R}(c)$ of a certain eigenmode ω:

$$\mathcal{R}(c) = \mathcal{R}(\frac{\omega}{\alpha}) \tag{2.15}$$

may be linked to the base flow velocity profile. In matching the real phase speed to the base flow velocity profile it gives an indication of the dominant location of this mode, i.e. the location at which it has its maximum amplitude [20]. For example, for a boundary layer flow those modes with a lower real phase speed may be considered wall modes, and modes for which the real phase speed approaches 1 are dominant in the freestream layer.

Further notes to keep in mind are that due to the non-orthogonality of the eigenvectors for fluid mechanics problems, the eigenspectra may yield regions with random mode behaviour, related to the phenomenon of transient growth [27]. And that the system of eigenvectors resulting from the EVP is only applicable up to ϵ away from the 'current' tangent space in which they reside. For example, to properly include the effects of transient growth, the actual (stable) manifold itself will be required, which yields a non-EVP [4].

2.4.1. Spurious mode behaviours

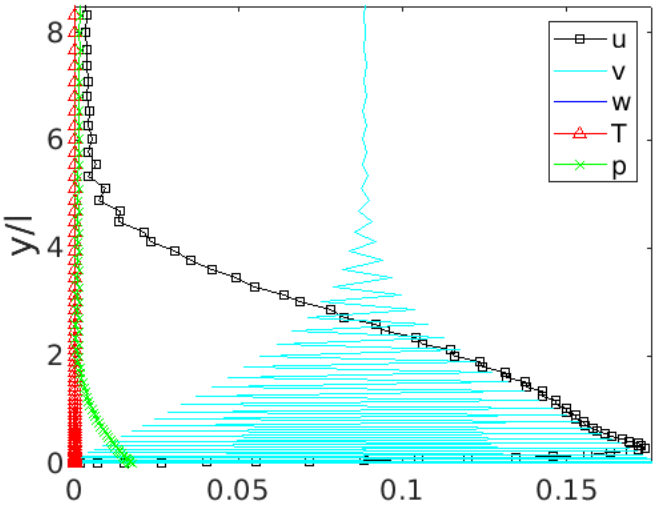

Figure 2.1: Spurious v-mode, $M = 10^{-3}, Re = 580, \alpha = 0.2$

Through solving the discretised LST equations with a compatiblity equation the set $\sigma(\mathbf{A}, \mathbf{B})$ does not solely contain physical modes. Rather, non-physical spurious modes are contained within the set $\sigma(\mathbf{A}, \mathbf{B})$. These are apparent in the normal-velocity perturbation and are characterised by large oscillations between subsequent nodes. See for example the spurious mode in Figure 2.1. The mode effectively becomes a combination of two decoupled mode-shapes with intermittent 'zig-zagging'. Such a spurious mode might perhaps be attributed to the following:

- As a result of the pressure compatibility conditions, the formulation in $\tilde{v}$ remains unconstrained, which leads to odd-even decoupling between the nodes and subsequent non-uniqueness as a result of additive constants [23]
- eigensolver characteristics, i.e. replacing entries below a certain threshold with zeros, thereby affecting the system considerably given that it is highly non-orthogonal

Detection of the non-physical spurious modes is achieved by means of an orthogonal projection of the mode on a general 'zig-zag' pattern to capture the oscillatory content of the $\tilde{v}$-amplitude. These modes are omitted in what follows.

3

Derivations of the adjoint LST operators

In this chapter we will first briefly discuss the definition of an adjoint operator and what adjoint operators might be used for in section 3.1. The derivation of the adjoint operator of the primitive variable formulation of the incompressible LST system is then presented in section 3.2. The adjoint operator derivation of the primitive variable formulation of the compressible LST system is shown in section 3.3.

3.1. Adjoint operators

Formally the adjoint is defined as an operator $\mathcal{L}^+$ such that:

$$(y, \mathcal{L}(x)) = (\mathcal{L}^+(y), x) \qquad \forall x \in X, y \in Y \tag{3.1}$$

for arbitrary vectors x, y, and with the inner product defined as $(u, v) = \int u^* v \quad \mathrm{d}y \in \mathbb{C}^N$. For continuous linear operators the adjoint is generally defined as the matrix $\mathbf{A}^+$ such that:

$$(y, \mathbf{A}x) = (\mathbf{A}^+ y, x) \qquad \forall x, y \in \mathbb{C}^N \text{ and } \mathbf{A}, \mathbf{A}^+ \in \mathbb{C}^{NxN} \tag{3.2}$$

for which – again for arbitrary vectors x, y – the inner product properties dictate that $\mathbf{A}^+ = \mathbf{A}^H$, and $(\mathbf{A}^+)^H = \mathbf{A}$ for constant coefficient matrices $\mathbf{A}$. As such the definition of the adjoint translates to the complex conjugate transpose, or Hermitian transpose, in matrix operations. For cases with non-constant coefficient matrices, due to for example an inhomogeneous direction and hence differential dependency in the operator matrix, the latter equation does not necessarily apply. In that scenario the transposition of the system might yield additional cross-terms: i.e. $\mathbf{A}^+ \neq \mathbf{A}^H$.
An example of such a non-constant coefficient operator would be that of the LST operators such as those described in section 2.2. These operators not yield constant coefficient matrices due to their inherent $y-$dependency, and as a result $\mathbf{A}^+ \neq \mathbf{A}^H$ for the continuous linear operator case. When considering the discretised version of these operators, *then* the identity $\mathbf{A}^+ = \mathbf{A}^H$ does apply. This means that for a discrete EVP the adjoint eigenvectors could be derived by determining the left eigenvectors of the direct EVP. The left eigenvectors of the direct EVP equal the eigenvectors of the Hermitian transpose of the direct EVP operator, $\mathbf{A}^H$ in our example. In the current study we will use both the continous approach and the discrete approach to obtain $\mathbf{A}^+$.

3.1.1. Application of adjoint operators

Inherent to the inner product definition of the adjoint, with its bilinear characteristics, bi-orthogonality relations regarding the two sets of eigenmodes may be derived [20]. The bi-orthogonality relations

can be used for the projection of "*any initial condition or external forcing onto the basis formed by the system's eigenvectors*" [19]. Thereby the adjoints help provide insight into the sensitivity and response of a system to initial conditions or types of forcing of interest. Schmid [19] notes that triggering a specific mode is best done by "*using the velocity profile defined by its adjoint*".

In another application, the adjoint operator may be used to determine optimal growth modes [20], which may especially be of interest for the transient growth perspectives touched upon earlier in the introduction to this thesis.

For further applications of the adjoint equations in stability analysis, see the review of Luchini & Bottaro [8].

3.2. Primitive variable incompressible LST

In the primitive variable formulation the incompressible LST equations can be expressed as the generalised eigenvalue problem $(\mathbf{A}-\omega\mathbf{B})\tilde{q}=\mathbf{C}\tilde{q}=0$:

$$\mathcal{L}=\begin{bmatrix}\mathrm{x-momentum}\\ \mathrm{y-momentum}\\ \mathrm{z-momentum}\\ \mathrm{continuity}\end{bmatrix}\Rightarrow \qquad \mathbf{C}\tilde{q}=\begin{bmatrix}G & \overline{U}_y & 0 & i\alpha\\ 0 & G & 0 & \mathcal{D}\\ 0 & \overline{W}_y & G & i\beta\\ i\alpha & \mathcal{D} & i\beta & 0\end{bmatrix}\begin{bmatrix}\tilde{u}\\ \tilde{v}\\ \tilde{w}\\ \tilde{p}\end{bmatrix} \tag{3.3}$$

with $G=-i\omega+i\alpha\overline{U}+i\beta\overline{W}-\frac{1}{Re}(\mathcal{D}^2-k^2)$, and homogeneous boundary conditions $\tilde{u}=\tilde{v}=\tilde{w}=0$ at the walls in case of Poiseuille flow – or more generally speaking – at the bounds of the domain. Note that we here consider the temporal eigenvalue problem with the frequency ω as the eigenvalue.

Property-wise, it is interesting to note that the mean flow terms $\overline{U}_y$ and $\overline{W}_y$ are the sole cause of system asymmetry in $\mathbf{C}$. Thereby preventing us from using the hugely simplifying properties of symmetric matrices, such as orthogonal eigenvectors or real eigenvalues. Furthermore, it is to be observed that perturbation pressure-wise there is no implicit coupling between the momentum and continuity equations. And with the velocity perturbation components known on the boundaries through the homogeneous boundary conditions, the perturbation pressure solution essentially does not have any boundary conditions itself. Although, we do employ pressure compatibility conditions on $\frac{\partial\tilde{p}}{\partial y}$ in the TU Delft stability code through use of the y-momentum equation defined at the wall and free-stream edge. That is, a Neumann boundary condition forced by the viscous term on the RHS. Thereby the pressure perturbation is not prescribed on the boundaries, but follows from the velocity components, consequently yielding a singular system. The singular pressure modes can be interpreted as superfluous unknowns which can take on any value $\tilde{p}_{i,j}+const$ without affecting the pressure gradients or the conservation of mass. As such there are infinitely many solutions. In EVPs the undetermined constant in the perturbation-pressure solution is set randomly by the eigensolver [4].

In the discrete approach solving, the above direct EVP using Matlab's *eig* yields the direct eigenvectors (right eigenvectors) and the discrete adjoint eigenvectors (the left eigenvectors).

3.2.1. Continuous approach

If we now intend to derive the adjoint operator $\mathbf{C}^+$ using the continuous approach we effectively determine the transpose and complex conjugate of operator $\mathbf{C}$, as per the inner product definition of the adjoint operator. In the derivation below we will do so by (**STEP 1**) defining the inner product $(\tilde{q}^+,\mathbf{C}\tilde{q})=\int_y(\tilde{q}^+)^*\mathbf{C}\tilde{q}\ \mathrm{d}y=0$, (**STEP 2**) performing integration by parts on the inner product to transpose the system and (**STEP 3**) taking the complex conjugate of the remaining expression so as to determine the adjoint of the complete *operator* as opposed to just the *matrix* (i.e. as for example constants taken out of the matrix in order to simplify the transposition, might themselves still be complex numbers).

STEP 1:

$$\int_y \begin{bmatrix}(\tilde{u}^+)^* & (\tilde{v}^+)^* & (\tilde{w}^+)^* & (\tilde{p}^+)^*\end{bmatrix} \begin{bmatrix} G & \overline{U}_y & 0 & i\alpha \\ 0 & G & 0 & \mathcal{D} \\ 0 & \overline{W}_y & G & i\beta \\ i\alpha & \mathcal{D} & i\beta & 0 \end{bmatrix} \begin{bmatrix}\tilde{u}\\ \tilde{v}\\ \tilde{w}\\ \tilde{p}\end{bmatrix} \mathrm{d}y = 0 \tag{3.4}$$

STEP 2:

1. Performing integration by parts on the inner product's x-momentum terms:

$$\int (\tilde{u}^+)^* \left[-i\omega + i\alpha\overline{U} + i\beta\overline{W} - \frac{1}{Re}(\mathcal{D}^2 - k^2)\right](\tilde{u})\mathrm{d}y + \int (\tilde{u}^+)^* \left[\overline{U}_y\right](\tilde{v})\mathrm{d}y + \int (\tilde{u}^+)^* [i\alpha](\tilde{p})\mathrm{d}y$$

$$\Rightarrow \quad \int (\tilde{u}) \left[-i\omega + i\alpha\overline{U} + i\beta\overline{W} - \frac{1}{Re}(\mathcal{D}^2 - k^2)\right](\tilde{u}^+)^*\mathrm{d}y - \left[\frac{1}{Re}((\tilde{u})\mathcal{D}(\tilde{u}^+)^*)\right]_{\mathrm{BC}} - \left[\frac{1}{Re}((\tilde{u}^+)^*\mathcal{D}(\tilde{u}))\right]_{\mathrm{BC}}$$
$$+ \int (\tilde{v})\left[\overline{U}_y\right](\tilde{u}^+)^*\mathrm{d}y + \int (\tilde{p})\,[i\alpha]\,(\tilde{u}^+)^*\mathrm{d}y$$

$$\Rightarrow \quad \int (\tilde{u}) \left[-i\omega + i\alpha\overline{U} + i\beta\overline{W} - \frac{1}{Re}(\mathcal{D}^2 - k^2)\right](\tilde{u}^+)^*\mathrm{d}y + \int (\tilde{v})\left[\overline{U}_y\right](\tilde{u}^+)^*\mathrm{d}y + \int (\tilde{p})\,[i\alpha]\,(\tilde{u}^+)^*\mathrm{d}y$$

note that after applying $\tilde{u}(\mathrm{BC}) = 0$, and choosing $(\tilde{u}^+)^*(\mathrm{BC}) = 0$, there are no integration-by-parts boundary terms left in the expression.

2. Performing integration by parts on the inner product's y-momentum terms

$$\int (\tilde{v}^+)^* \left[-i\omega + i\alpha\overline{U} + i\beta\overline{W} - \frac{1}{Re}(\mathcal{D}^2 - k^2)\right](\tilde{v})\mathrm{d}y + \int (\tilde{v}^+)^*\mathcal{D}(\tilde{p})\mathrm{d}y$$

$$\Rightarrow \quad \int (\tilde{v}) \left[-i\omega + i\alpha\overline{U} + i\beta\overline{W} - \frac{1}{Re}(\mathcal{D}^2 - k^2)\right](\tilde{v}^+)^*\mathrm{d}y - \int (\tilde{p})\mathcal{D}(\tilde{v}^+)^*\mathrm{d}y$$

again, by applying $\tilde{v}(\mathrm{BC}) = 0$, and choosing $(\tilde{v}^+)^*(\mathrm{BC}) = 0$, there are no integration-by-parts boundary terms left in the expression. Also note the '–' due to the integration-by-parts on the direct pressure gradient term (transposing from $\mathcal{D}\tilde{p}$ to $(\mathcal{D}\tilde{v}^+)^*$).

3. Performing integration by parts on the inner product's z-momentum terms

$$\int (\tilde{w}^+)^* \left[-i\omega + i\alpha\overline{U} + i\beta\overline{W} - \frac{1}{Re}(\mathcal{D}^2 - k^2)\right](\tilde{w})\mathrm{d}y + \int (\tilde{w}^+)^* \left[\overline{W_y}\right](\tilde{v})\mathrm{d}y + \int (\tilde{w}^+)^* [i\beta](\tilde{p})\mathrm{d}y$$

$$\Rightarrow \quad \int (\tilde{w}) \left[-i\omega + i\alpha\overline{U} + i\beta\overline{W} - \frac{1}{Re}(\mathcal{D}^2 - k^2)\right](\tilde{w}^+)^*\mathrm{d}y + \int (\tilde{v})\left[\overline{W_y}\right](\tilde{w}^+)^*\mathrm{d}y + \int (\tilde{p})\,[i\beta]\,(\tilde{w}^+)^*\mathrm{d}y$$

observe that by applying $\tilde{w}(\mathrm{BC}) = 0$, and choosing $(\tilde{w}^+)^*(\mathrm{BC}) = 0$, there are no additional boundary terms due to the integration-by-parts procedure to be found in the expression.

4. Performing integration by parts on the inner product's continuity terms

$$\int (\tilde{p}^+)^* [i\alpha](\tilde{u})\mathrm{d}y + \int (\tilde{p}^+)^*\mathcal{D}(\tilde{v})\mathrm{d}y + \int (\tilde{p}^+)^* [i\beta](\tilde{w})\mathrm{d}y$$

$$\Rightarrow \quad \int (\tilde{u})\,[i\alpha]\,(\tilde{p}^+)^*\mathrm{d}y - \int (\tilde{v})\mathcal{D}(\tilde{p}^+)^*\mathrm{d}y + \int (\tilde{w})\,[i\beta]\,(\tilde{p}^+)^*\mathrm{d}y$$

by applying $\tilde{v}(\mathrm{BC}) = 0$ there are no additional boundary terms due to the integration-by-parts procedure (do note the '−' resulting from the transposition from velocity gradient to pressure gradient).

As such the transposed system becomes:

$$\begin{bmatrix}\tilde{u} & \tilde{v} & \tilde{w} & \tilde{p}\end{bmatrix}\begin{bmatrix} G & 0 & 0 & i\alpha \\ \overline{U}_y & G & \overline{W}_y & -\mathcal{D} \\ 0 & 0 & G & i\beta \\ i\alpha & -\mathcal{D} & i\beta & 0 \end{bmatrix}\begin{bmatrix}(\tilde{u}^+)^* \\ (\tilde{v}^+)^* \\ (\tilde{w}^+)^* \\ (\tilde{p}^+)^*\end{bmatrix} = 0 \tag{3.5}$$

STEP 3: Finally, taking the c.c. of the complete transposed expression:

$$\int_y \begin{bmatrix}\tilde{u}^* & \tilde{v}^* & \tilde{w}^* & \tilde{p}^*\end{bmatrix}\begin{bmatrix} G^* & 0 & 0 & -i\alpha^* \\ \overline{U}_y & G^* & \overline{W}_y & -\mathcal{D} \\ 0 & 0 & G^* & -i\beta^* \\ -i\alpha^* & -\mathcal{D} & -i\beta^* & 0 \end{bmatrix}\begin{bmatrix}\tilde{u}^+ \\ \tilde{v}^+ \\ \tilde{w}^+ \\ \tilde{p}^+\end{bmatrix}\mathrm{d}y = 0 \quad \Rightarrow \quad (\tilde{q}, \mathbf{C}^+\tilde{q}^+) = 0 \tag{3.6}$$

where $G^* = i\omega^* - i\alpha^*\overline{U} - i\beta^*\overline{W} - \frac{1}{Re}(\mathcal{D}^2 - k^2)$, and homogeneous boundary conditions $\tilde{u}^+ = \tilde{v}^+ = \tilde{w}^+ = 0$ at the wall and free-stream edge in case of boundary layer flow – or more generally speaking – at the bounds of the domain. As with the direct system the (Neumann) boundary condition for the pressure (i.e. on $\mathcal{D}(\tilde{p}^+)^*(\mathrm{BC})$) is provided through the use of – in this case – the adjoint y-momentum equation as the compatibility condition. This follows from the derivation, for which in the adjoint y-moment equation the pressure gradient is again coupled with the viscous term.
Note that for the adjoint formulation ω^* would be considered the eigenvalue. See also section 4.1 for more information on the relation between the adjoint and direct eigenvalues. Furthermore, the spatial wavenumbers in the LST currently used are taken to be real, but in an effort to remain as general as possible, here they are still shown as being in their complex conjugate form.

Furthermore, as Schmid & Henningson [20] also noted: the form of the adjoint depends on the particular inner product that is chosen for the transposition of the operator. Note that in this continuous approach we have taken the complex conjugate of the complete expression, including any constants.

3.3. Primitive variable compressible LST

As with the incompressible LST derivation in section 3.2 the discrete approach involves solving the above direct EVP using Matlab's *eig* for the direct eigenvectors (right eigenvectors) and the discrete adjoint eigenvectors (the left eigenvectors). The continuous approach can be executed using the same steps as in section 3.2. See the Appendix A for the full derivation of the adjoint system for the compressible LST equations.

Interesting to note regarding the continuous adjoint derivation is that as a result of the continuous complex conjugate transposition there is a shift to be observed from mu-transport variables in the direct equations to lambda-transport variables in the adjoint equations due to the homogeneous boundary conditions used in the integration-by-parts.

4

Derivations of bi-orthogonality relations

In this chapter we will first derive the bi-orthogonality relations that ensure orthogonal sets of direct and adjoint eigenvectors in Sections 4.1 and 4.2. We will further discuss the numerical implementation and results of said biorthogonality relations for the compressible and incompressible LST equations in Sections 4.3, 4.4 and 4.5.

4.1. Theoretical: direct and adjoint eigenvectors incompressible LST

Consider the generalised direct (I) and adjoint (II) EVPs, respectively:

$$\begin{aligned} I: &\quad \mathbf{A}\tilde{q_j} = \omega_j \mathbf{B}\tilde{q_j} \\ II: &\quad \mathbf{A}^+\tilde{q_i}^+ = \omega_i^+ \mathbf{B}^+\tilde{q_i}^+ \end{aligned}$$

where by definition $\mathbf{A}^+ = \mathbf{A}^H$. That is, the adjoint operator $\mathbf{A}^+$ is defined as the complex conjugate transpose of the orginal operator $\mathbf{A}$. Then we can show the relation between the direct and adjoint eigenvalues by taking the inner products (I_a): $(\tilde{q_i}^+, \mathbf{A}\tilde{q_j}) = \omega_j(\tilde{q_i}^+, \mathbf{B}\tilde{q_j})$ and (II_a): $(\tilde{q_j}, \mathbf{A}^+\tilde{q_i}^+) = \omega_i^+(\tilde{q_j}, \mathbf{B}^+\tilde{q_i}^+)$.

$$\begin{aligned} I_a: &\quad (\tilde{q_i}^+)^H \mathbf{A}\tilde{q_j} = \omega_j(\tilde{q_i}^+)^H \mathbf{B}\tilde{q_j} \\ II_a: &\quad (\tilde{q_j})^H \mathbf{A}^+\tilde{q_i}^+ = \omega_i^+(\tilde{q_j})^H \mathbf{B}^+\tilde{q_i}^+ \end{aligned}$$

For which (I_a) – by rewriting the inner product and using the definition of the adjoint operator – becomes:

$$I_b: \quad (\mathbf{A}^+\tilde{q_i}^+)^H \tilde{q_j} = \omega_j(\mathbf{B}^+\tilde{q_i}^+)^H \tilde{q_j}$$

now taking the Hermitian conjugate of (I_b) yields:

$$I_c: \quad (\tilde{q_j})^H \mathbf{A}^+\tilde{q_i}^+ = \omega_j^*(\tilde{q_j})^H \mathbf{B}^+\tilde{q_i}^+$$

Comparing (I_c) with (II_a) shows that $\omega_i^+ = \omega_j^*$. As such the definition of the adjoint implies that the adjoint eigenvalues ω^+ are the complex conjugates of the direct eigenvalues ω.

To evaluate the bi-orthogonality between the sets of direct and adjoint eigenvectors we now define the following identity:

$$III: \quad (\tilde{q_i}^+)^H \mathbf{A}\tilde{q_j} - (\tilde{q_i}^+)^H \mathbf{A}\tilde{q_j} = 0$$

Recall the inner product of the adjoint eigenvector onto the direct problem:

$$\begin{aligned} & (\tilde{q_i}^+, \mathbf{A}\tilde{q_j}) = \omega_j (\tilde{q_i}^+, \mathbf{B}\tilde{q_j}) \\ \Rightarrow \quad & (\tilde{q_i}^+)^H \mathbf{A}\tilde{q_j} = \omega_j (\tilde{q_i}^+)^H \mathbf{B}\tilde{q_j} \end{aligned}$$

Rewriting (III) through use of (I) and (II), and the definition of the inner product and adjoint operator:

$$\begin{aligned} III_a: \quad & (\tilde{q_i}^+)^H (\omega_j \mathbf{B}\tilde{q_j}) - (\mathbf{A}^+ \tilde{q_i}^+)^H \tilde{q_j} = 0 \\ \Rightarrow III_b: \quad & (\tilde{q_i}^+)^H (\omega_j \mathbf{B}\tilde{q_j}) - (\omega_i^+ \mathbf{B}^+ \tilde{q_i}^+)^H \tilde{q_j} = 0 \\ \Rightarrow III_c: \quad & (\tilde{q_i}^+)^H (\omega_j \mathbf{B}\tilde{q_j}) - (\tilde{q_i}^+)^H ((\omega_i^+)^* \mathbf{B}\tilde{q_j}) = 0 \end{aligned}$$

Or equivalently to (III_c):

$$III_d: \quad \left(\omega_j - (\omega_i^+)^*\right) \left[(\tilde{q_i}^+)^H \mathbf{B}\tilde{q_j}\right] = 0$$

If we assume simple eigenvalues

$$\omega_j \neq \omega_i \qquad i \neq j$$

expression (III_d) yields the following bi-orthogonality relations between the adjoint eigenvectors and the direct eigenvectors:

$$(\tilde{q_i}^+)^H \mathbf{B}\tilde{q_j} = 0 \qquad i \neq j \tag{4.1}$$

$$(\tilde{q_i}^+)^H \mathbf{B}\tilde{q_j} = C_1 \qquad i = j \tag{4.2}$$

Note that in (III_d) the latter equation $\mathbf{B}$ acts as a weight to ensure orthogonality between the two sets of eigenvectors $\tilde{q_j}$ and $\tilde{q_i}^+$. For the incompressible LST equations – with the y-direction evaluated differentially, and x- and z-directions spectrally – this yields the orthogonality weight:

$$\mathbf{B} = \begin{bmatrix} i & 0 & 0 & 0 \\ 0 & i & 0 & 0 \\ 0 & 0 & i & 0 \\ 0 & 0 & 0 & 0 \end{bmatrix} \tag{4.3}$$

Or in other words, by integrating over the domain the following orthogonality relation applies for the continuous approach:

$$\int i \left[(\tilde{u_i}^+)^* \tilde{u_j} + (\tilde{v_i}^+)^* \tilde{v_j} + (\tilde{w_i}^+)^* \tilde{w_j}\right] \mathrm{d}y = 0 \qquad i \neq j \tag{4.4}$$

$$\int i \left[(\tilde{u_i}^+)^* \tilde{u_j} + (\tilde{v_i}^+)^* \tilde{v_j} + (\tilde{w_i}^+)^* \tilde{w_j}\right] \mathrm{d}y = C_2 \qquad i = j \tag{4.5}$$

whereas for the discrete approach the matrix operations following from the relations in 4.1 and 4.2 apply.

Recall that for the generalised EVP the primitive variable incompressible LST system operator, $\mathbf{A}$ would be represented by:

$$\mathbf{A} = \begin{bmatrix} F & \overline{U_y} & 0 & i\alpha \\ 0 & F & 0 & \mathcal{D} \\ 0 & \overline{W_y} & F & i\beta \\ i\alpha & \mathcal{D} & i\beta & 0 \end{bmatrix} \tag{4.6}$$

with $F = i\alpha\overline{U} + i\beta\overline{W} - \frac{1}{Re}(\mathcal{D}^2 - k^2)$

4.2. Theoretical: direct and adjoint eigenvectors compressible LST

Given that the compressible problems – both direct and adjoint – are also defined as a generalised EVP, an analysis similar to section 4.1 again yields the condition

$$III_d: \qquad \left(\omega_j - (\omega_i^+)^*\right)\left[(\tilde{q}_i{}^+)^H \mathbf{B} \tilde{q}_j\right] = 0 \tag{4.7}$$

So if we assume simple eigenvalues

$$\omega_j \neq \omega_i \qquad i \neq j \tag{4.8}$$

expression (III_d) yields the following bi-orthogonality relations between the adjoint eigenvectors and the direct eigenvectors:

$$(\tilde{q}_i{}^+)^H \mathbf{B} \tilde{q}_j = 0 \qquad i \neq j \tag{4.9}$$

$$(\tilde{q}_i{}^+)^H \mathbf{B} \tilde{q}_j = C_1 \qquad i = j \tag{4.10}$$

For the compressible LST equations with the y-direction evaluated differentially, and x- and z-directions spectrally this yields the orthogonality weight $\mathbf{B}$:

$$\mathbf{B} = \begin{bmatrix} E & 0 & 0 & 0 & 0 \\ 0 & E & 0 & 0 & 0 \\ 0 & 0 & i & -i\frac{\overline{P}}{\overline{T}} & 0 \\ 0 & 0 & -i(\gamma-1)M^2 & E & 0 \\ 0 & 0 & 0 & 0 & E \end{bmatrix} \tag{4.11}$$

with $E = \frac{i\gamma M^2 \overline{P}}{\overline{T}}$, and $\overline{T} = \overline{T}(y)$, $\overline{P} = \overline{P}(y)$ (the latter as a result of the ideal gas assumption).

4.3. Numerical: direct and adjoint eigenvectors incompressible LST

The incompressible continuous adjoint LST operator as derived in Chapter 3 is implemented in the TU Delft stability code with a Chebyshev collocation discretisation, homogeneous boundary conditions for the adjoint velocity perturbation amplitudes and a compatibility condition for the adjoint pressure perturbation amplitudes by means of the 'adjoint wall-normal y-momentum' equation. The resulting EVP is solved using Matlab's eig function. This yields the continuous adjoint eigenvectors and eigenvalues.

The discrete adjoint eigenvectors are obtained through the left eigenvectors of Matlab's eig function.

For the direct eigenvectors, and the continuous adjoint eigenvectors non-physical modes are omitted from the bi-orthogonality analysis. This concerns the previously identified spurious modes (see Chapter 2) and modes having infinite eigenvalues.

Eigenvalues

From the derivation in Section 4.1 we know that $\omega_i^+ = \omega_j^*$. A prima facie the complex conjugates of the continuous adjoint eigenvalue spectrum do match the direct eigenvalue spectrum in the physically interesting range (Figure 4.1). However on second inspection, it appears that outside of the range shown in Figure 4.1 there are rather large eigenvalues, $\mathcal{R}(\omega) > \mathcal{O}(10^4)$, in both the direct and adjoint sets. These large direct and adjoint eigenvalues tend to differ by $> \mathcal{O}(10^1)$. This marks a first discrepancy between the direct results and the continuous adjoint results, which may likely be attributed to the corresponding modes being non-physical modes given the size of the real part of these eigenvalues.

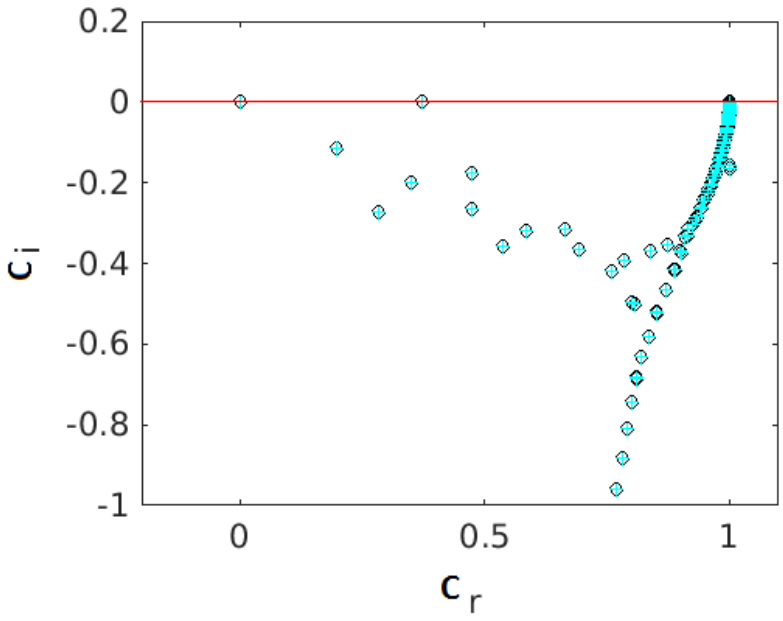

Figure 4.1: Temporal eigenvalue spectrum for incompressible LST with $M + 10^{-3}, Re = 580, \alpha = 0.2, NC = 150$. direct eigenvalues in black circles and adjoint eigenvalues in cyan pluses.

Discrete approach: Bi-orthogonality coefficient matrix

The bi-orthogonality relations derived in Section 4.1 yield a coefficient matrix, both for the discrete adjoint eigenvectors (matrix operation of the bi-orthogonality product) and the continous adjoint eigenvectors (integration of the bi-orthogonality product). The main point of the bi-orthogonality requirement is that this coefficient matrix is diagonal. To that end we will here use the following norm to determine how much the matrix A deviates from the diagonal matrix D containing only the diagonal elements of A:

$$dep_{diag} = ||A - D|| \tag{4.12}$$

This norm will be zero for a perfectly diagonal matrix A. For the incompressible discrete adjoint bi-orthogonality coefficient matrix $dep_{diag} = 5.4 \cdot 1e - 11$. This indicates that the norm of the off-diagonal terms in the coefficient matrix approaches zero. Thereby confirming that the product $(\tilde{q}^+)^H B\tilde{q}$ derived in Section 4.1 for the discrete adjoint eigenvectors is indeed bi-orthogonal. This notion is also exemplified visually in Figure 4.2. Here, only the diagonal terms are of order $\mathcal{O}(10^0)$, whereas the off-diagonal terms are of order $\sim \mathcal{O}(10^-10)$, or smaller.

In Figure 4.3 the bi-orthogonality norm $(\tilde{q}^+)^H B\tilde{q}$ can be seen to be dominant for eigenmodes with relatively low real phase speed that are highly damped, and increasingly dominant for modes approaching the phase speed of the free-stream U_e. The bi-orthogonality norm is relatively small (or zero) for the discrete wall modes, which can be recognised between elements 100 and 150. These discrete wall modes can be characterised as having relatively low damping and low real phase speed, with the eigenmode having its dominant amplitude close to the wall.

Also note that the bi-orthogonality norm $(\tilde{q}^+)^H B\tilde{q}$ as derived here is similar, to some extent, to the relation derived by Schmid [19] for the eigenvalue shift resulting from a matrix perturbation. They derived a proportionality constant $\frac{||q^+||||q|}{|<q^+,q>|}$ Schmid & Henningson [20] argued that the quantity $||q^+||_E||q|_E$, i.e. the energy norms of the adjoint and direct eigenmodes, can be interpreted as the relative sensitivity of an individual eigenvalue. In their derivation this quantity appears as the proportionality constant between the size of a matrix perturbation and the shift of

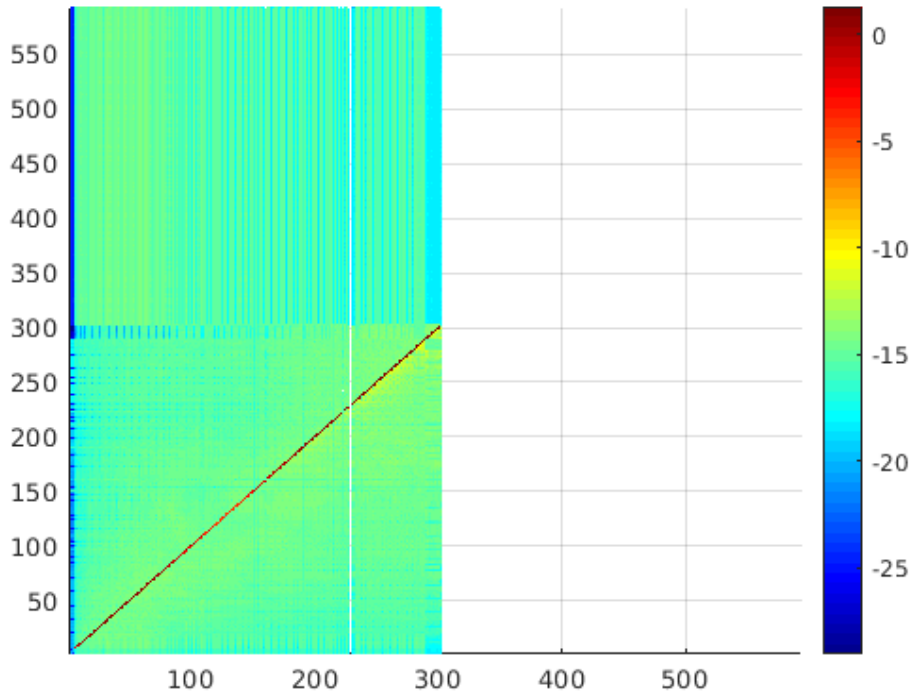

Figure 4.2: Mesh plot of $log(abs(\cdot))$ of the coefficient matrix entries for the discrete approach. Results are from an incompressible LST computation with $M = 10^{-3}, Re = 580, \alpha = 0.2, NC = 150$.

the eigenvalue. It should be noted that Schmid's [19] and Schmid & Henningson's [20] derivations both were for an eigenvalue problem of the form $\omega\tilde{q} = A\tilde{q}$. The bi-orthogonality norm $(\tilde{q}^+)^H B\tilde{q}$ may thus *perhaps* provide some insight into the relative sensitivity of an eigenmode to perturbations in a generalised EVP. Extending this to the findings in this section might indicate that those eigenvalues with small contributions of the bi-orthogonality norm in Figure 4.3 would shift less when the LST operator is perturbed than those with a larger norm.

Overlap between the direct and adjoint eigenvectors

In Figures 4.4 and 4.5 the 'overlap' $(\tilde{q}_i^+)^H B\tilde{q}_i$ between the direct eigenvectors $\tilde{q}_i$ and the discrete adjoint eigenvectors $\tilde{q}_i^+$ can be seen for a wall mode, and a 'middle-layer mode' respectively. In both these cases the dominant amplitude of the direct eigenmode is located lower than the dominant amplitude of the discrete adjoint eigenmode. For the wall mode in 4.4 the shaping is also different as the direct mode has a 'second peak' towards δ_{99}, whereas the adjoint mode then approaches zero.

Continuous approach: Bi-orthogonality coefficient matrix

Unlike the discrete approach, for the incompressible continuous adjoint bi-orthogonality coefficient matrix $dep_{diag} = 83.25$. This indicates that the coefficient matrix does contain substantial off-diagonal terms, which is in disagreement with the bi-orthogonality relations derived in Section 4.1. Although one could argue that the coefficient matrix is diagonally dominant (see also Figure 4.6 for a visual representation).

To investigate why the continous approach does not yield the expected bi-orthogonal matrix, we have compared a discrete adjoint mode with the corresponding continously derived adjoint mode in Figure 4.7. This figure shows that whilst the discrete and continous adjoint eigenmodes are *similar* in shape and location, the modes do not coincide. As a result the bi-orthogonality norm for this particular eigenmode would indeed yield different results for the discrete approach versus

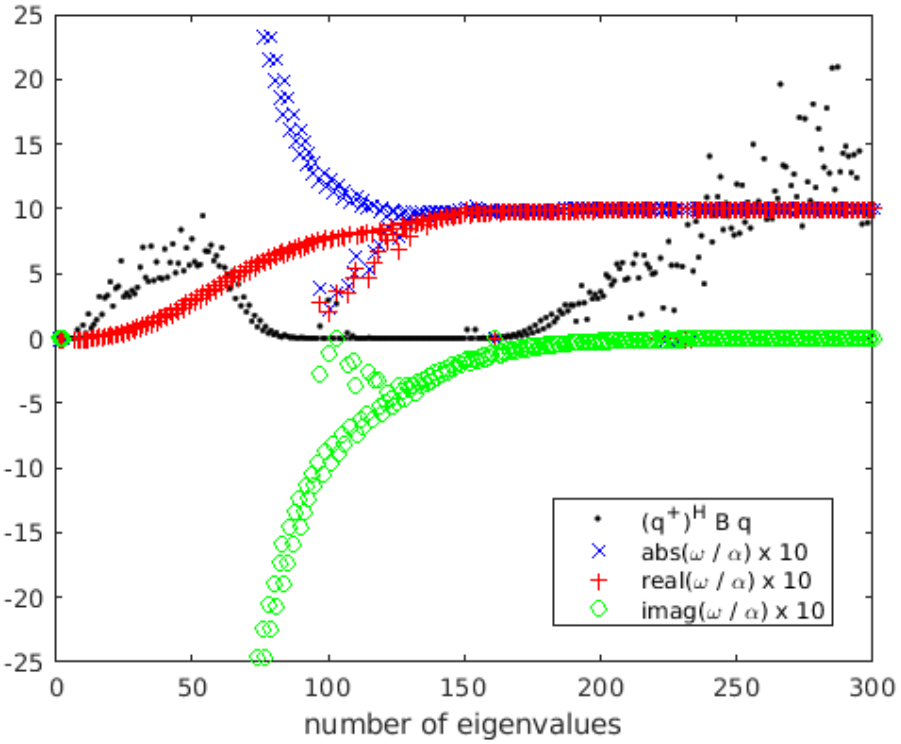

Figure 4.3: Dominant contributions of the bi-orthogonality norm for the discrete approach, shown with the corresponding eigenvalue: its absolute value, and the real and imaginary parts. Results are from an incompressible LST computation with $M = 10^{-3}, Re = 580, \alpha = 0.2, NC = 150$.

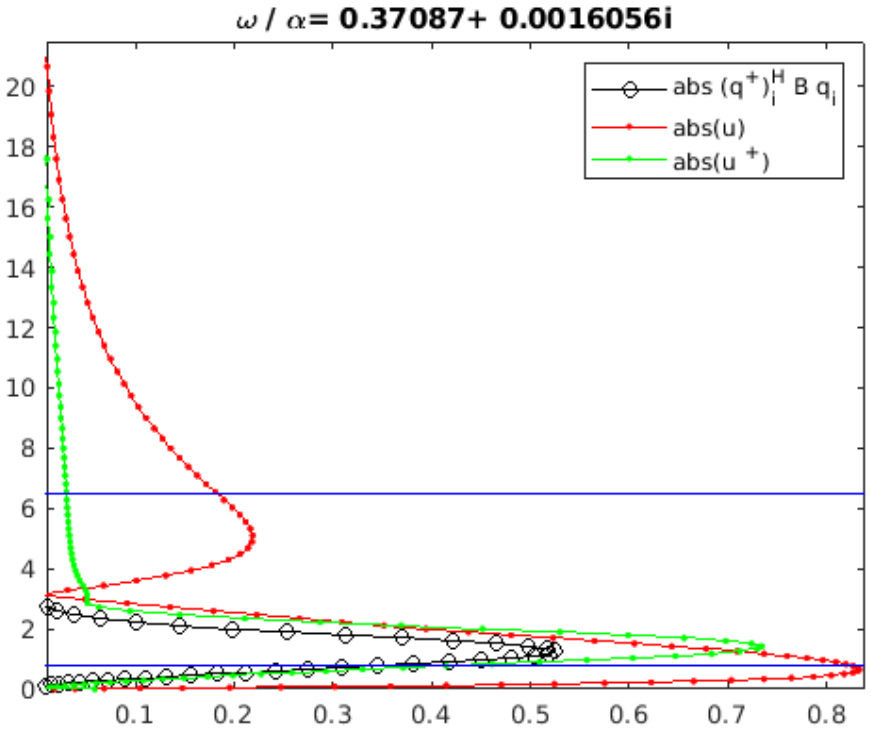

Figure 4.4: Plot of the 'overlap' product $(\tilde{q}_i^+)^H B \tilde{q}_i$ using the direct eigenvector $\tilde{q}_i$ and the discrete adjoint eigenvector $\tilde{q}_i^+$, for a wall mode with $\omega/\alpha = 0.37 + 0.0016i$. The bottom blue line represents $\delta_{25} \rightarrow \tilde{u}/U_e \approx 25\%$. The top blue line represents $\delta_{99} \rightarrow \tilde{u}/U_e \approx 99\%$. Results are from an incompressible LST computation with $M = 0^{-3}, Re = 580, \alpha = 0.2, NC = 150$.

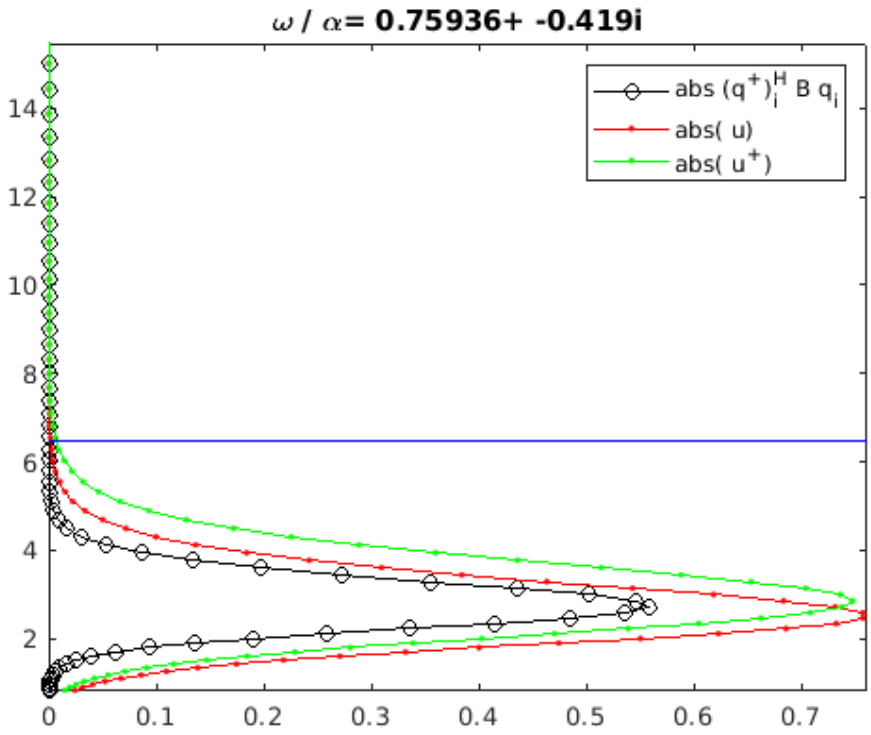

Figure 4.5: Plot of the 'overlap' product $(\tilde{q}_i^+)^H B \tilde{q}_i$ using the direct eigenvector $\tilde{q}_i$ and the discrete adjoint eigenvector $\tilde{q}_i^+$, for a 'middle-layer' mode with $\omega/\alpha = 0.76 - 0.42i$. The bottom blue line represents $\delta_{25} \rightarrow \tilde{u}/U_e \approx 25\%$. The top blue line represents $\delta_{99} \rightarrow \tilde{u}/U_e \approx 99\%$. Results are from an incompressible LST computation with $M = 0^{-3}, Re = 580, \alpha = 0.2, NC = 150$.

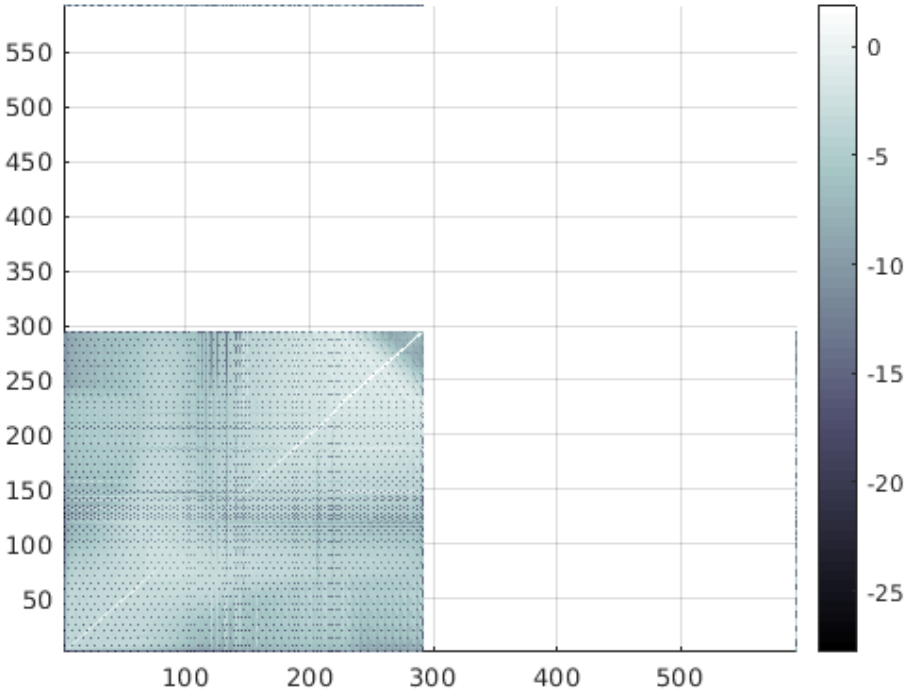

Figure 4.6: Mesh plot of $log(abs(\cdot))$ of the coefficient matrix entries for the continuous approach. Results are from an incompressible LST computation with $M = 0^{-3}, Re = 580, \alpha = 0.2, NC = 150$.

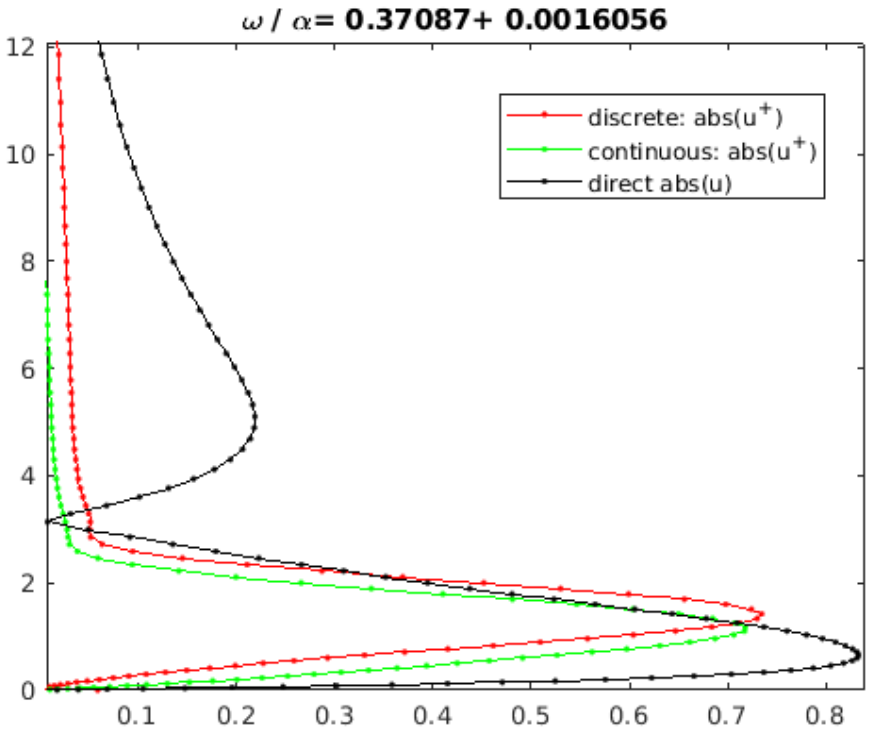

Figure 4.7: Comparison between a discrete adjoint eigenmode and the corresponding continuous adjoint eigenmode. Results are from an incompressible LST computation with $M = 0^{-3}, Re = 580, \alpha = 0.2, NC = 150$.

the continuous approach. A potential explanation might be that in the continous approach the adjoint eigenvalue problem is solved using Chebyshev collocation nodes set-up similar to the direct eigenvalue problem, whereas in the discrete approach the Matlab left eigenvectors are *weighted* accordingly to be represented on the same nodes as the direct eigenvectors.

4.4. Numerical: direct and adjoint eigenvectors compressible LST

Similarly to the incompressible adjoint, the compressible LST operator derived in Chapter 3 is implemented in the TU Delft stability code with a Chebyshev collocation discretisation, homogeneous boundary conditions for the velocity perturbation amplitudes and the temperature perturbation amplitudes, and a compatibility condition for the pressure perturbation amplitudes by means of the 'adjoint wall-normal y-momentum' equation. The resulting EVP is solved using Matlab's eig function.This yields the continuous adjoint eigenvectors and eigenvalues.

The discrete adjoint eigenvectors are obtained through the left eigenvectors of Matlab's eig function.

For the direct eigenvectors, and the continuous adjoint eigenvectors non-physical modes are omitted from the bi-orthogonality analysis. This concerns the previously identified spurious modes (see Chapter 2) and modes having infinite eigenvalues.

Eigenvalues

Again, a prima facie the complex conjugates of the continuous adjoint eigenvalue spectrum appear to match the direct eigenvalue spectrum in the physically interesting range (Figure 4.8). Yet, on second inspection, it appears that outside of the range shown in Figure 4.1 there are rather large eigenvalues, $\mathcal{R}(\omega) > \mathcal{O}(10^4)$, in both the direct and adjoint sets. These large direct and adjoint eigenvalues tend to differ by $> \mathcal{O}(10^1)$. As with the incompressible LST results in Section 4.3 this marks a first discrepancy between the direct results and the continuous adjoint results, which may likely be attributed to the corresponding modes being non-physical modes given the size of the

real part of these eigenvalues.

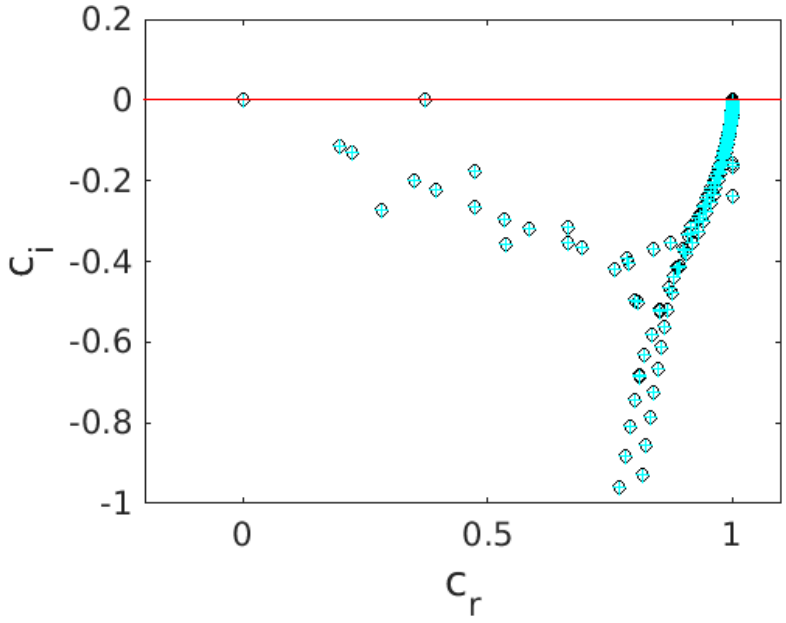

Figure 4.8: Temporal eigenvalue spectrum for compressible LST with $M + 10^{-3}, Re = 580, \alpha = 0.2, NC = 150$. direct eigenvalues in black circles and adjoint eigenvalues in cyan pluses.

Discrete approach: Bi-orthogonality coefficient matrix

For the compressible discrete adjoint bi-orthogonality coefficient matrix $dep_{diag} = 1.3 \cdot 10^{-10}$. This indicates that the norm of the off-diagonal terms in the coefficient matrix approaches zero. Thereby confirming that the product $(\tilde{q}^{+})^{H} B \tilde{q}$ derived in Section 4.1 for the discrete adjoint eigenvectors is indeed bi-orthogonal. This notion is also exemplified visually in Figure 4.9. Here, only the diagonal terms are of order $\mathcal{O}(10^{0})$, whereas the off-diagonal terms are of order $\sim \mathcal{O}(10^{-}10)$, or smaller.

In Figure 4.10 the bi-orthogonality norm $(\tilde{q}^{+})^{H} B \tilde{q}$ can be seen to be dominant for eigenmodes that are highly damped and have relatively low real phase speed , and increasingly dominant for modes approaching the phase speed of the free-stream U_e. The bi-orthogonality norm is relatively small (or zero) for the discrete wall modes, which can be recognised between elements 400 and 500. These discrete wall modes can be characterised as having relatively low damping and low real phase speed, with the eigenmode having its dominant amplitude close to the wall.

Continuous approach: Bi-orthogonality coefficient matrix

For the compressible continous adjoint bi-orthogonality coefficient matrix $dep_{diag} = 99.81$. This indicates that the coefficient matrix does contain substantial off-diagonal terms. Figure 4.6 confirms the finding for the incompressible continous bi-orthogonality matrix in that the coefficient matrix is diagonally dominant.

4.5. Conclusions

Theoretically relations can be derived for which a weight matrix ensures bi-orthogonal sets of direct and adjoint eigenvectors. These adjoint eigenvectors may be obtained by means of a discrete approach or a continuous approach. Numerical implementation of these bi-orthogonality relations for both incompressible and compressible LST leads to diagonal bi-orthogonality coefficient matrices for the discrete case. Results for the continous approach show that the coefficient matrix is diagonally dominant, but does contain substantial off-diagonal terms. As per the theoretical derivation, the complex conjugates of the adjoint eigenvalues were shown to match the direct

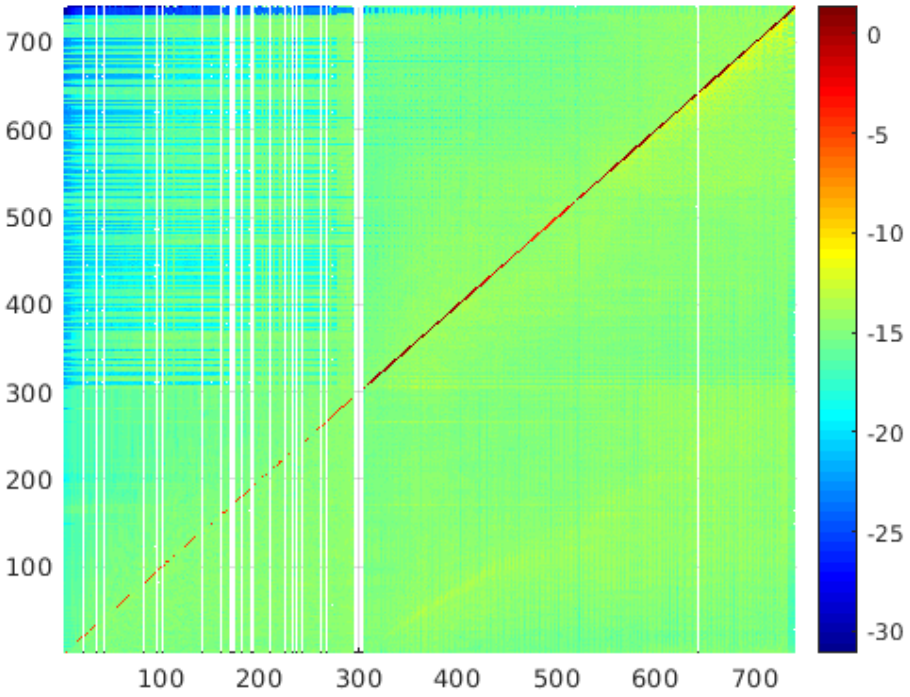

Figure 4.9: Mesh plot of $log(abs(\cdot))$ of the coefficient matrix entries for the discrete approach. Results are from a compressible LST computation with $M = 10^{-3}, Re = 580, \alpha = 0.2, NC = 150$.

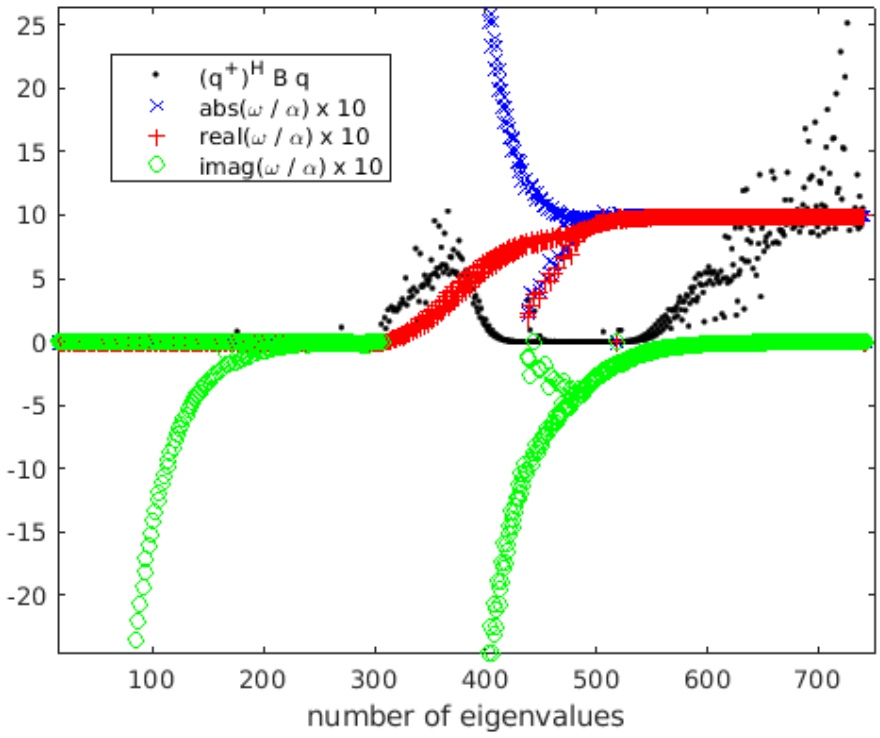

Figure 4.10: Dominant contributions of the bi-orthogonality norm for the discrete approach, shown with the corresponding eigenvalue: its absolute value, and the real and imaginary parts. Results are from a compressible LST computation with $M = 10^{-3}, Re = 580, \alpha = 0.2, NC = 150$.

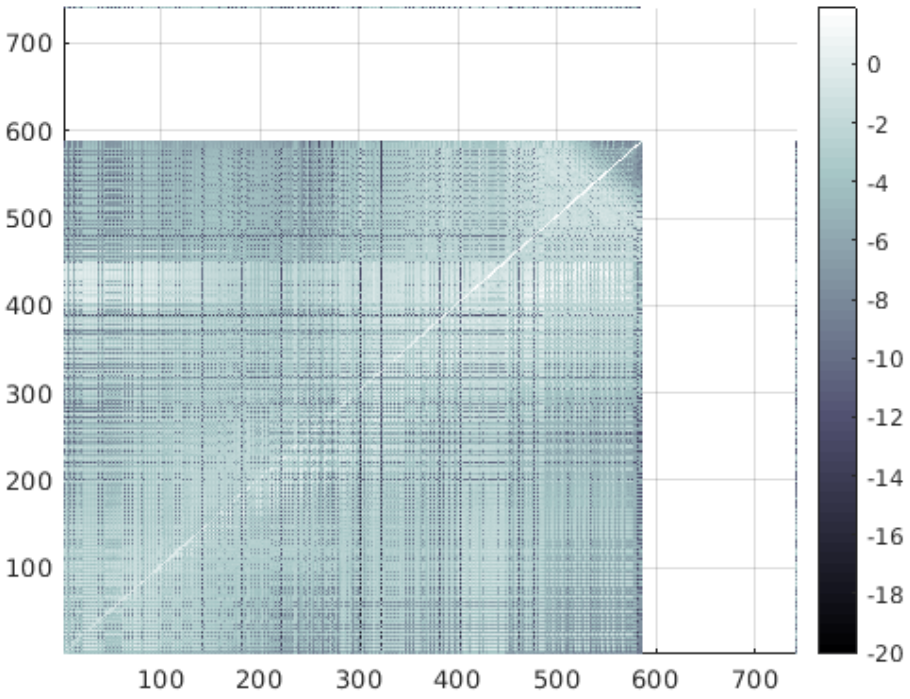

Figure 4.11: Mesh plot of $log(abs(\cdot))$ of the coefficient matrix entries for the continous approach. Results are from a compressible LST computation with $M = 10^{-3}, Re = 580, \alpha = 0.2, NC = 150$.

eigenvalues in the physically interesting range, for both the incompressible and compressible LST spectra.

To investigate why the continous approach does not yield the expected bi-orthogonal matrix, a discrete adjoint mode was compared with the corresponding continous adjoint mode. Whilst the discrete and continous adjoint eigenmodes were *similar* in shape and location, the modes were found not to coincide. A potential explanation for the discrepancy might be the use of the Chebyshev collocation nodes in the continous adjoint EVP. The adjoint EVP may require different stretching of the mesh. Alternatively, closing the continuous adjoint system using the 'adjoint wall-normal equation' as a compatiblity condition for the adjoint pressure amplitude might possibly adversely affect the continous adjoint eigenmodes.

The 'overlap' $(\tilde{q}_i^+)^H B \tilde{q}_i$ between the direct eigenvectors $\tilde{q}_i$ and the discrete adjoint eigenvectors $\tilde{q}_i^+$ was computed for a wall mode, and a 'middle-layer mode' respectively. Interestingly, for both modes the location of the maximum amplitude of the direct eigenmode was found to differ spatially from that of the maximum amplitude of the discrete adjoint eigenmode.

5

Perturbations of the LST operators

In this chapter we will first briefly discuss the basic state used in the LST computations in Section 5.1. Then the 'original' temporal eigenvalue spectra will be characterised in Section 5.2. Subsequently, in Section 5.3 pseudospectra will be presented for a perturbed generalised eigenvalue problem for a Falkner-Skan-Cooke boundary layer flow, for both the incompressible and compressible LST operators. Finally, we will provide our initial conclusions based on the results in Section 5.4.

5.1. Basic state

The basic state used in this work is a Falkner-Skan-Cooke boundary layer flow computed by Groot [5] using the DEKAF boundary-layer solver. The DEKAF boundary-layer solver employs a Chebyshev pseudo-spectral discretisation on the linearised compressible boundary-layer equations. These equations are then solved with a Newton-Raphson method. We here use their kindly provided 'case II', the Tollmien-Schlichting instability case in the incompressible flow regime with $M = 1e-3$, $Re = 580$, zero sweep, zero pressure gradient, and an adiabatic wall. For a complete overview of this basic state and the numerical methods involved, see [5].

5.2. Reference eigenvalue spectra

The reference incompressible LST eigenvalue spectra for $\alpha = 0.2$, $\alpha = 0.8$ and $\alpha = 6$ are shown in Figures 5.1a, 5.2a and 5.3a, respectively. The Figures 5.1b, 5.2b and 5.3b provide the same spectra, but with spurious modes (Chapter 2) and infinite eigenvalues removed, and the eigenvalues labelled for the dominant perturbation amplitude per eigenvalue.

The reference compressible LST eigenvalue spectra for $\alpha = 0.2$, $\alpha = 0.8$ and $\alpha = 6$ are shown in Figures 5.4a, 5.5a and 5.6a, respectively. The Figures 5.4b, 5.5b and 5.6b provide the same spectra, but with spurious modes (Chapter 2) and infinite eigenvalues removed, and the eigenvalues labelled for the dominant perturbation amplitude per eigenvalue.

The incompressible spectra can be seen to consist of a 'continous branch' of modes extending from $c_i \approx 0, c_r \approx 1$ downward, and a set of discrete modes to the left of this continous branch with $c_r \sim 0.2 - 0.7$ for $\alpha = 0.2$ (Figure 5.1a). As mentioned previously, these discrete modes, with lower real phase speeds, have their dominant amplitude close to the wall. Notably, the TS-mode, i.e. the 'most unstable' mode, which can be recognised in Figure 5.1a for $c_r \approx 0.4, c_i \approx 0$, .

The compressible spectra display a similar lay-out, but with additional modes due to the inclusion of the energy equation (Figure 5.4a). Additional modes can be observed in both the continous branch and the discrete set of modes. The additional modes in the continous branch initially follow the same pattern as the incompressible modes, but branch off for increasingly damped modes.

Also note that the continous branch in the incompressible spectra is relatively straight for $\alpha = 0.2$, but is shown to shift leftward for increasing spatial wavenumber α in Figures 5.2a and

5.3a. This same shift can be observed in the compressible spectra in Figures 5.5a and 5.6a.

The visible incompressible spectrum predominantly contains $\tilde{u}$- and $\tilde{w}$-dominant modes, with $\tilde{v}$-dominant modes being present in the top of the continous branch. The visible compressible spectrum predominantly contains $\tilde{u}$-, $\tilde{w}$- and $\tilde{T}$-dominant modes.

5.3. Pseudospectra

For the pseudospectra we solved a perturbed generalised eigenvalue problem:

$$(\mathbf{A} + \mathbf{E_0})q = \omega(\mathbf{B} + \mathbf{E_1})q, \quad \mathbf{E_0}, \mathbf{E_1}\mathbb{C}^{N\times N} : \mathcal{O}(\epsilon), \tag{5.1}$$

for $M = 10^{-3}, Re = 580, NC = 150, \alpha = [0.2, 0.8, 6]$, with $\mathbf{E_0}, \mathbf{E_1}$ containing random, complex perturbation elements picked from a normal distribution with a mean of 0 and a standard deviation of 1 and multiplied with a factor of $\mathcal{O}(\epsilon)$. The perturbation elements are imposed for $\mathcal{O}(\epsilon) = 10^{-4}$ - $\mathcal{O}(\epsilon) = 10^{-10}$, with 100 random cases for each $\mathcal{O}(\epsilon)$. The eigenvalue data is subsequently aggregated for the 100 random cases per $\mathcal{O}(\epsilon)$. To assess whether we can reliably use the eigenvalue data from the perturbed systems we evaluated the algorithm precision - $\epsilon_{machine} \cdot ||\mathbf{A}||_F$, which indicates the eigenvalue error. Both for the incompressible and the compressible eigenproblem computations the algorithm precision is in the order of $\leq \mathcal{O}(10^{-12})$ for all perturbation levels $\mathcal{O}(\epsilon) = 10^{-4}$ - $\mathcal{O}(\epsilon) = 10^{-10}$, respectively. This indicates a reliable result, with minimal eigenvalue error.

The superposition of the 100 sets of perturbed eigenvalue spectra per $\mathcal{O}(\epsilon)$ is shown for the incompressible LST computations in Figures 5.7a - 5.7f for $\alpha = 0.2$, in Figures 5.8a - 5.8f for $\alpha = 0.8$, and in Figures 5.9a - 5.9f for $\alpha = 6$.

The superposition of the 100 sets of perturbed eigenvalue spectra per $\mathcal{O}(\epsilon)$ is shown for the compressible LST computations in Figures 5.10a - 5.10f for $\alpha = 0.2$, in Figures 5.11a - 5.11f for $\alpha = 0.8$, and in Figures 5.12a - 5.12f for $\alpha = 6$.

Observations for increasing perturbations

If we consider increasing perturbation size, the disturbance of the spectrum appears to be initiated from the intersection of the continous branch and the discrete set of modes. For increasing perturbation size the disturbance of the spectrum then starts to spread outward. This behaviour can be observed to be very similar for both the incompressible and the compressible results. Also in terms of relative 'movement' of the eigenvalues do the incompressible and compressible spectra seem similar.

Another interesting general observation is that especially for larger perturbations the incompressible and compressible eigenvalues describe a contour within which most of the 'pseudo-eigenvalues' are contained in a relatively noisy pattern. As such, some eigenvalues shift further from the 'original' unperturbed location than the order of magnitude of the imposed perturbations would dictate. This finding is in agreement with Schmid [19] who noted for a Poiseuille flow and a Couette flow – both with perturbations of a norm $\epsilon = 5 \cdot 10^{-3}$ – that some eigenvalues would move from their unperturbed locations by an $\mathcal{O}(1)$ magnitude.

Observations for individual modes

Different modes appear to be affected differently by the matrix perturbations. As mentioned previously, the disturbance of the spectrum appears to be initiated for the modes at the intersection of the continous branch and the set of discrete modes. As an example we take the incompressible spectrum for $\alpha = 0.2$. In this example the modes at the intersection visibly move in the spectrum for perturbations of $\mathcal{O}(\epsilon) = 10^{-8}$. The 'free-stream' modes for which $c_r \to 1$ and the wall modes start to display a visible shift in the spectrum for $\mathcal{O}(\epsilon) = 10^{-6}$ and smaller. Even for relatively

large perturbations of $\mathcal{O}(\epsilon) = 10^{-5}$ the wall modes with the lowest phase speeds appear relatively unaffected and to be contained in a region close to the unperturbed eigenvalue.

Again comparing this to Schmid [19] shows that these findings are in line with the sensitivity results of the Poiseuille and Couette flows. Especially the Poiseuille eigenspectrum in their Figure 16 ([19])seems quite similar to the eigenspectrum of the boundary layer flow considered here.

The relative disturbance of the eigenmodes does not appear to be related to it's dominant amplitude. For example, in the compressible spectra the $\tilde{T}$-dominant modes and $\tilde{u}$-/$\tilde{w}$-dominant modes appear to be similarly affected.

Observations for α

First observations include that for $\alpha = 0.8$ and smaller, the eigenvalues start to visually 'shift' around the unperturbed set of eigenvalues for $\mathcal{O}(\epsilon) = 10^{-8})$ and larger, whilst for $\alpha = 6$ the spectrum appears to be more robust to perturbations and the eigenvalues start to visually shift around the unperturbed set of eigenvalues for $\mathcal{O}(\epsilon) = 10^{-7})$ and larger.

Furthermore it may be observed that the highly damped modes (i.e. the lower regions of the continous branch) shift considerably for $\alpha = 0.2$, whereas these damped modes are barely affected for $\alpha = 6$. Although we should keep in mind that the relative phase speed of these 'continuous branch' modes then approaches that of the discrete wall modes, whereas for $\alpha = 0.2$ the phase speed of the highly damped 'continuous branch' modes is closer to 1.

5.4. Conclusions

The disturbance of the eigenvalue spectrum as a result of the matrix perturbations appears to be initiated from the intersection of the continous branch and the discrete set of modes. For increasing perturbation size the disturbance of the spectrum then starts to spread outward. Especially for larger perturbations the eigenvalues describe a contour within which most of the 'pseudo-eigenvalues' are contained in a relatively noisy pattern. The eigenvalue spectrum appears to be more robust to perturbations for higher spatial wavenumbers α.

The spectrum has been shown to not be uniformly affected by matrix perturbations. Some eigenvalues have a visible shift in the spectrum for perturbations as small as $\mathcal{O}(10^{-8})$, whereas other eigenvalues display very little movement even for perturbations of $\mathcal{O}(10^{-4})$, or $\mathcal{O}(10^{-5})$. Interestingly, for some modes the shift of the eigenvalues in the spectrum is thus far greater in orders of magnitude than the perturbations imposed. Notably the set of discrete wall modes appears to remain relatively close to their unperturbed position.

Another interesting observation is that the 'free-stream' modes for which $c_r \to 1$, and the discrete wall modes with relatively small c_r tend to move less for a certain perturbation than the modes for which c_r is in between those two. As these findings are in agreement with the sensitivity findings of Schmid [19] for Poiseuille and Couette flow, there appears to be a pattern for perturbed eigenspectra of shear force flows.

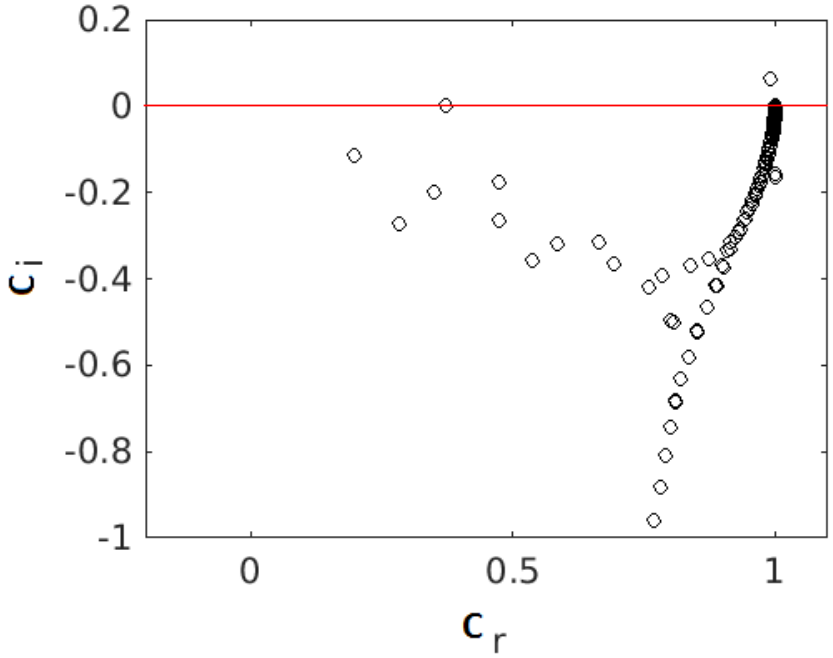

(a) Temporal eigenvalue spectrum for incompressible LST, with $M = 10^{-3}, Re = 580, \alpha = 0.2, NC = 150$.

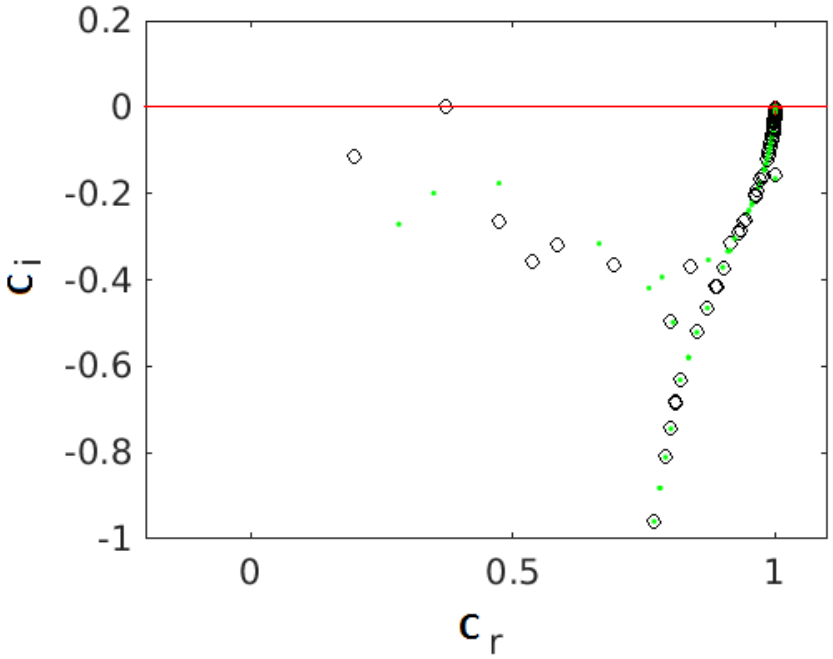

(b) Labelled incompressible LST eigenvalue spectrum for dominant perturbation amplitude per eigenvalue for $M = 10^{-3}, Re = 580, \alpha = 0.2, NC = 150$. Spurious and other non-physical modes are omitted. Black circles for $\tilde{u}$, red pluses for $\tilde{v}$, green dots for $\tilde{w}$ and blue diamonds for $\tilde{p}$.

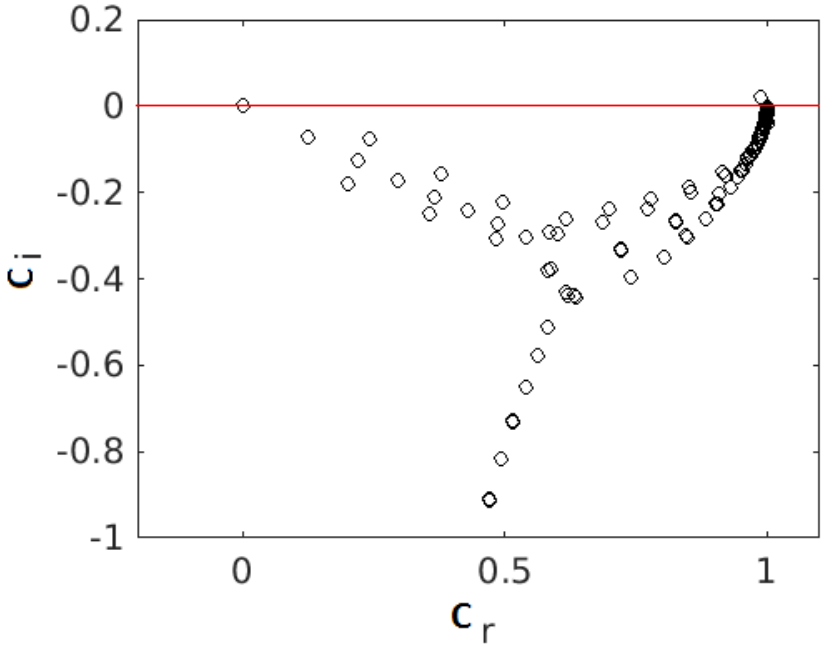

(a) Temporal eigenvalue spectrum for incompressible LST, with $M = 10^{-3}$, $Re = 580, \alpha = 0.8, NC = 150$.

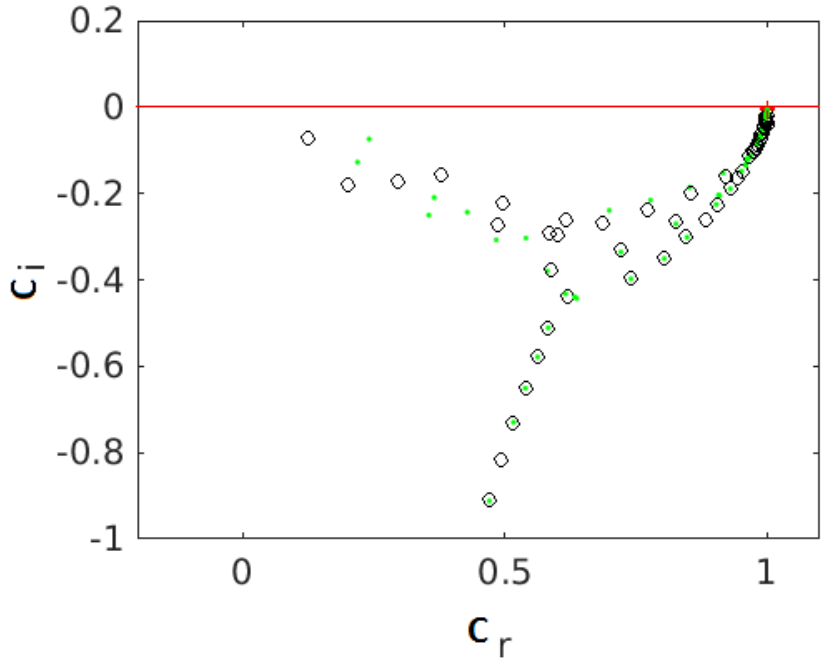

(b) Labelled incompressible LST eigenvalue spectrum for dominant perturbation amplitude per eigenvalue for $M = 10^{-3}, Re = 580, \alpha = 6, NC = 150$. Spurious and other non-physical modes are omitted. Black circles for $\tilde{u}$, red pluses for $\tilde{v}$, green dots for $\tilde{w}$ and blue diamonds for $\tilde{p}$.

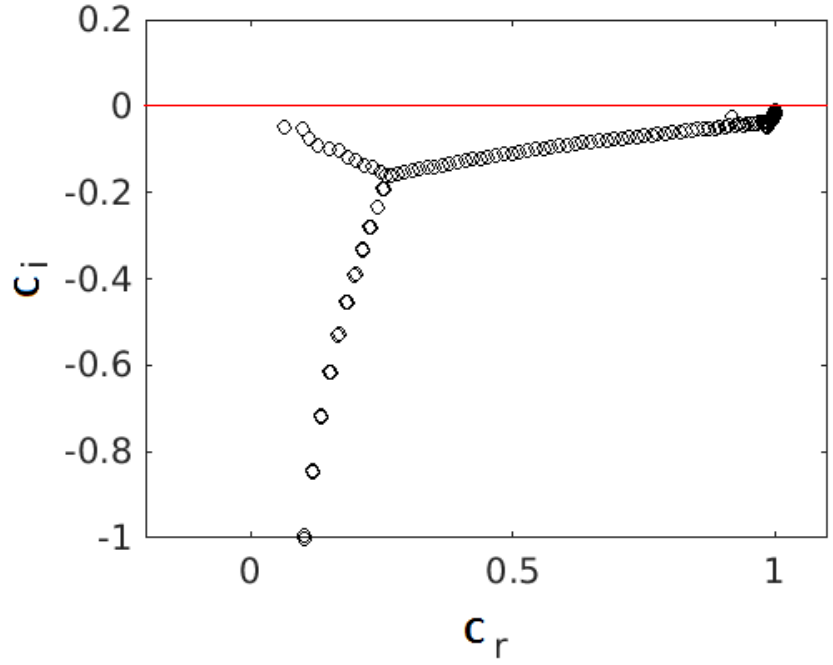

(a) Temporal eigenvalue spectrum for for incompressible LST, with $M = 10^{-3}$, $Re = 580, \alpha = 0.8, NC = 150$.

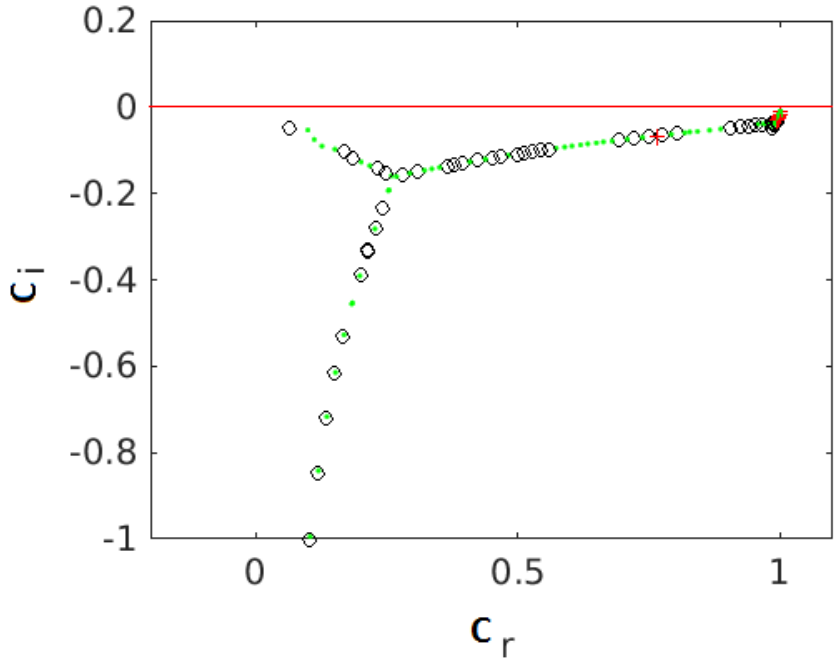

(b) Labelled incompressible LST eigenvalue spectrum for dominant perturbation amplitude per eigenvalue for $M = 10^{-3}, Re = 580, \alpha = 6, NC = 150$. Spurious and other non-physical modes are omitted. Black circles for $\tilde{u}$, red pluses for $\tilde{v}$, green dots for $\tilde{w}$ and blue diamonds for $\tilde{p}$.

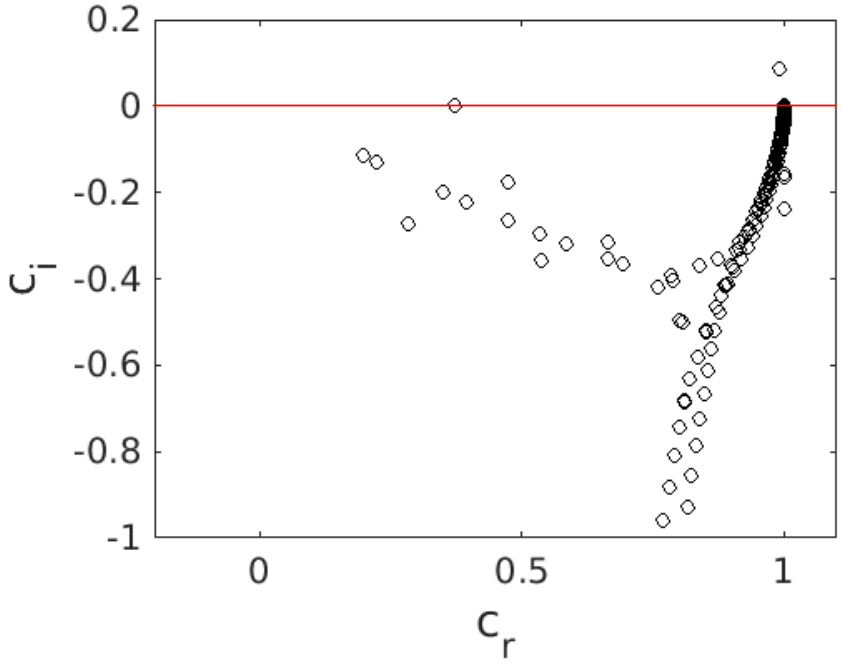

(a) Temporal eigenvalue spectrum for compressible LST, with $M = 10^{-3}, Re = 580, \alpha = 0.2, NC = 150$.

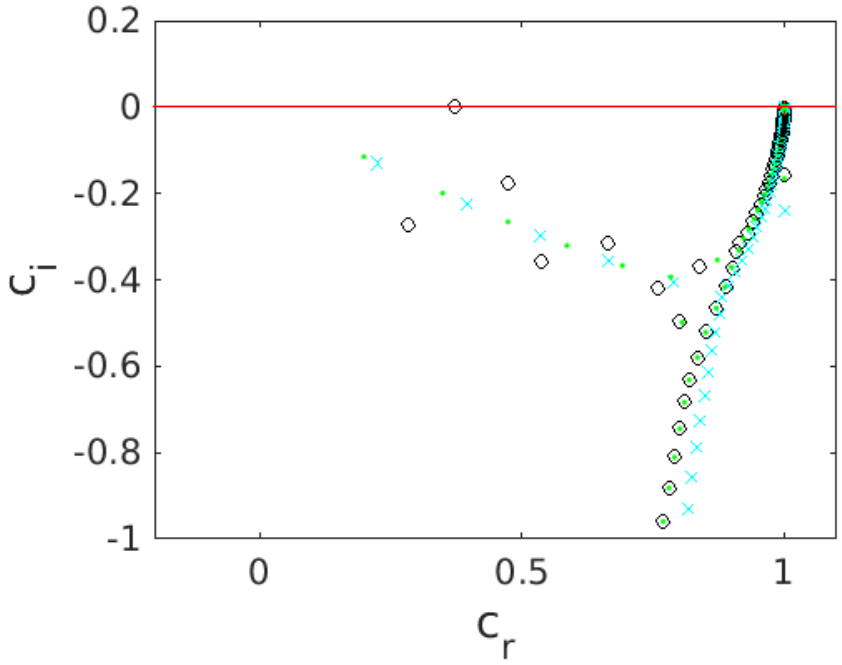

(b) Labelled compressible LST eigenvalue spectrum for dominant perturbation amplitude per eigenvalue for $M = 10^{-3}, Re = 580, \alpha = 0.2, NC = 150$. Spurious and other non-physical modes are omitted. Black circles for $\tilde{u}$, red pluses for $\tilde{v}$, green dots for $\tilde{w}$ and blue diamonds for $\tilde{p}$, and cyan crosses for $\tilde{T}$.

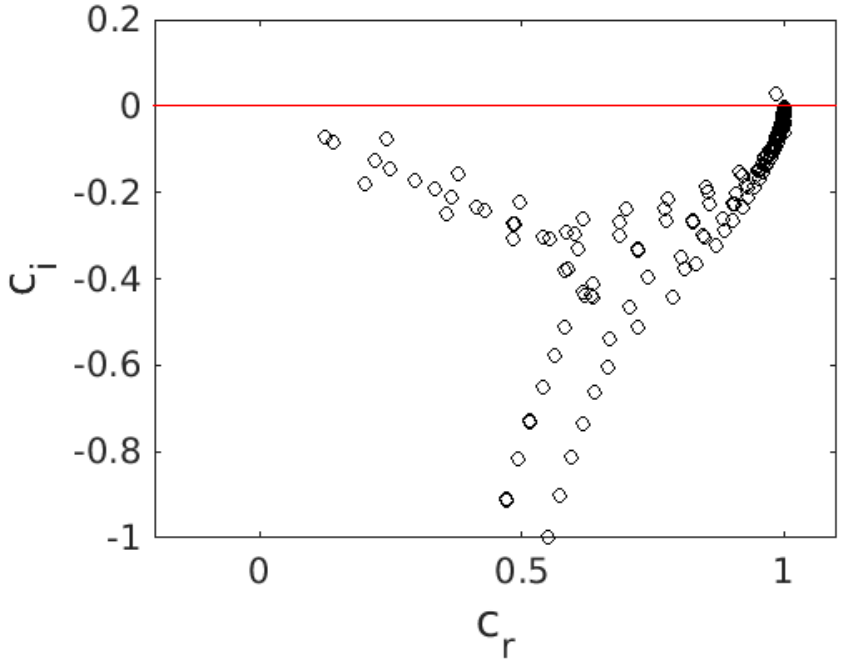

(a) Temporal eigenvalue spectrum for compressible LST, with $M = 10^{-3}$, $Re = 580, \alpha = 0.8, NC = 150$.

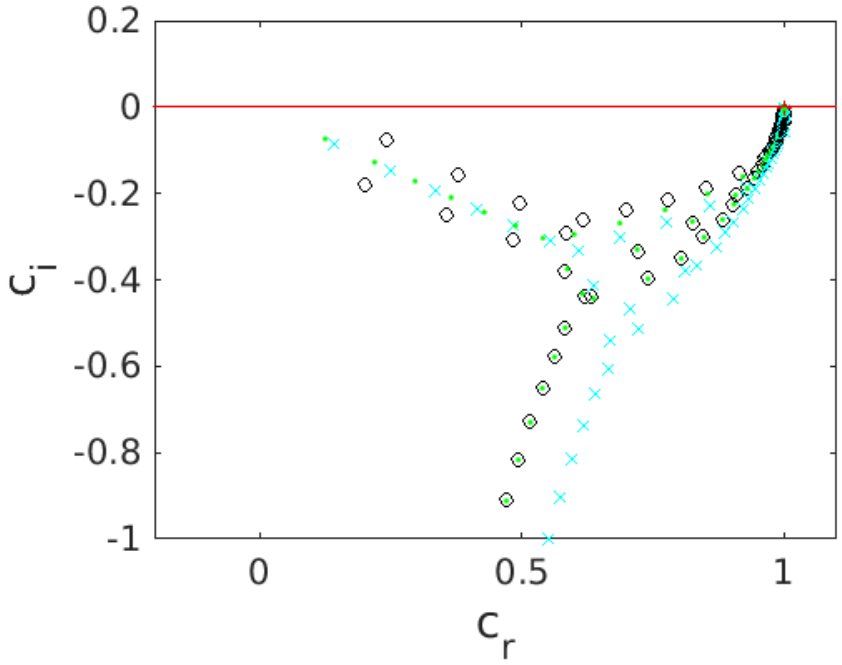

(b) Labelled compressible LST eigenvalue spectrum for dominant perturbation amplitude per eigenvalue for $M = 10^{-3}, Re = 580, \alpha = 6, NC = 150$. Spurious and other non-physical modes are omitted. Black circles for $\tilde{u}$, red pluses for $\tilde{v}$, green dots for $\tilde{w}$ and blue diamonds for $\tilde{p}$, and cyan crosses for $\tilde{T}$.

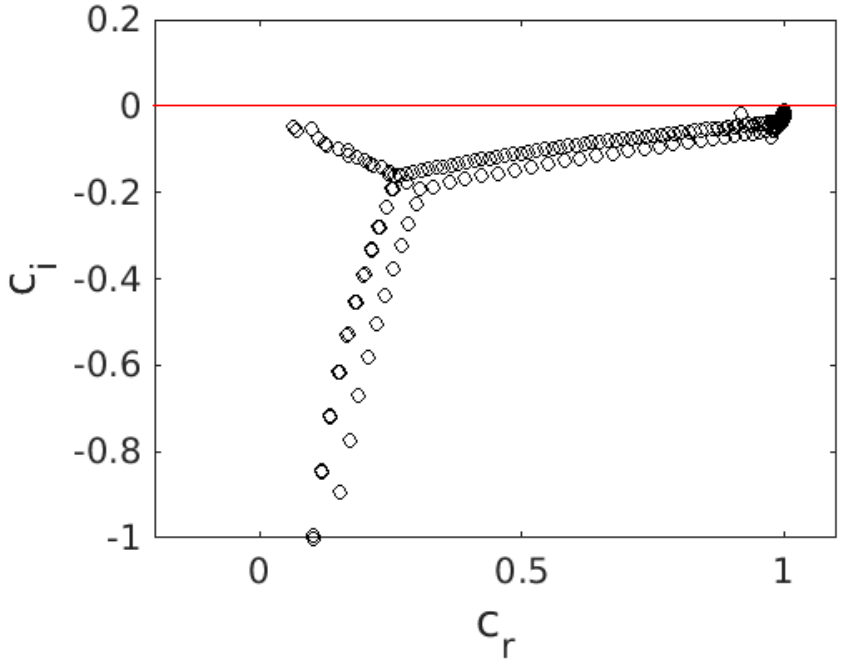

(a) Temporal eigenspectrum for compressible LST, with $M = 10^{-3}, Re = 580, \alpha = 0.8, NC = 150$.

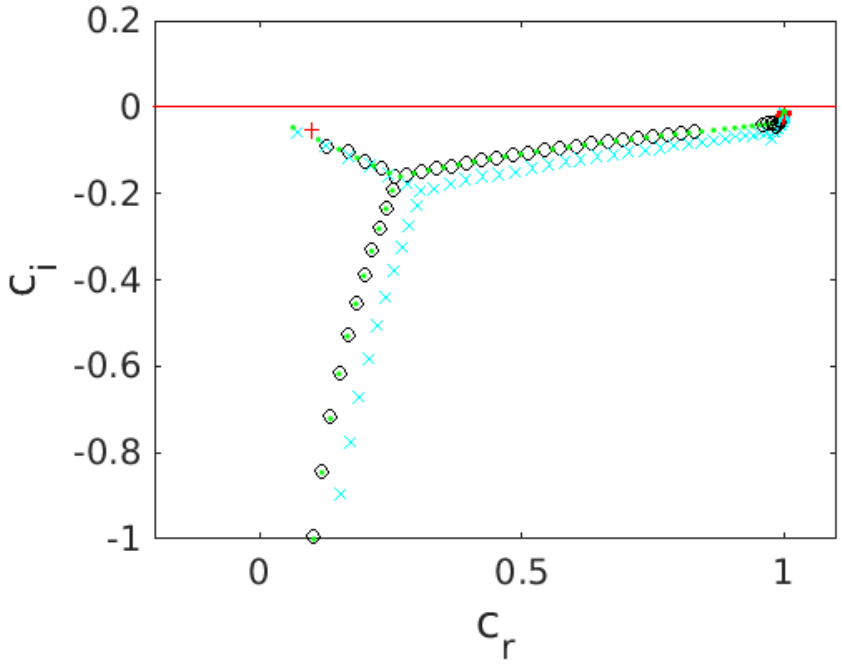

(b) Labelled compressible LST eigenvalue spectrum for dominant perturbation amplitude per eigenvalue for $M = 10^{-3}, Re = 580, \alpha = 6, NC = 150$. Spurious and other non-physical modes are omitted. Black circles for $\tilde{u}$, red pluses for $\tilde{v}$, green dots for $\tilde{w}$ and blue diamonds for $\tilde{p}$, and cyan crosses for $\tilde{T}$.

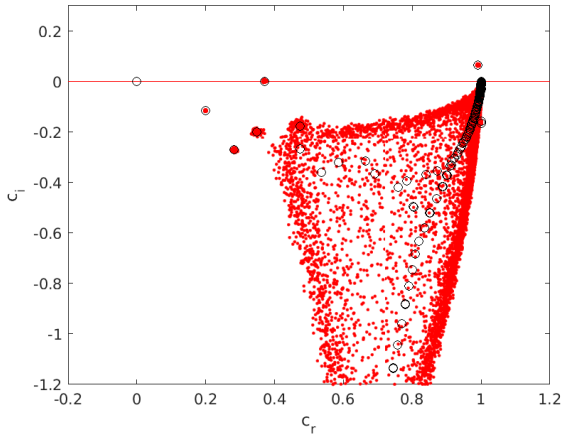

(a) $\mathcal{O}(\epsilon) = 10^{-4}$

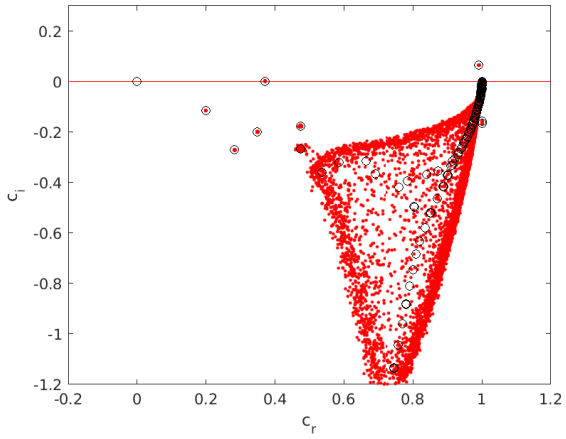

(b) $\mathcal{O}(\epsilon) = 10^{-5}$

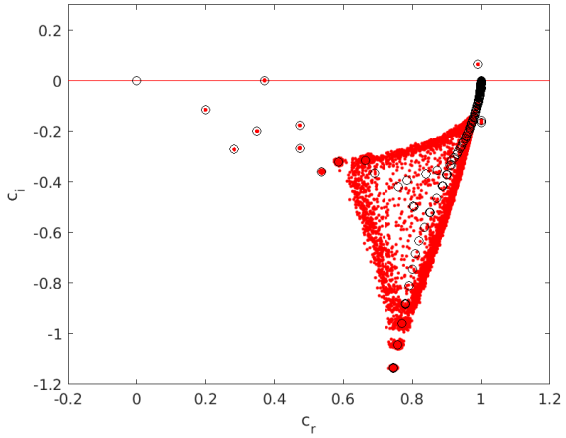

(c) $\mathcal{O}(\epsilon) = 10^{-6}$

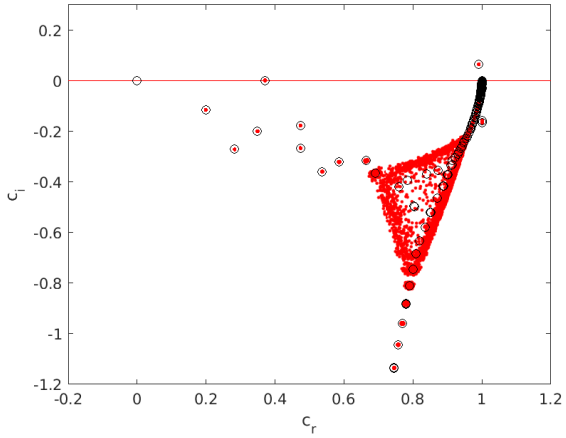

(d) $\mathcal{O}(\epsilon_{pert}) = 10^{-7}$

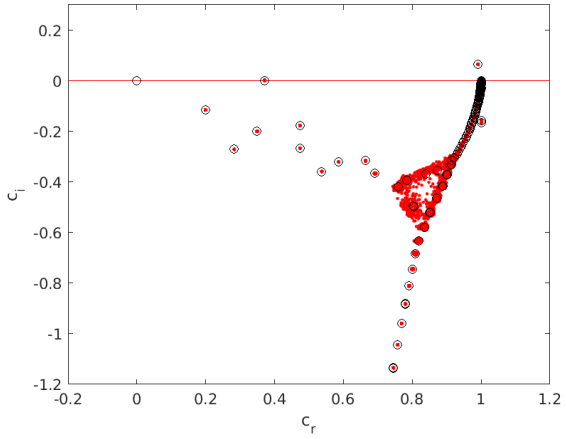

(e) $\mathcal{O}(\epsilon) = 10^{-8}$

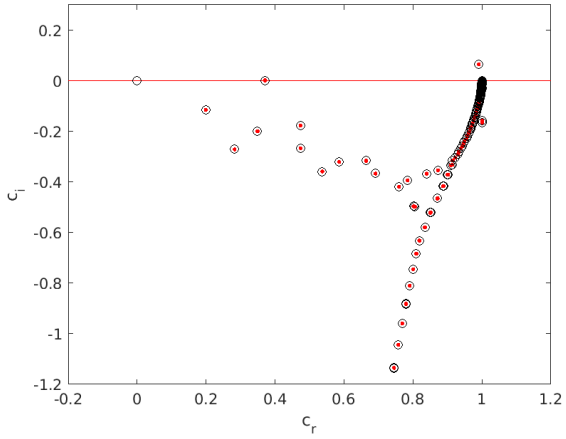

(f) $\mathcal{O}(\epsilon) = 10^{-10}$

Figure 5.7: Temporal eigenvalue spectra for the incompressible LST equations, with $M = 10^{-3}, Re = 580, \alpha = 0.2, NC = 150$. Perturbations from a normal distribution with a mean of 0 and a standard deviation of 1 for both the real and imaginary part are introduced for both the A and B matrices of the $(A - \omega B)q = 0$ generalised eigenvalue problem. The superposed perturbations are in the order of $\mathcal{O}(\epsilon) = 10^{-4}$ - $\mathcal{O}(\epsilon) = 10^{-10}$, respectively

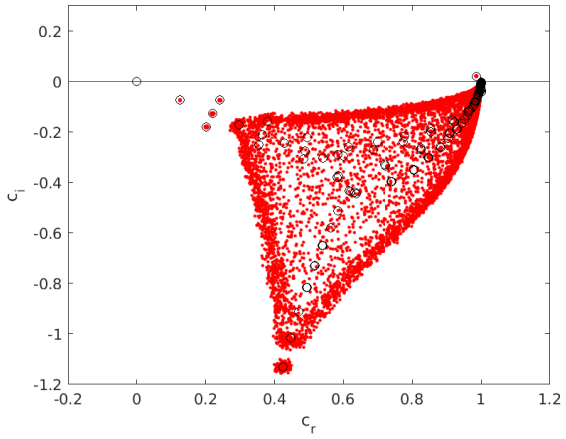

(a) $\mathcal{O}(\epsilon) = 10^{-4}$

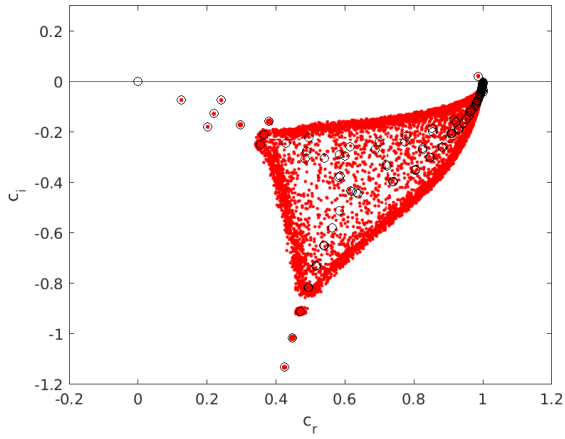

(b) $\mathcal{O}(\epsilon) = 10^{-5}$

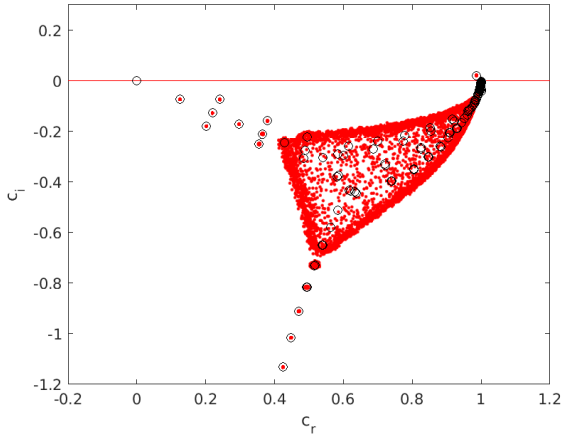

(c) $\mathcal{O}(\epsilon) = 10^{-6}$

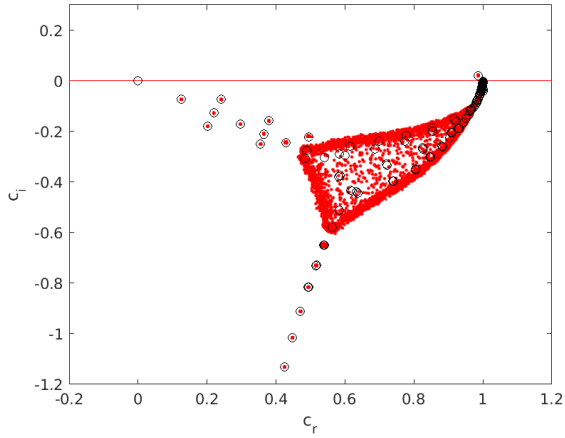

(d) $\mathcal{O}(\epsilon_{pert}) = 10^{-7}$

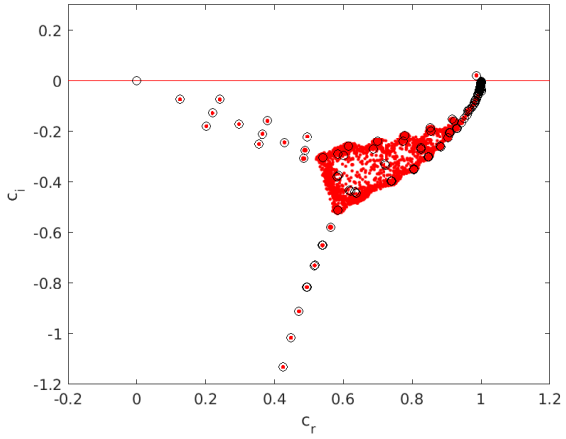

(e) $\mathcal{O}(\epsilon) = 10^{-8}$

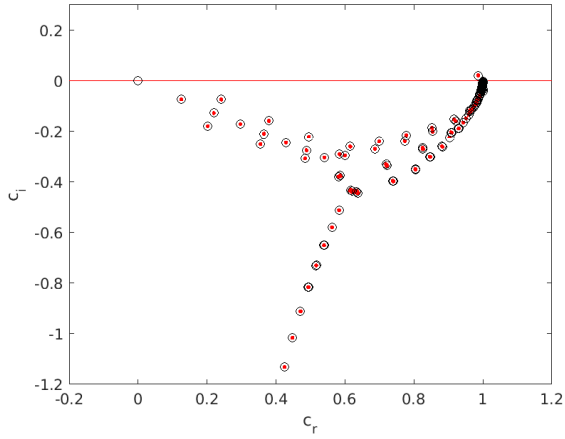

(f) $\mathcal{O}(\epsilon) = 10^{-10}$

Figure 5.8: Temporal eigenvalue spectra for the incompressible LST equations, with $M = 10^{-3}, Re = 580, \alpha = 0.8, NC = 150$. Complex perturbations from a normal distribution with a mean of 0 and a standard deviation of 1 for both the real and imaginary part are introduced for both the A and B matrices of the $(A - \omega B)q = 0$ generalised eigenvalue problem. The superposed perturbations are in the order of $\mathcal{O}(\epsilon) = 10^{-4}$ - $\mathcal{O}(\epsilon) = 10^{-10}$, respectively

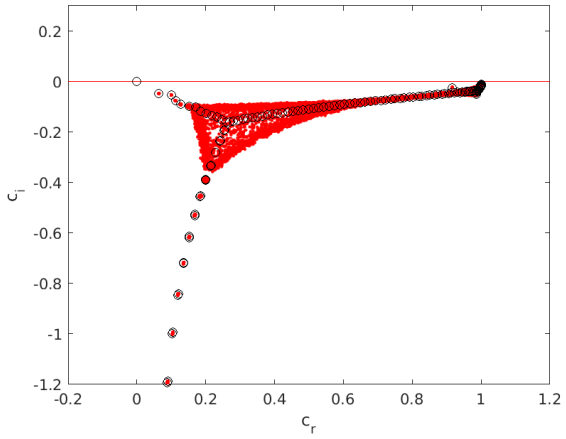

(a) $\mathcal{O}(\epsilon) = 10^{-4}$

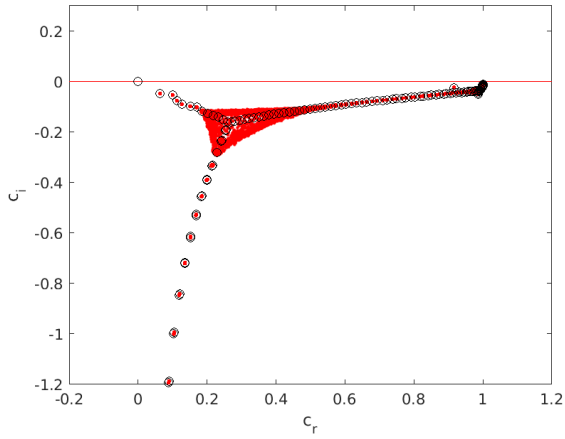

(b) $\mathcal{O}(\epsilon) = 10^{-5}$

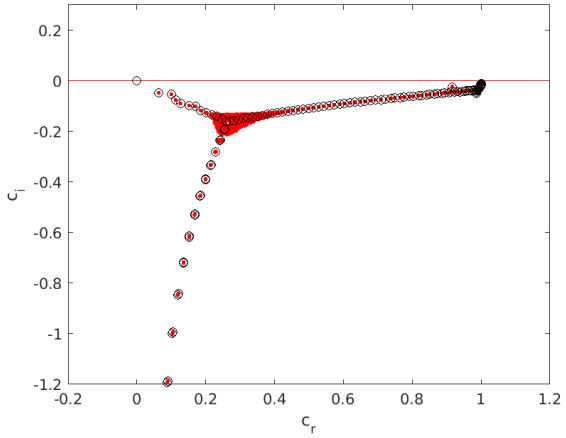

(c) $\mathcal{O}(\epsilon) = 10^{-6}$

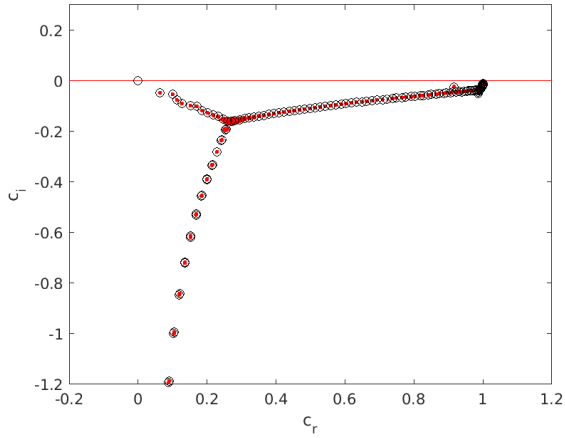

(d) $\mathcal{O}(\epsilon_{pert}) = 10^{-7}$

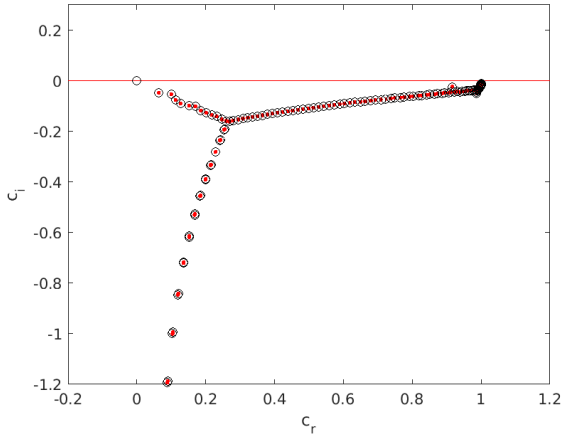

(e) $\mathcal{O}(\epsilon) = 10^{-8}$

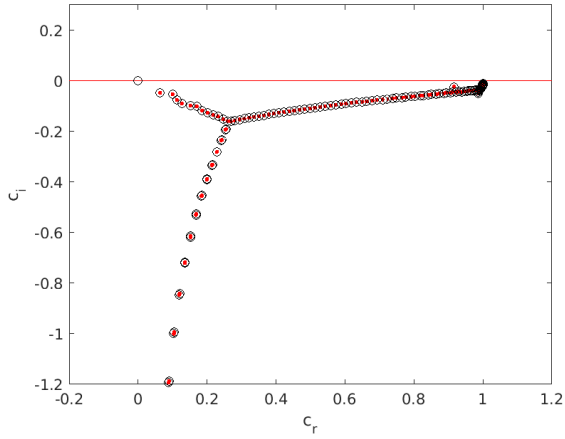

(f) $\mathcal{O}(\epsilon) = 10^{-10}$

Figure 5.9: Temporal eigenvalue spectra for the incompressible LST equations, with $M = 10^{-3}, Re = 580, \alpha = 6, NC = 150$. Complex perturbations from a normal distribution with a mean of 0 and a standard deviation of 1 for both the real and imaginary part are introduced for both the A and B matrices of the $(A - \omega B)q = 0$ generalised eigenvalue problem. The superposed perturbations are in the order of $\mathcal{O}(\epsilon) = 10^{-4}$ - $\mathcal{O}(\epsilon) = 10^{-10}$, respectively

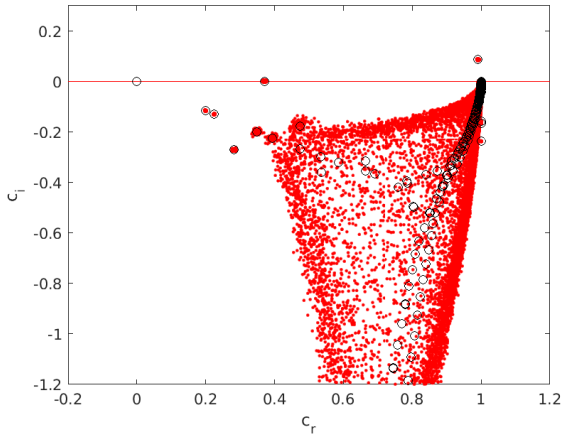

(a) $\mathcal{O}(\epsilon) = 10^{-4}$

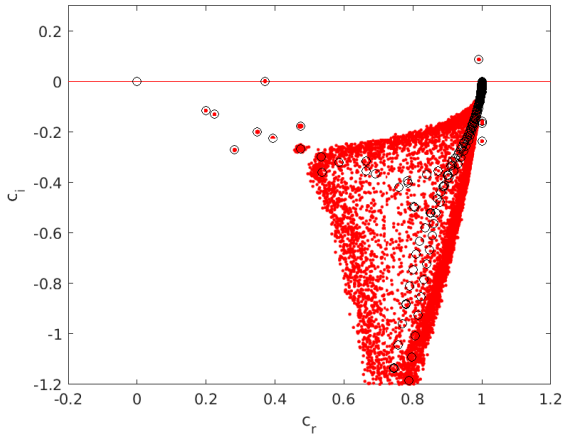

(b) $\mathcal{O}(\epsilon) = 10^{-5}$

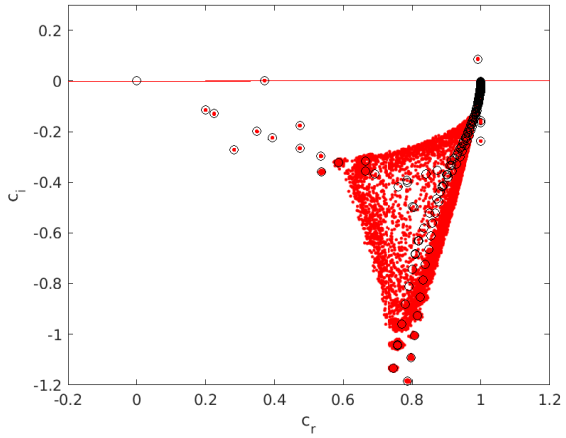

(c) $\mathcal{O}(\epsilon) = 10^{-6}$

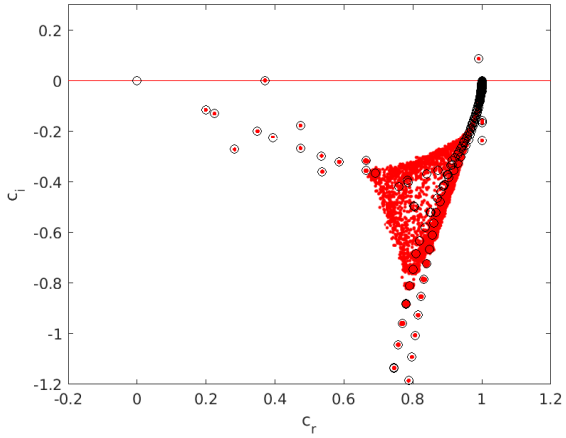

(d) $\mathcal{O}(\epsilon_{pert}) = 10^{-7}$

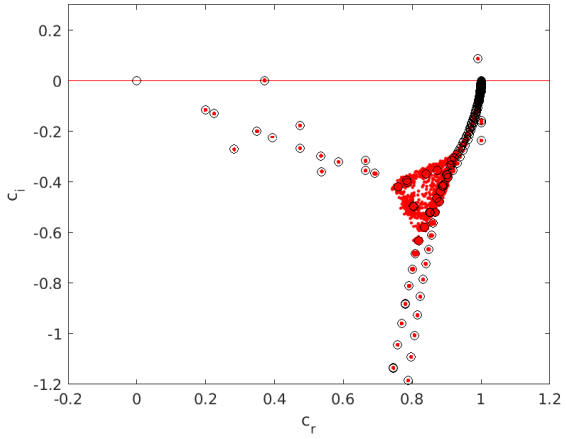

(e) $\mathcal{O}(\epsilon) = 10^{-8}$

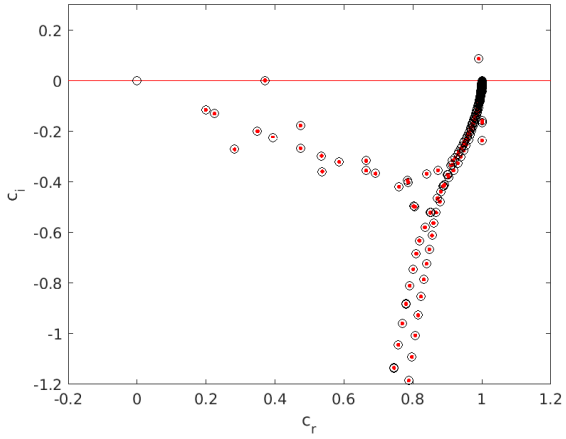

(f) $\mathcal{O}(\epsilon) = 10^{-10}$

Figure 5.10: Temporal eigenvalue spectra for the compressible LST equations, with $M = 10^{-3}, Re = 580, \alpha = 0.2, NC = 150$. Perturbations from a normal distribution with a mean of 0 and a standard deviation of 1 for both the real and imaginary part are introduced for both the A and B matrices of the $(A - \omega B)q = 0$ generalised eigenvalue problem. The imposed perturbations are in the order of $\mathcal{O}(\epsilon) = 10^{-4}$ - $\mathcal{O}(\epsilon) = 10^{-10}$, respectively

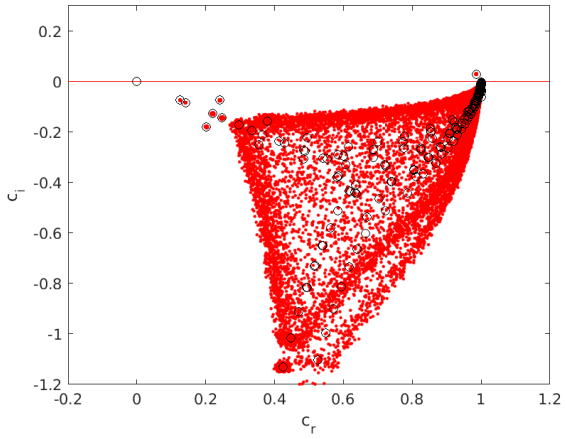

(a) $\mathcal{O}(\epsilon) = 10^{-4}$

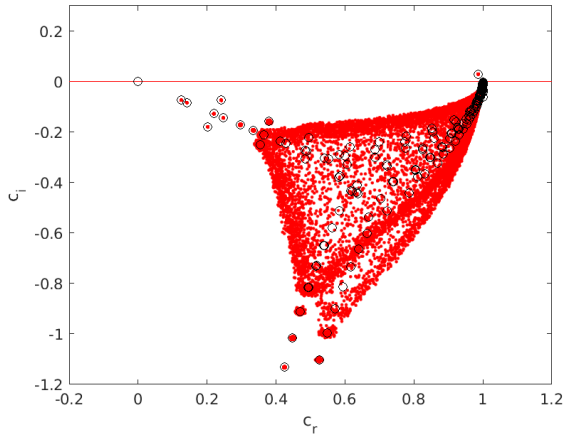

(b) $\mathcal{O}(\epsilon) = 10^{-5}$

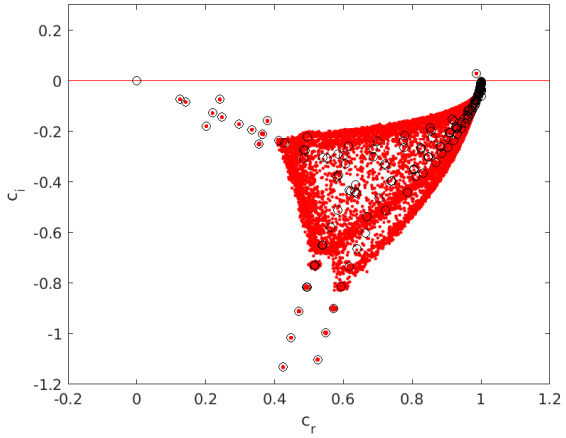

(c) $\mathcal{O}(\epsilon) = 10^{-6}$

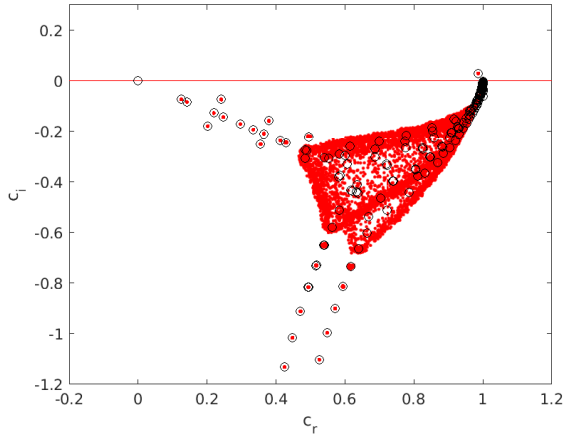

(d) $\mathcal{O}(\epsilon_{pert}) = 10^{-7}$

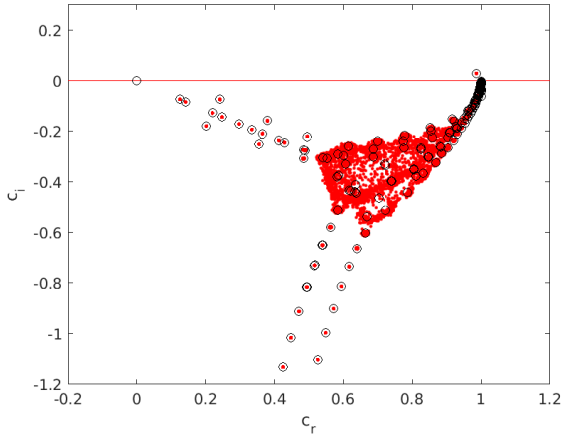

(e) $\mathcal{O}(\epsilon) = 10^{-8}$

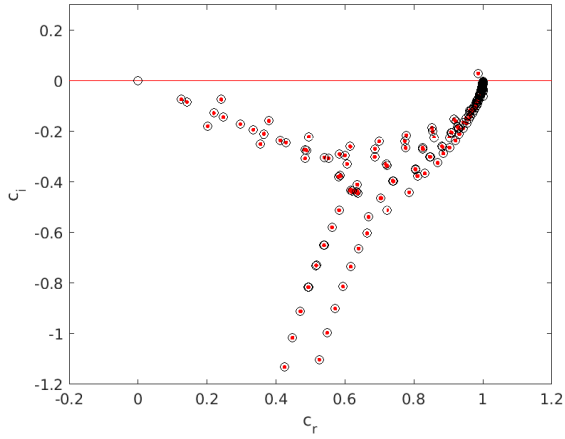

(f) $\mathcal{O}(\epsilon) = 10^{-10}$

Figure 5.11: Temporal eigenvalue spectra for the compressible LST equations, with $M = 10^{-3}, Re = 580, \alpha = 0.8, NC = 150$. Complex perturbations from a normal distribution with a mean of 0 and a standard deviation of 1 for both the real and imaginary part are introduced for both the A and B matrices of the $(A - \omega B)q = 0$ generalised eigenvalue problem. The imposed perturbations are in the order of $\mathcal{O}(\epsilon) = 10^{-4}$ - $\mathcal{O}(\epsilon) = 10^{-10}$, respectively

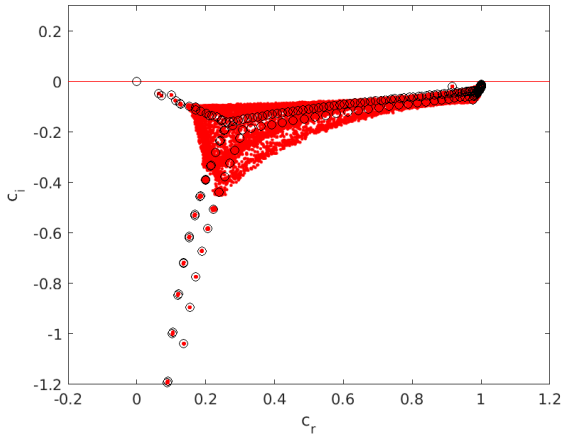

(a) $\mathcal{O}(\epsilon) = 10^{-4}$

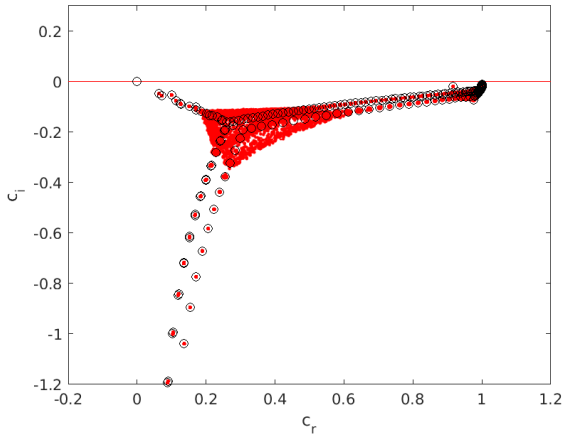

(b) $\mathcal{O}(\epsilon) = 10^{-5}$

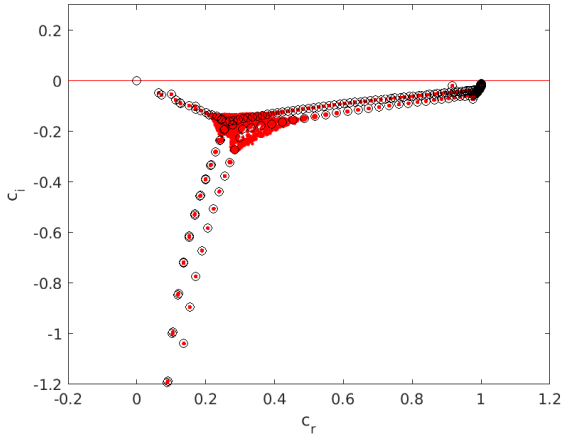

(c) $\mathcal{O}(\epsilon) = 10^{-6}$

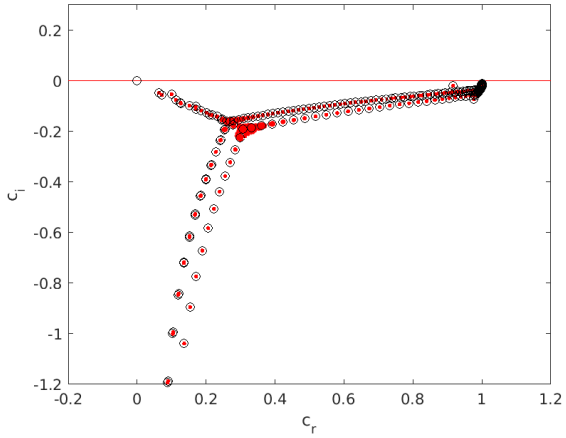

(d) $\mathcal{O}(\epsilon_{pert}) = 10^{-7}$

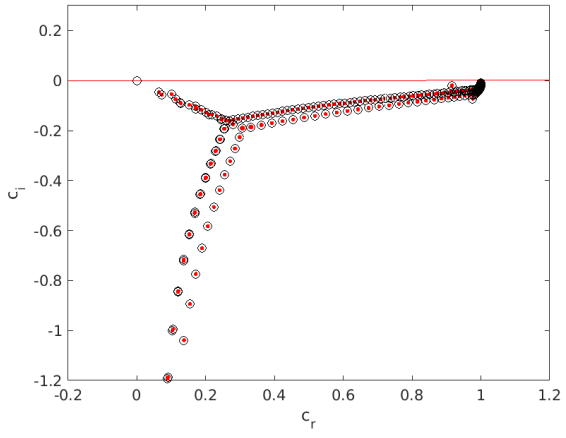

(e) $\mathcal{O}(\epsilon) = 10^{-8}$

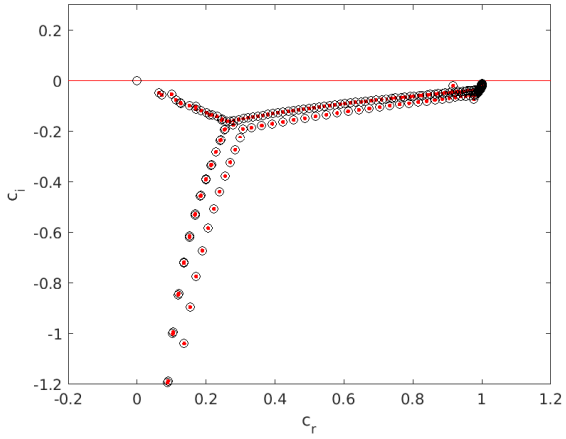

(f) $\mathcal{O}(\epsilon) = 10^{-10}$

Figure 5.12: Temporal eigenvalue spectra for the compressible LST equations, with $M = 10^{-3}, Re = 580, \alpha = 6, NC = 150$. Complex perturbations from a normal distribution with a mean of 0 and a standard deviation of 1 for both the real and imaginary part are introduced for both the A and B matrices of the $(A - \omega B)q = 0$ generalised eigenvalue problem. The imposed perturbations are in the order of $\mathcal{O}(\epsilon) = 10^{-4}$ - $\mathcal{O}(\epsilon) = 10^{-10}$, respectively

6

Perturbations of the streamwise velocity base flow profile

In this chapter we will first briefly discuss the reference streamwise velocity base flow profile in Section 6.1. Then we will present temporal eigenspectra of the incompressible and compressible LST operators for perturbations of the streamwise velocity base flow profile. These perturbations will be imposed (1) on the entire profile (in Section 6.2), (2) in the wall region (in Section 6.3), (3) in a middle region (in Section 6.5) and (4) in the top-layer near the free-stream edge in (Section 6.5). Finally, we will present our initial conclusions in Section 6.6.

6.1. Reference streamwise velocity base flow profile

The basic state used in this chapter is the same as in Chapter 5: the Falkner-Skan-Cooke boundary layer flow computed by Groot [5] using the DEKAF boundary-layer solver. For reference, the lower regions of the streamwise velocity base flow profile of this basic state are shown in Figure 6.1. Note that the bottom blue line in this Figure represents $\delta_{25} \rightarrow \tilde{u}/U_e \approx 25\%$ amd that the top blue line represents $\delta_{99} \rightarrow \tilde{u}/U_e \approx 99\%$. The perturbations in the wall region will be imposed on the region between the wall up to δ_{25}. The perturbations in the middle region will be imposed on the region between δ_{25} to δ_{99}.

6.2. Perturbations of the entire profile

To determine how the eigenvalue spectrum of the LST operator is affected by perturbations on the base flow profile eigenspectra are computed for the incompressible and compressible LST equations, for a perturbed streamwise velocity base flow profile $u(y) + E(y)$, with $E(y) \sim \mathcal{O}(\epsilon)$. The incompressible and compressible EVPs are solved for $M = 10^{-3}, Re = 580, NC = 150, \alpha = [0.2, 0.8, 6]$, with $E(y)$ containing random, complex perturbation elements picked from a normal distribution with a mean of 0 and a standard deviation of 1 and multiplied with a factor of $\mathcal{O}(\epsilon)$.

The perturbation elements are imposed for $\mathcal{O}(\epsilon) = 10^{-4}$ - $\mathcal{O}(\epsilon) = 10^{-10}$, with 100 random cases for each $\mathcal{O}(\epsilon)$. The $\frac{\partial u}{\partial y}$ and $\frac{\partial^2 u}{\partial y^2}$ profiles corresponding to the perturbed base flow profile are determined using Chebyshev differential spectral matrices, so as to be consistent with the unperturbed EVP.

Both for the incompressible and the compressible eigenproblem computations the algorithm precision is in the order of $\leq \mathcal{O}(10^{-12})$ for all perturbation levels $\mathcal{O}(\epsilon) = 10^{-4}$ - $\mathcal{O}(\epsilon) = 10^{-10}$, respectively. This indicates a reliable result, with minimal eigenvalue error.

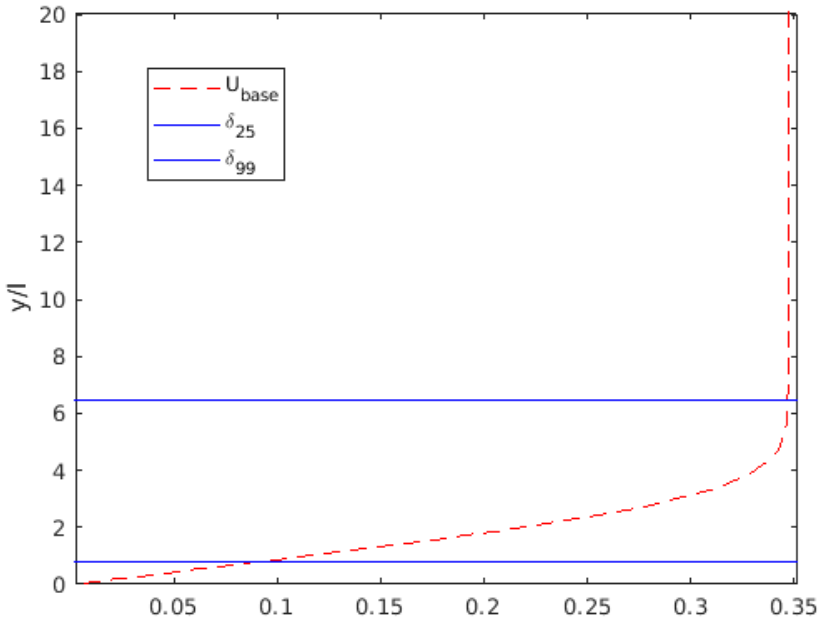

Figure 6.1: Zoom on the lower regions of the streamwise velocity base flow profile of the basic state [5] used in this work. The bottom blue line represents $\delta_{25} \rightarrow \tilde{u}/U_e \approx 25\%$. The top blue line represents $\delta_{99} \rightarrow \tilde{u}/U_e \approx 99\%$.

Observations and comparison with matrix perturbations

The perturbations imposed on the base flow appear to initiate a disturbance pattern in both the incompressible and compressible spectra that is similar to that of the matrix perturbations in Chapter 5: the initial disturbance can be seen at the intersection of the continous branch and the discrete set of modes. For increasing perturbation size the disturbance of the spectrum then starts to spread outward.

Again, for larger perturbations the incompressible and compressible eigenvalues describe a contour within which most of the 'pseudo-eigenvalues' are contained in a relatively noisy pattern. As such, some eigenvalues shift further from the 'original' unperturbed location than the order of magnitude of the imposed perturbations would dictate. For $\alpha = 0.8$ and smaller, the spectrum starts to visibly shift relative to the unperturbed set of eigenvalues for $\mathcal{O}(\epsilon) = 10^{-8}$ and larger .

As with the matrix perturbations, the discrete wall modes with small c_r and the continous 'free-stream'-modes for which $c_r \rightarrow 1$ move less for a certain-sized perturbation than the modes for which c_r is mid-range. Even for relatively large sized perturbations there is very little movement of these particular modes.

A comparison is made between the compressible pseudospectra for a perturbation of $\mathcal{O}(\epsilon) = 10^{-4}$ in Figure 5.10a and the superposition of eigenspectra for a perturbed baseflow with $\mathcal{O}(\epsilon) = 10^{-4}$ in Figure 6.3a. These Figures indicate that for this perturbation-size the contour of the superimposed eigenvalues seems to have spread ever so slightly further towards the free-stream modes and the discrete wall modes for the pseudospectra when compared with the perturbed base flow eigenspectra.

6.3. Perturbations in the wall region

The perturbations for this analysis were imposed on the base flow profile in the wall region. This wall region was defined from the wall up to $u/U_e \approx 0.25$. The perturbation elements are again picked from a normal distribution with a mean of 0, and a standard deviation of 1. These random elements are then multiplied with a factor of order epsilon. Note that the boundary no-slip condition of $U_w = 0$ was maintainted. The first and second order derivatives corresponding to the perturbed base flow profile are obtained by means of Chebyshev differential spectral matrices.

Observations

A first observation when considering the superimposed eigenspectra for the wall region perturbations is that the disturbance pattern no longer seems to be often of the random, noisy type. For larger sized perturbations the superimposed modes at the intersection between the discrete modes and the continous modes, and the superimposed modes along the continuous branch are distributed along distinct lines. For $\alpha = 0.2$ these eigenvalues start to visibly move relative to the unperturbed set of eigenvalues for $\mathcal{O}(\epsilon) = 10^{-7}$ and larger. Do note that for every perturbation-level the eigenspectrum appears more robust to base flow perturbations in this specific wall region, when compared with the entire profile.

Interestingly, the wall modes, which are dominant in this near-wall region (see e.g. Figure 4.4, do not seem to be affected by a perturbation in this specific region. Even for $\mathcal{O}(\epsilon) = 10^{-5}$, for $\alpha = 0.2$, the most right eigenvalues in the discrete set of modes demonstrate very little movement.

6.4. Perturbations in a middle region

The perturbations for this analysis were imposed on the base flow profile in a middle region. This middle region was defined from the $u/U_e \approx 0.25$ up to $u/U_e \approx 0.99$. The perturbation elements are again picked from a normal distribution with a mean of 0, and a standard deviation of 1. These random elements are then multiplied with a factor of order epsilon. The first and second order derivatives corresponding to the perturbed base flow profile are obtained by means of Chebyshev differential spectral matrices.

Observations

Unlike for the wall region, the disturbance patterns that can be observed in the superimposed eigenvalue spectra for middle region perturbations are very similar to those seen for the entire base flow and/or generic matrix perturbations. The eigenvalues for larger sized perturbations do provide a contour within which a noisy pattern of eigenvalues is contained. However, the distribution of eigenvalues does appear denser towards the 'edges' of said contour when compared with the contours for perturbations of the entire profile or that of matrix perturbations.

For $\alpha = 0.2$ the spectrum starts to visibly shift relative to the unperturbed set of eigenvalues for perturbatinos of $\mathcal{O}(\epsilon) = 10^{-7}$ and larger. The eigenvalue shift oberved is also larger for most of the eigenvalues as compared to the wall region perturbations.

Again, as with all the previous analysis, the discrete wall modes with small c_r and the continous 'free-stream'-modes for which $c_r \to 1$ demonstrate very little movement.

6.5. Perturbations in a top layer at the edge

The perturbations for this analysis were imposed on the base flow profile in a top layer, near the free-stream edge. This top region was defined for the approx. top 50% of the top layer for which $u/U_e \approx 0.99$. The perturbation elements are again picked from a normal distribution with a mean of 0, and a standard deviation of 1. These random elements are then multiplied with a factor of order epsilon. The first and second order derivatives corresponding to the perturbed base flow profile are obtained by means of Chebyshev differential spectral matrices.

An analogy for these perturbations might for example be deviations in the input data resulting from a disturbance in the far field.

Observations

The eigenvalue shift pattern for the perturbations in the top layer follows a pattern similar to that of perturbations in the wall region. Eigenvalues at the intersection between the discrete modes and the continous branch are distributed along disinct lines. For perturbations of $\mathcal{O}(\epsilon) = 10^{-6}$ and larger, for $\alpha = 0.2$, visible eigenvalue movement relative to the unperturbed spectrum is to be observed. Compared to the wall region perturbations, it seems that the eigenvalues in this analysis demonstrate less movement for a certain perturbation.

In agreement with all the previous analyses, some eigenvalues barely shift. The discrete wall modes with small c_r and the continous 'free-stream'-modes for which $c_r \to 1$ demonstrate very little movement.

6.6. Conclusions

Perturbing the entire base flow profile produces superimposed eigenspectra that are similar to the pseudospectra in Chapter 5. There are indications that for a certain sized perturbation (slightly) fewer eigenvalues demonstrate visible movement for the perturbed base flow than for the matrix perturbations.

Perturbations in specific regions of the base flow indicated that perturbations in a middle region would most strongly affect the eigenvalues in that there was relatively more eigenvalue shift when compared with perturbations in just the wall region or the top layer. Additionally, it was only perturbations in the middle region that lead to the previously seen contour within which most of the 'pseudo-eigenvalues' are contained in a relatively noisy pattern. For both the wall region and top layer perturbations, the superimposed modes at the intersection between the discrete modes and the continous modes, and the superimposed modes along the continuous branch were found to be distributed along distinct lines. There are indications that the spectrum is slightly more robust to perturbations in the top layer than in the wall region.

Counterintuitively, the wall modes, which are dominant in the near-wall region did not seem to be affected by a perturbation of the base flow in this specific region. This provides an interesting result in that specific errors in the input data, e.g. due to difficulties in measuring the near-wall region, may not necessarily lead to an eigenvalue shift of the TS-mode. Thereby rendering the long-term stability information from this eigenvalue rather robust.

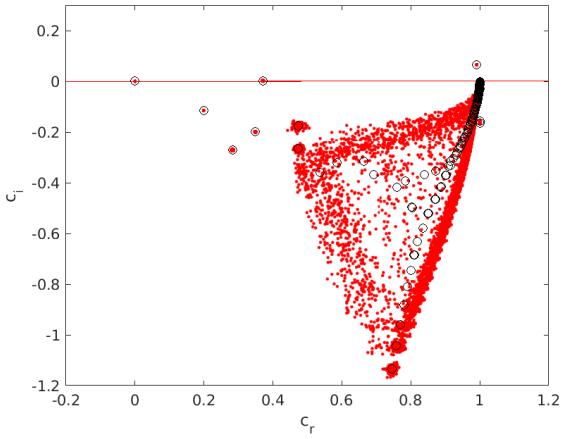

(a) $\mathcal{O}(\epsilon) = 10^{-4}$

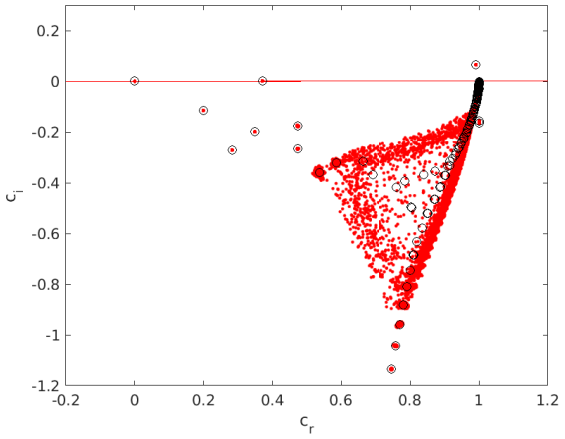

(b) $\mathcal{O}(\epsilon) = 10^{-5}$

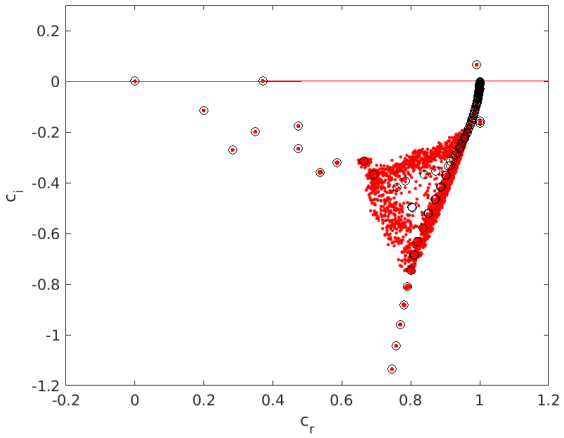

(c) $\mathcal{O}(\epsilon) = 10^{-6}$

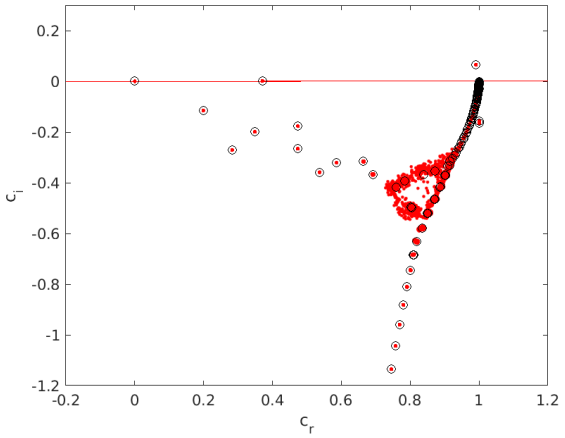

(d) $\mathcal{O}(\epsilon_{pert}) = 10^{-7}$

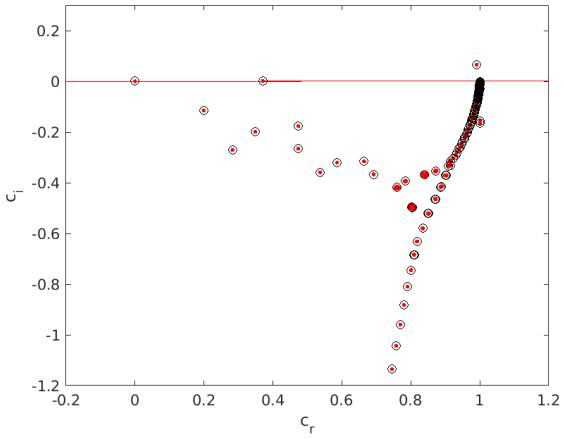

(e) $\mathcal{O}(\epsilon) = 10^{-8}$

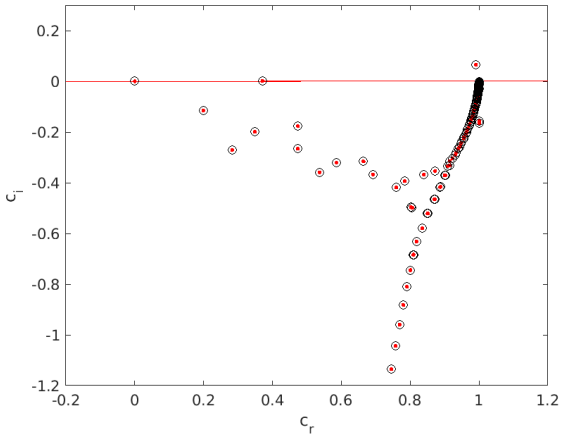

(f) $\mathcal{O}(\epsilon) = 10^{-10}$

Figure 6.2: Temporal eigenvalue spectra for the incompressible LST equations, with $M = 10^{-3}, Re = 580, \alpha = 0.2, NC = 150$. Perturbations from a normal distribution with a mean of 0 and a standard deviation of 1 are introduced for the entire streamwise velocity base flow profile. The superimposed perturbations are in the order of $\mathcal{O}(\epsilon) = 10^{-4}$ - $\mathcal{O}(\epsilon) = 10^{-10}$, respectively

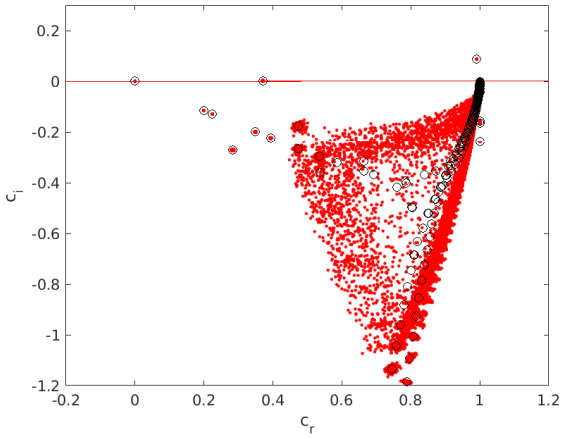

(a) $\mathcal{O}(\epsilon) = 10^{-4}$

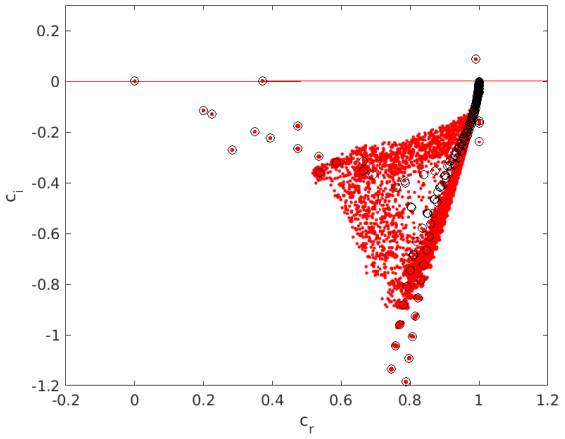

(b) $\mathcal{O}(\epsilon) = 10^{-5}$

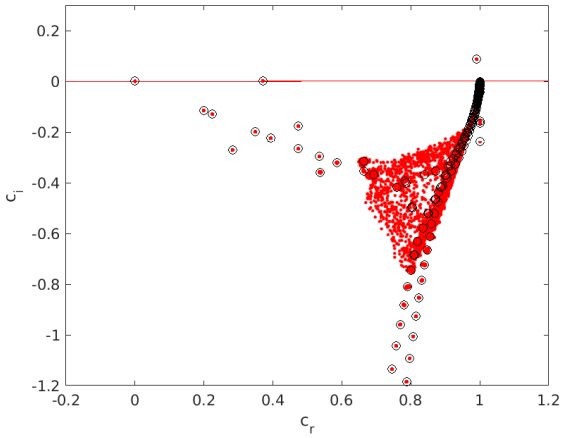

(c) $\mathcal{O}(\epsilon) = 10^{-6}$

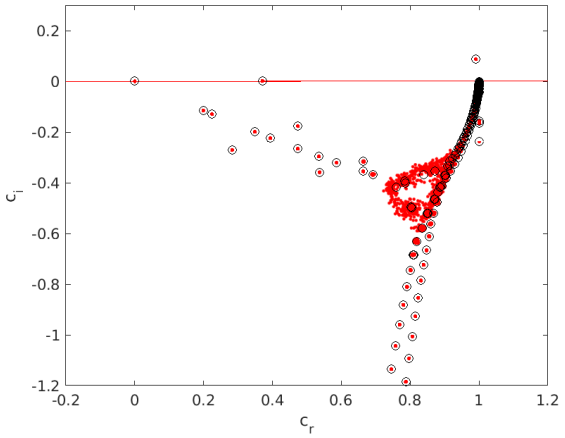

(d) $\mathcal{O}(\epsilon_{pert}) = 10^{-7}$

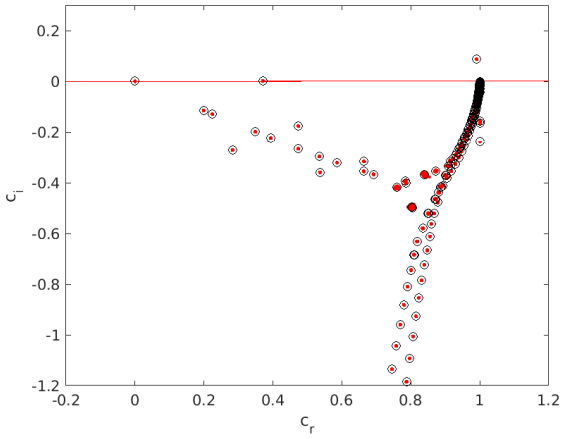

(e) $\mathcal{O}(\epsilon) = 10^{-8}$

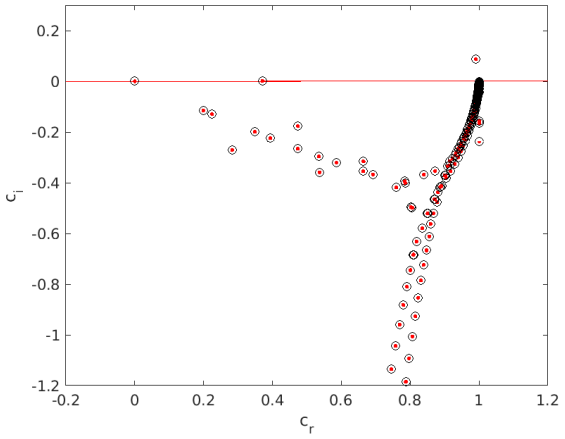

(f) $\mathcal{O}(\epsilon) = 10^{-10}$

Figure 6.3: Temporal eigenvalue spectra for the compressible LST equations, with $M = 10^{-3}, Re = 580, \alpha = 0.2, NC = 150$. Perturbations from a normal distribution with a mean of 0 and a standard deviation of 1 are introduced for the entire streamwise velocity base flow profile. The superimposed perturbations are in the order of $\mathcal{O}(\epsilon) = 10^{-4}$ - $\mathcal{O}(\epsilon) = 10^{-10}$, respectively

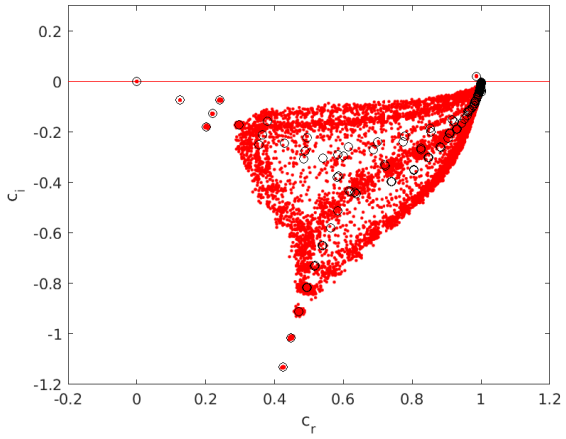

(a) $\mathcal{O}(\epsilon) = 10^{-4}$

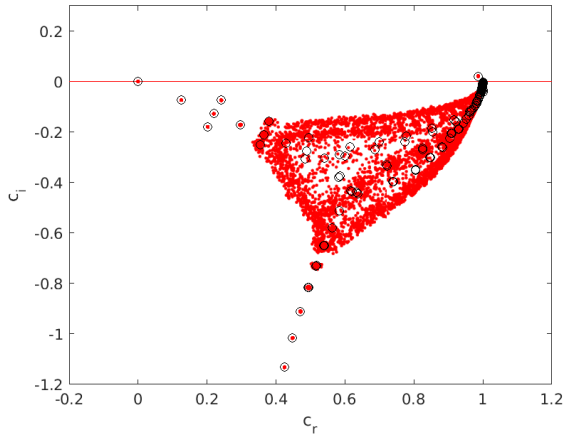

(b) $\mathcal{O}(\epsilon) = 10^{-5}$

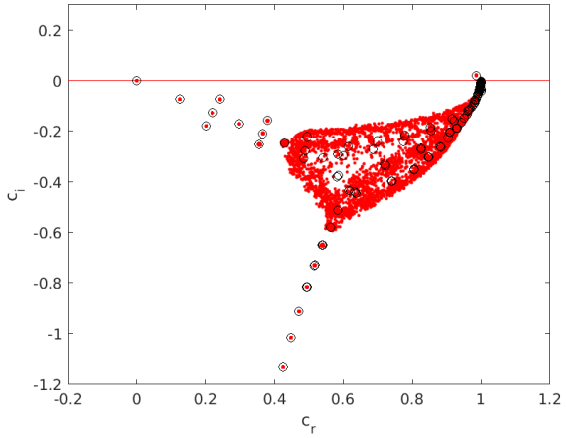

(c) $\mathcal{O}(\epsilon) = 10^{-6}$

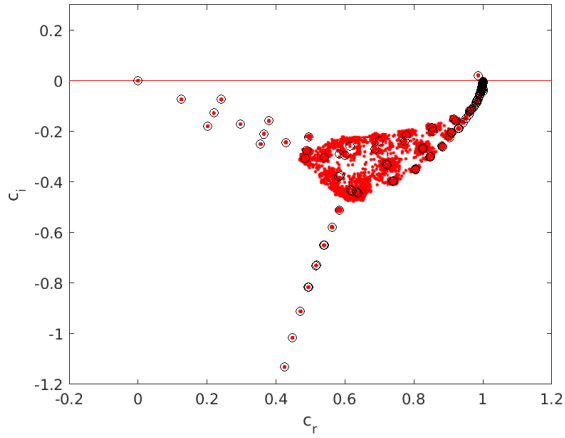

(d) $\mathcal{O}(\epsilon_{pert}) = 10^{-7}$

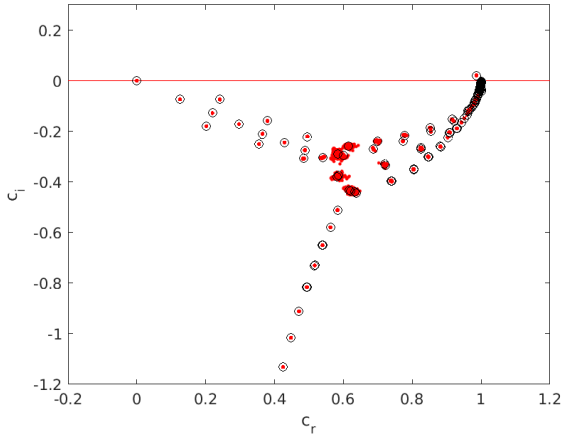

(e) $\mathcal{O}(\epsilon) = 10^{-8}$

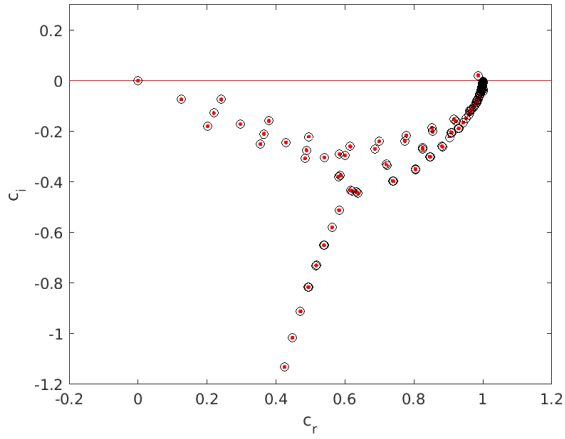

(f) $\mathcal{O}(\epsilon) = 10^{-10}$

Figure 6.4: Temporal eigenvalue spectra for the incompressible LST equations, with $M = 10^{-3}, Re = 580, \alpha = 0.8, NC = 150$. Perturbations from a normal distribution with a mean of 0 and a standard deviation of 1 are introduced for the entire streamwise velocity base flow profile. The imposed perturbations are in the order of $\mathcal{O}(\epsilon) = 10^{-4}$ - $\mathcal{O}(\epsilon) = 10^{-10}$, respectively

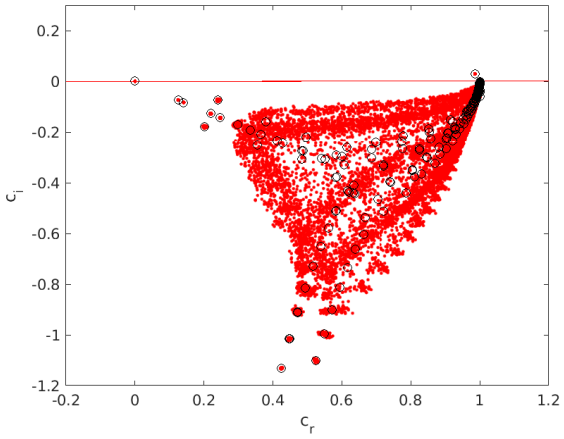

(a) $\mathcal{O}(\epsilon) = 10^{-4}$

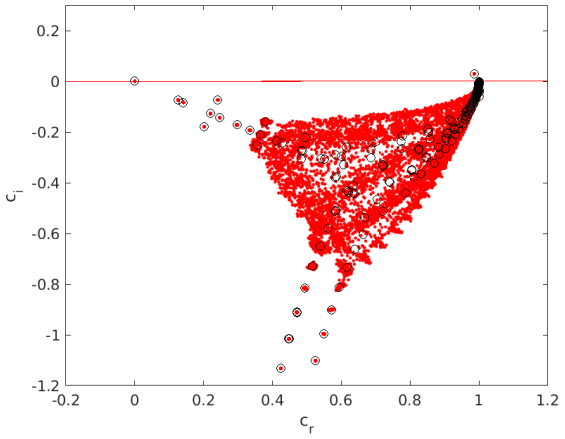

(b) $\mathcal{O}(\epsilon) = 10^{-5}$

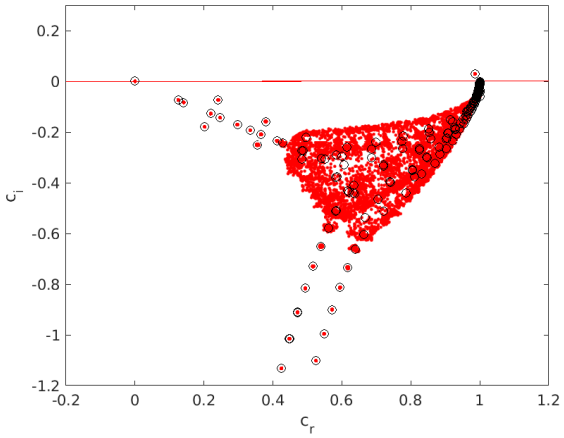

(c) $\mathcal{O}(\epsilon) = 10^{-6}$

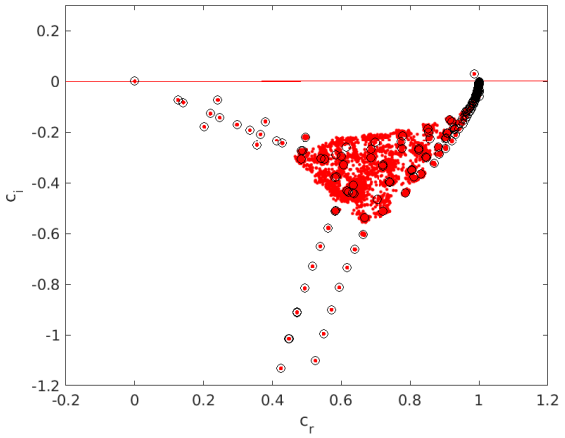

(d) $\mathcal{O}(\epsilon_{pert}) = 10^{-7}$

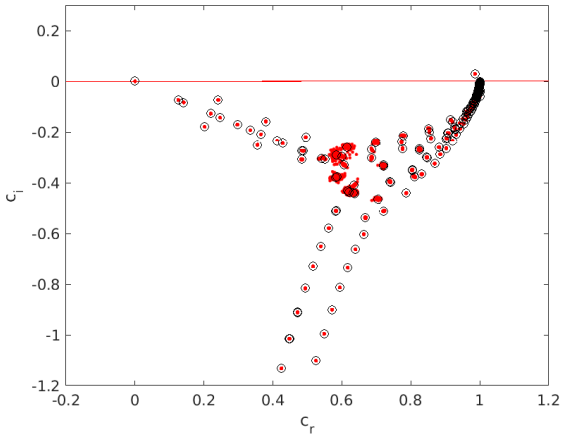

(e) $\mathcal{O}(\epsilon) = 10^{-8}$

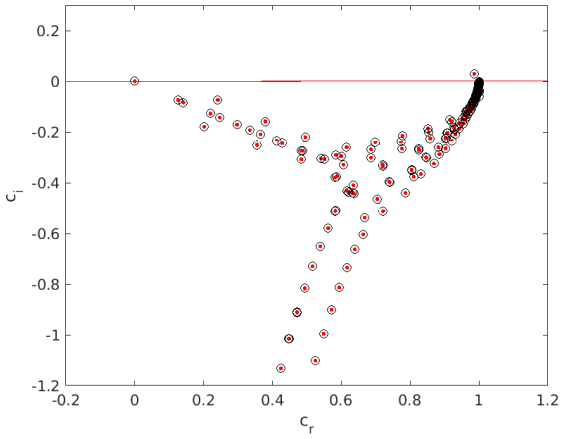

(f) $\mathcal{O}(\epsilon) = 10^{-10}$

Figure 6.5: Temporal eigenvalue spectra for the compressible LST equations, with $M = 10^{-3}, Re = 580, \alpha = 0.8, NC = 150$. Perturbations from a normal distribution with a mean of 0 and a standard deviation of 1 are introduced for the entire streamwise velocity base flow profile. The superimposed perturbations are in the order of $\mathcal{O}(\epsilon) = 10^{-4}$ - $\mathcal{O}(\epsilon) = 10^{-10}$, respectively

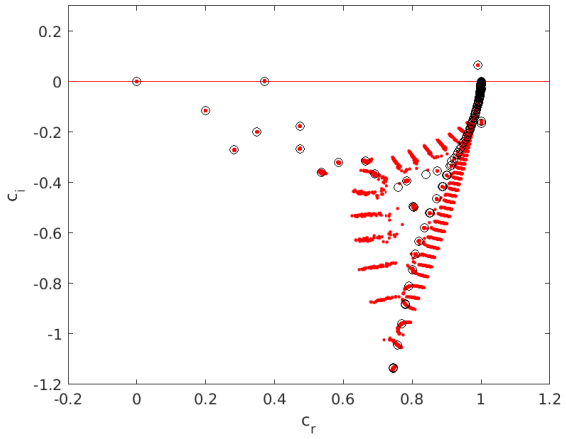

(a) $\mathcal{O}(\epsilon) = 10^{-4}$

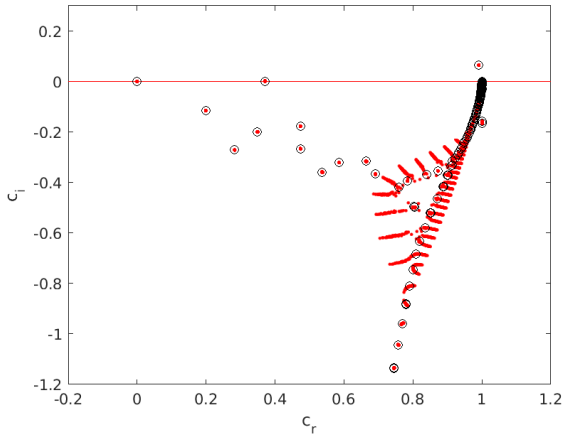

(b) $\mathcal{O}(\epsilon) = 10^{-5}$

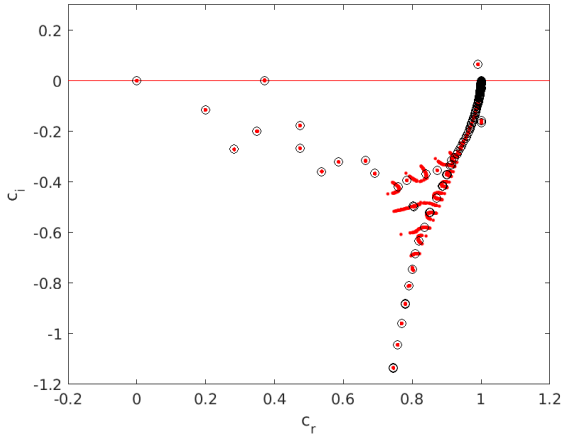

(c) $\mathcal{O}(\epsilon) = 10^{-6}$

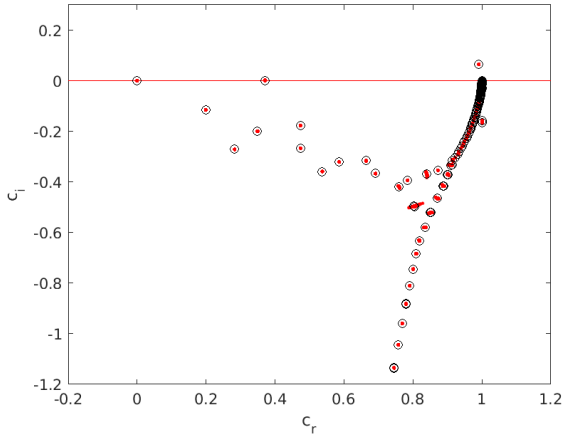

(d) $\mathcal{O}(\epsilon_{pert}) = 10^{-7}$

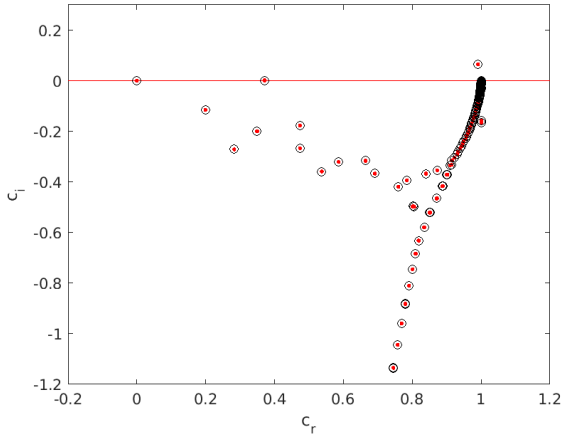

(e) $\mathcal{O}(\epsilon) = 10^{-8}$

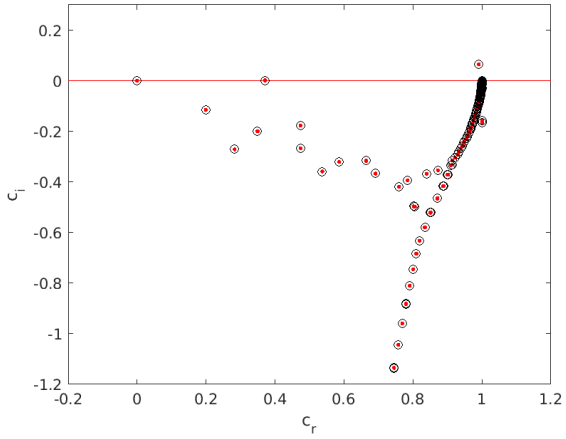

(f) $\mathcal{O}(\epsilon) = 10^{-10}$

Figure 6.6: Temporal eigenvalue spectra for the incompressible LST equations, with $M = 10^{-3}, Re = 580, \alpha = 0.2, NC = 150$. Perturbations from a normal distribution with a mean of 0 and a standard deviation of 1 are introduced in the wall region of the streamwise velocity base flow profile. The imposed perturbations are in the order of $\mathcal{O}(\epsilon) = 10^{-4}$ - $\mathcal{O}(\epsilon) = 10^{-10}$, respectively

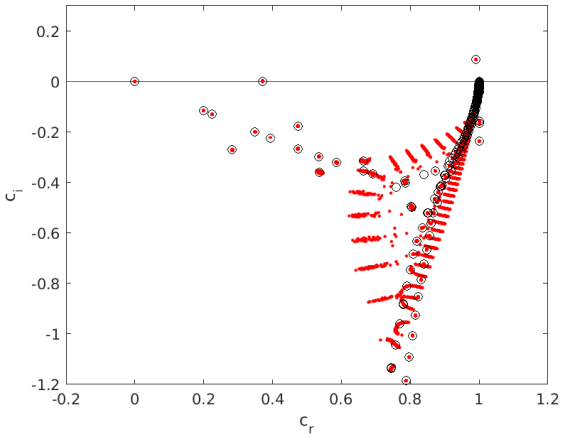

(a) $\mathcal{O}(\epsilon) = 10^{-4}$

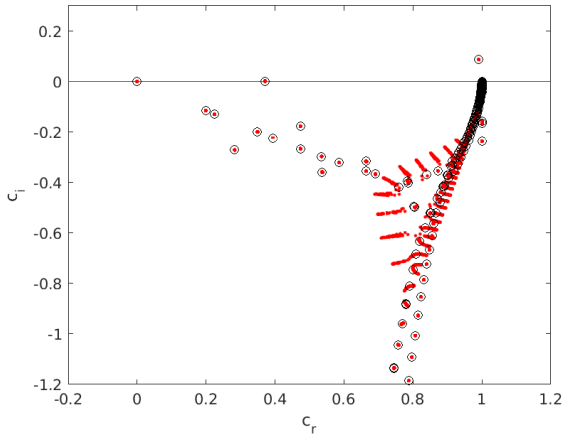

(b) $\mathcal{O}(\epsilon) = 10^{-5}$

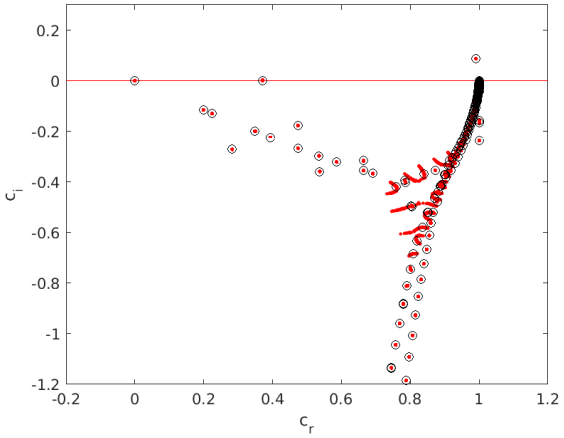

(c) $\mathcal{O}(\epsilon) = 10^{-6}$

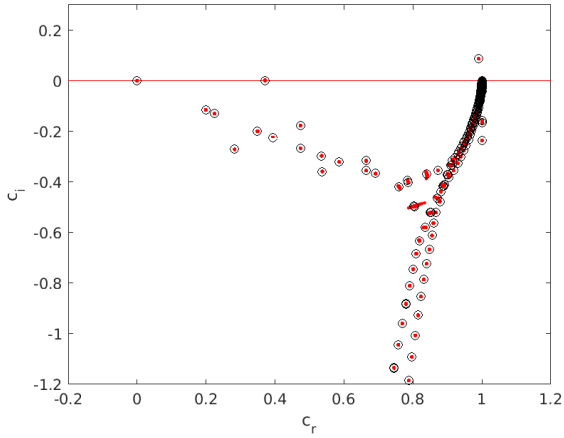

(d) $\mathcal{O}(\epsilon_{pert}) = 10^{-7}$

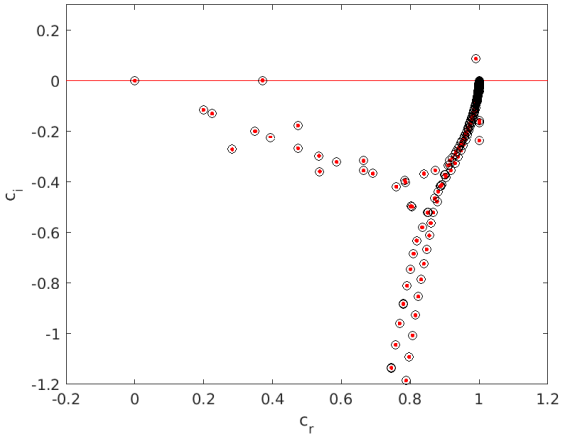

(e) $\mathcal{O}(\epsilon) = 10^{-8}$

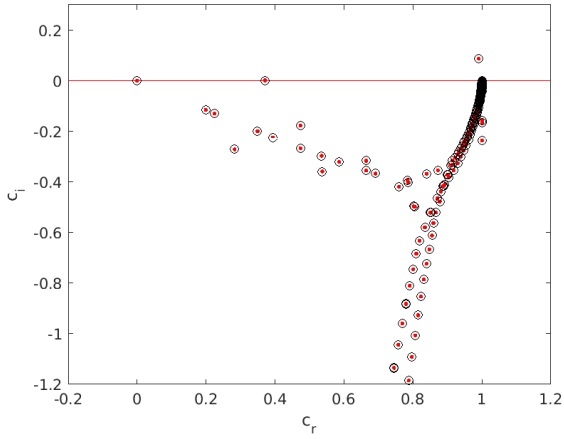

(f) $\mathcal{O}(\epsilon) = 10^{-10}$

Figure 6.7: Temporal eigenvalue spectra for the compressible LST equations, with $M = 10^{-3}, Re = 580, \alpha = 0.2, NC = 150$. Perturbations from a normal distribution with a mean of 0 and a standard deviation of 1 are introduced in the wall region of the streamwise velocity base flow profile. The imposed perturbations are in the order of $\mathcal{O}(\epsilon) = 10^{-4}$ - $\mathcal{O}(\epsilon) = 10^{-10}$, respectively

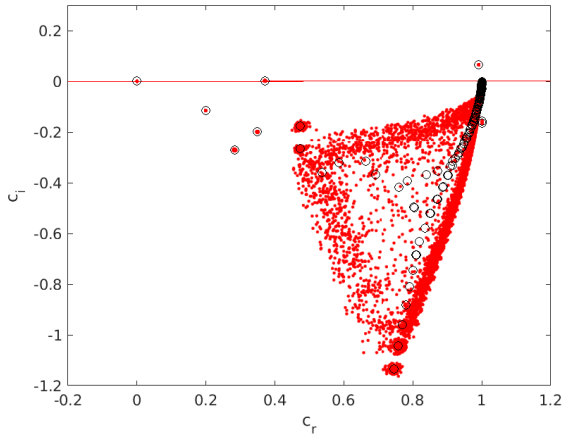

(a) $\mathcal{O}(\epsilon) = 10^{-4}$

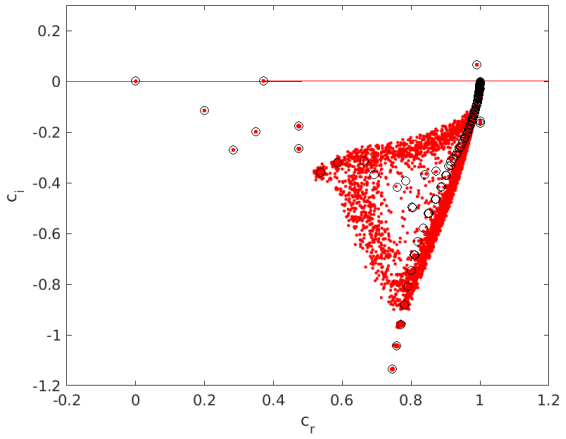

(b) $\mathcal{O}(\epsilon) = 10^{-5}$

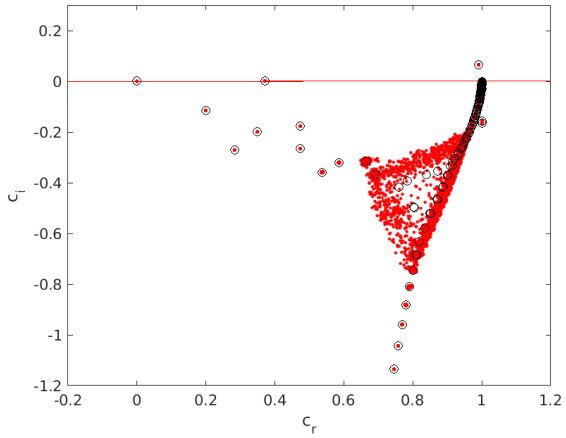

(c) $\mathcal{O}(\epsilon) = 10^{-6}$

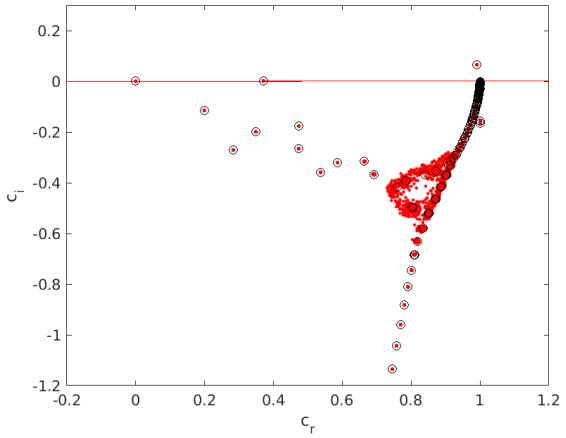

(d) $\mathcal{O}(\epsilon_{pert}) = 10^{-7}$

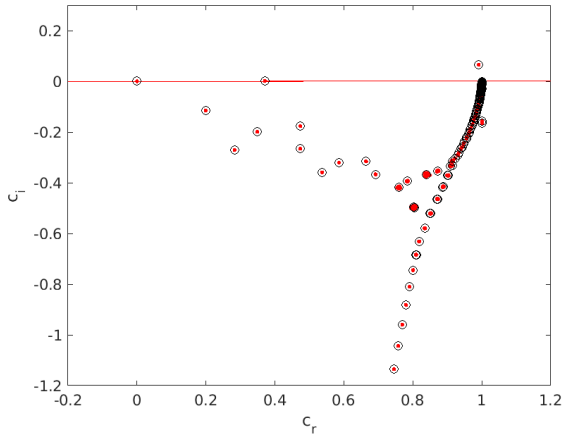

(e) $\mathcal{O}(\epsilon) = 10^{-8}$

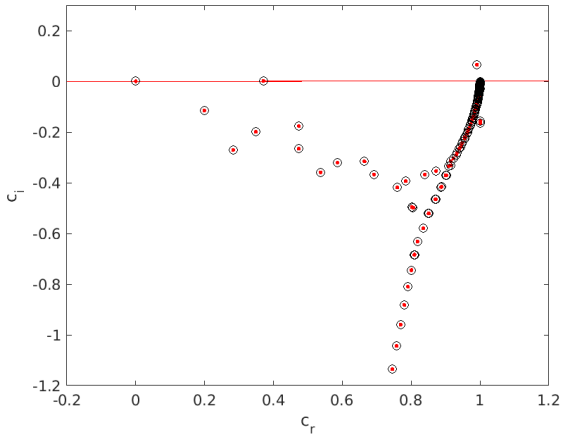

(f) $\mathcal{O}(\epsilon) = 10^{-10}$

Figure 6.8: Temporal eigenvalue spectra for the incompressible LST equations, with $M = 10^{-3}, Re = 580, \alpha = 0.8, NC = 150$. Perturbations from a normal distribution with a mean of 0 and a standard deviation of 1 are introduced in a middle region between δ_{25} and δ_{99} of the streamwise velocity base flow profile. The imposed perturbations are in the order of $\mathcal{O}(\epsilon) = 10^{-4}$ - $\mathcal{O}(\epsilon) = 10^{-10}$, respectively

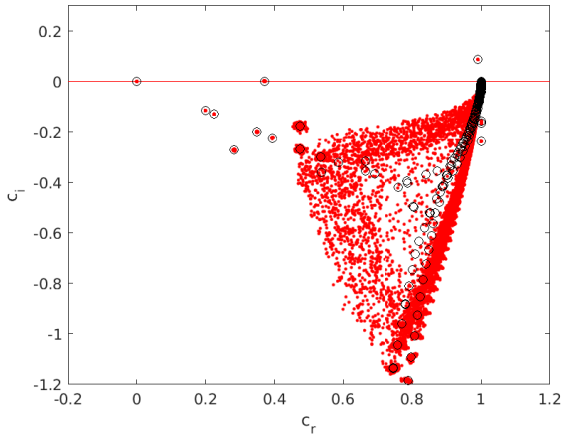

(a) $\mathcal{O}(\epsilon) = 10^{-4}$

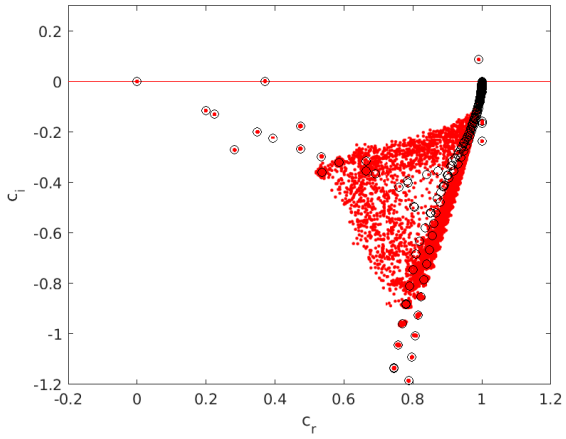

(b) $\mathcal{O}(\epsilon) = 10^{-5}$

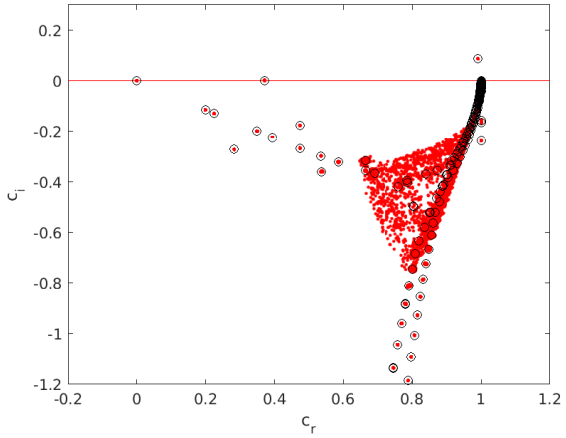

(c) $\mathcal{O}(\epsilon) = 10^{-6}$

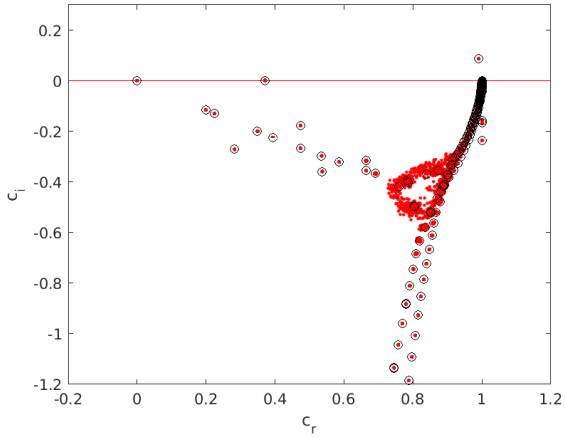

(d) $\mathcal{O}(\epsilon_{pert}) = 10^{-7}$

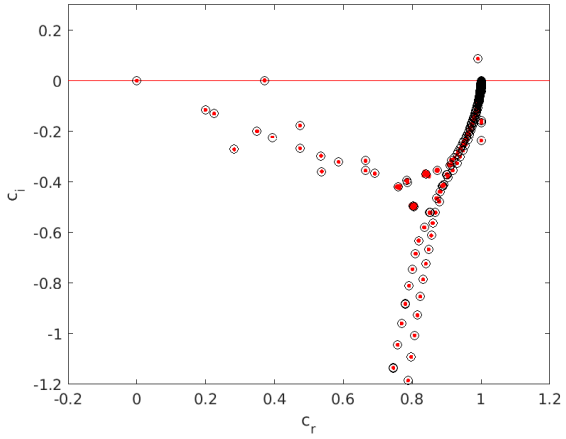

(e) $\mathcal{O}(\epsilon) = 10^{-8}$

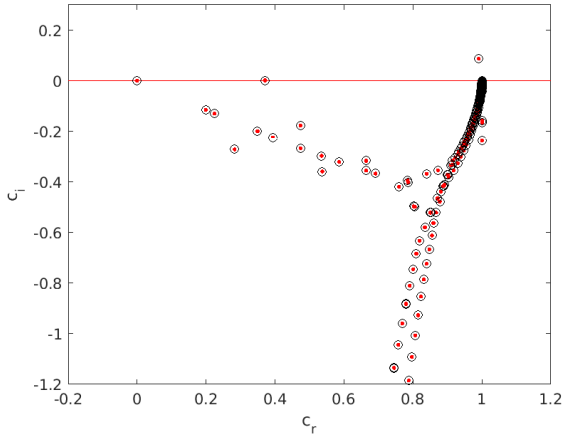

(f) $\mathcal{O}(\epsilon) = 10^{-10}$

Figure 6.9: Temporal eigenvalue spectra for the compressible LST equations, with $M = 10^{-3}, Re = 580, \alpha = 0.2, NC = 150$. Perturbations from a normal distribution with a mean of 0 and a standard deviation of 1 are introduced in a middle region of the streamwise velocity base flow profile. The imposed perturbations are in the order of $\mathcal{O}(\epsilon) = 10^{-4}$ - $\mathcal{O}(\epsilon) = 10^{-10}$, respectively

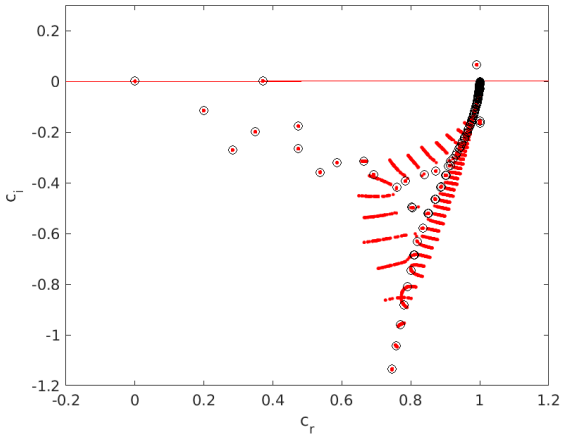

(a) $\mathcal{O}(\epsilon) = 10^{-4}$

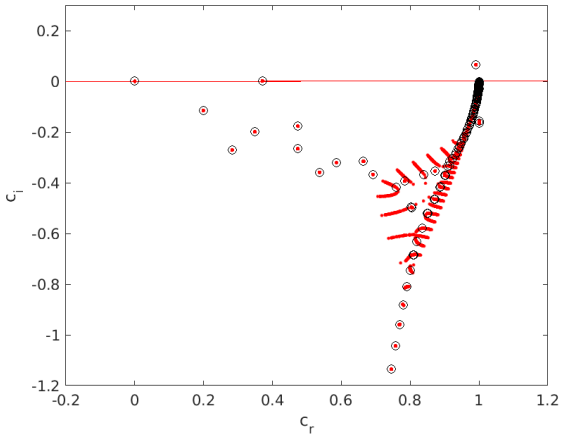

(b) $\mathcal{O}(\epsilon) = 10^{-5}$

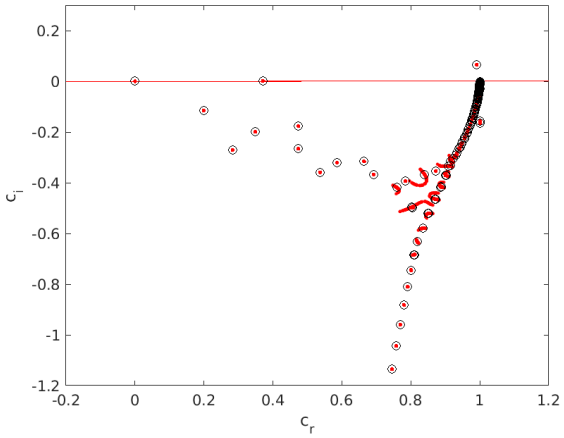

(c) $\mathcal{O}(\epsilon) = 10^{-6}$

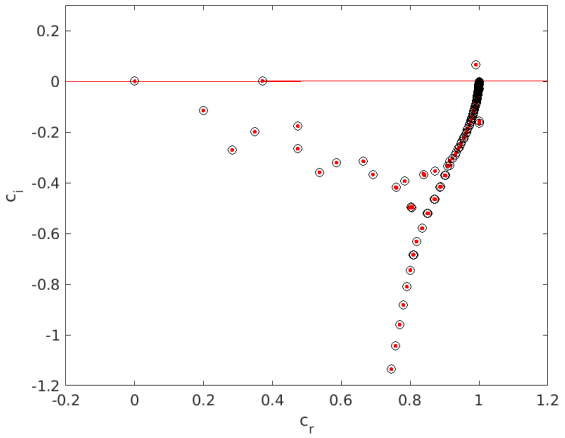

(d) $\mathcal{O}(\epsilon_{pert}) = 10^{-7}$

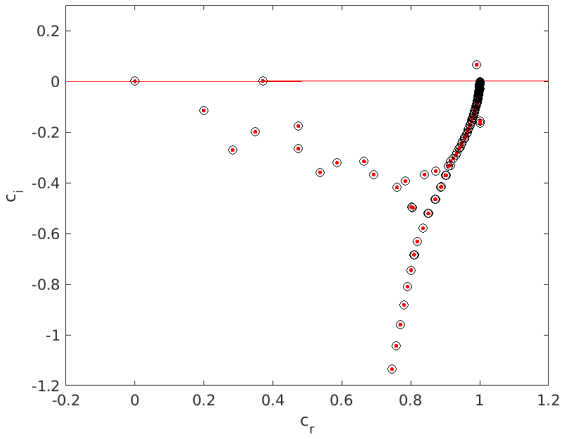

(e) $\mathcal{O}(\epsilon) = 10^{-8}$

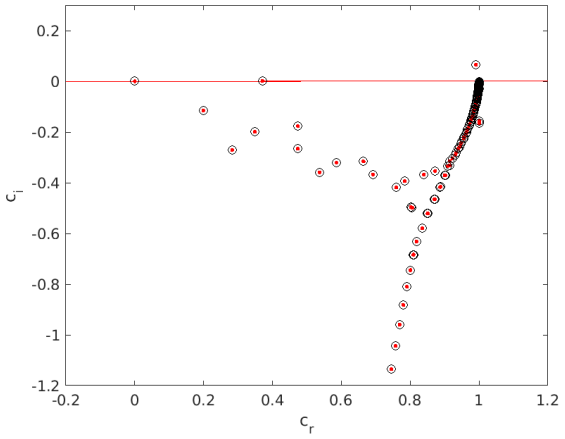

(f) $\mathcal{O}(\epsilon) = 10^{-10}$

Figure 6.10: Temporal eigenvalue spectra for the incompressible LST equations, with $M = 10^{-3}, Re = 580, \alpha = 0.8, NC = 150$. Perturbations from a normal distribution with a mean of 0 and a standard deviation of 1 are introduced in a top layer of the streamwise velocity base flow profile. The imposed perturbations are in the order of $\mathcal{O}(\epsilon) = 10^{-4}$ - $\mathcal{O}(\epsilon) = 10^{-10}$, respectively

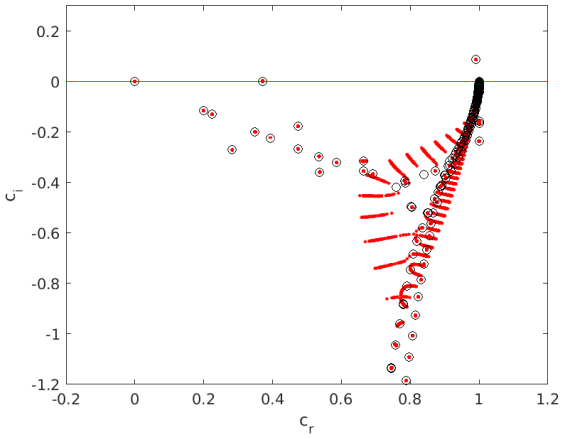

(a) $\mathcal{O}(\epsilon) = 10^{-4}$

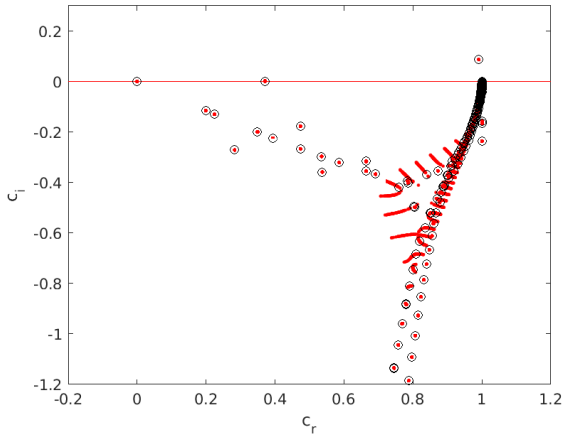

(b) $\mathcal{O}(\epsilon) = 10^{-5}$

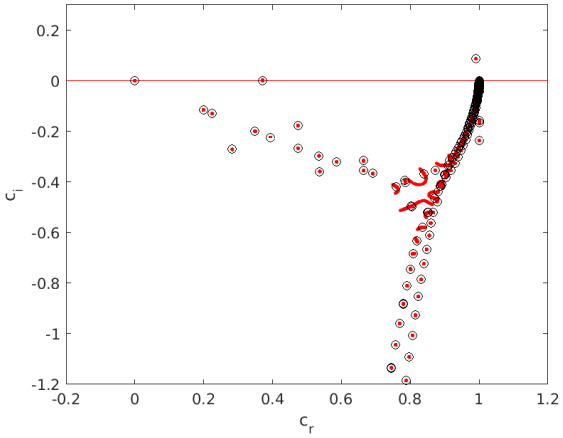

(c) $\mathcal{O}(\epsilon) = 10^{-6}$

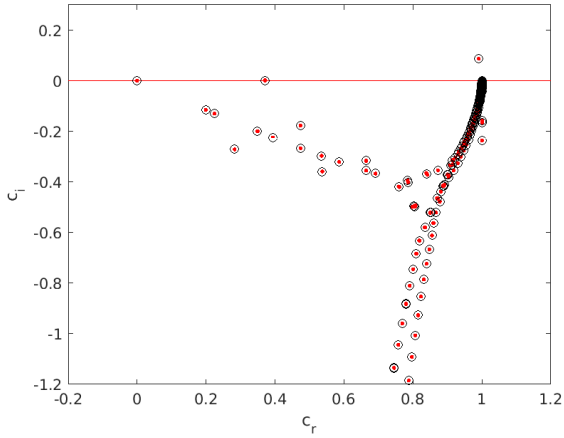

(d) $\mathcal{O}(\epsilon_{pert}) = 10^{-7}$

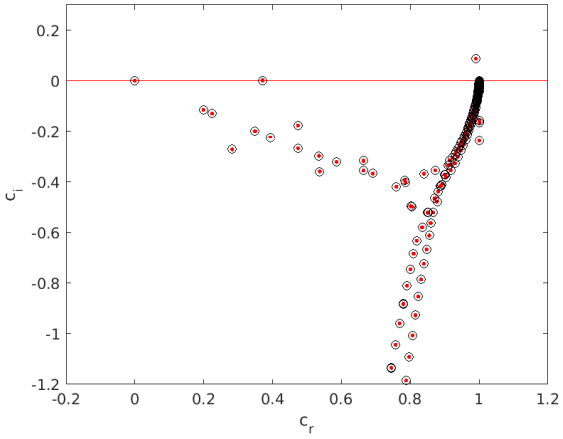

(e) $\mathcal{O}(\epsilon) = 10^{-8}$

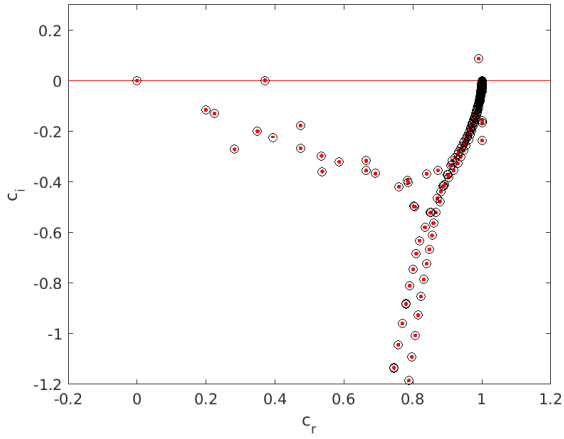

(f) $\mathcal{O}(\epsilon) = 10^{-10}$

Figure 6.11: Temporal eigenvalue spectra for the compressible LST equations, with $M = 10^{-3}, Re = 580, \alpha = 0.2, NC = 150$. Perturbations from a normal distribution with a mean of 0 and a standard deviation of 1 are introduced in a top layer of the streamwise velocity base flow profile. The imposed perturbations are in the order of $\mathcal{O}(\epsilon) = 10^{-4}$ - $\mathcal{O}(\epsilon) = 10^{-10}$, respectively

7

Conclusions and recommendations

Adjoint derivations and bi-orthogonality

Recall that the **first aim** of this thesis was to assess whether we can derive bi-orthogonality relations demonstrating that the adjoint LST eigenvectors are orthogonal to the direct eigenvectors, for both the compressible and incompressible LST equations; thereby resolving the non-orthogonality complication. It is to that end that we derived the adjoint operators for the incompressible and compressible LST equations using both the discrete and the continous approach in chapter 3. Subsequently, we derived, implemented and assessed bi-orthogonality relations using the adjoint eigenvectors resulting from the discrete and continous approaches in chapter 3.

It was found that theoretically relations can be derived for which a weight matrix ensures bi-orthogonal sets of direct and adjoint eigenvectors. Numerical implementation of these bi-orthogonality relations for both the incompressible and compressible LST yielded diagonal bi-orthogonality coefficient matrices for the discrete case. Results for the continous approach have shown that the coefficient matrices are diagonally dominant, but do contain substantial off-diagonal terms. As per the theoretical bi-orthogonality derivation, the complex conjugates of the adjoint eigenvalues were shown to match the direct eigenvalues in the physically interesting range, for both the incompressible and compressible LST spectra.

The discrete and continous adjoint eigenmodes were found to be *similar* in shape and location, but the modes did not coincide. A potential explanation for the discrepancy might be the use of the Chebyshev collocation nodes in the continous adjoint EVP. The adjoint EVP may require different stretching of the mesh. Alternatively, closing the continuous adjoint system using the 'adjoint wall-normal equation' as a compatiblity condition for the adjoint pressure amplitude might possibly adversely affect the continous adjoint eigenmodes.

An interesting observation was made when considering the spatial structure defining the overlap between direct eigenmodes and discrete adjoint eigenmodes. For both a wall mode, and a 'middle region' mode, the location of the maximum amplitude of the direct eigenmode was found to differ spatially from that of the maximum amplitude of the discrete adjoint eigenmode.

Eigenvalue spectrum sensitivity to specific perturbations in the base flow

The **second aim** of this study was to determine how the eigenvalue spectrum of the LST operator is affected by specific perturbations in the base flow profile. It is to that end that we first computed pseudospectra for the incompressible and compressible LST eqations for a perturbed generalised eigenvalue problem (GEP):

$$(A + E)\mathbf{q} = \omega(B + E)\mathbf{q} \quad \text{, with} \quad E \sim \mathcal{O}(\epsilon) \tag{7.1}$$

for a Falkner-Skan-Cooke boundary layer flow in Chapter 5.

Subsequently we computed eigenspectra for the incompressible and compressible LST eqations for a perturbed streamwise velocity base flow profile $u(y) + E(y)$, with $E \sim \mathcal{O}(\epsilon)$ in Chapter 6. The perturbations were imposed on the base flow velocity profile (1) in its entirety, (2) in the wall region (2) in a middle layer, and (3) on a top layer near the free-stream edge.

For the pseudospectra of the generalised eigenvalue problem, it was found that the disturbance of the eigenvalue spectrum resulting from the matrix perturbations would initiate from the intersection of the continous branch and the discrete set of modes. For increasing perturbation size, the disturbance of the spectrum was then seen to spread outward. Especially for larger perturbations the eigenvalues would describe a contour within which most of the 'pseudo-eigenvalues' were contained in a relatively noisy pattern. For higher spatial wavenumbers α the eigenvalue spectrum was found to be more robust to perturbations .

The eigenspectrum has been shown to not be uniformly affected by matrix perturbations. Some eigenvalues have a visible shift in the spectrum for perturbations as small as $\mathcal{O}(10^{-8})$, whereas other eigenvalues display very little movement even for perturbations of $\mathcal{O}(10^{-4})$, or $\mathcal{O}(10^{-5})$. Thus, for some modes the shift of the eigenvalues in the spectrum is far greater in orders of magnitude than the perturbations imposed. Notably the set of discrete wall modes, and the TS-mode, appeared to remain relatively close to their unperturbed position.

Another interesting observation made in the pseudospectra analysis was that the 'free-stream' modes for which $c_r \to 1$, and the discrete wall modes with relatively small c_r tend to move less for a certain perturbation than the modes for which c_r is mid-range. As these findings are in agreement with the sensitivity findings of Schmid [19] for Poiseuille and Couette flow, there appears to be a 'sensitivity pattern' for perturbed eigenspectra of shear force flows.

7

For the perturbed base flow problem it was found that perturbing the entire profile produced superimposed eigenspectra that are similar to the pseudospectra for the matrix perturbations. There were indiciations that for a certain sized perturbation (slightly) fewer eigenvalues would demonstrate visible movement for the perturbed base flow than for the matrix perturbations.

A comparison of the perturbations imposed on specific regions of the base flow indicated that perturbations in a middle region of the flow would most strongly affect the eigenvalues in that there was relatively more eigenvalue shift when compared with perturbations in just the wall region or the top layer. There were also indications that the spectrum is slightly more robust to perturbations in the top layer than in the wall region. Additionally, it was only perturbations in the middle region that lead to the previously seen contour within which most of the 'pseudo-eigenvalues' are contained in a relatively noisy pattern.

An interesting observation is that for both the wall region and top layer perturbations, the superposed modes at the intersection between the discrete modes and the continous modes, and the superposed modes along the continuous branch were found to be distributed along distinct lines.

Furthermore, and counterintuitively, the wall modes – which are dominant in the near-wall region – did not seem to be affected by a perturbation of the base flow in this specific region. This implies that errors in the input data, e.g. due to difficulties in measuring the near-wall region, may not necessarily lead to an eigenvalue shift of the TS-mode. Consequently, the long-term linear stability information from this might be eigenvalue rather robust.

General conclusions

We have demonstrated that the discrete adjoint LST eigenvectors are theoretically and numerically bi-orthogonal to the direct eigenvectors when using the derived weight matrix, for both the compressible and incompressible LST operators. This resolves the first complication of the non-normal LST operators: non-orthogonal eigenvectors. The demonstrated bi-orthogonality might allow for the investigation of (isolated) responses to different types of disturbances, which is especially of interest in boundary layer receptivity. Additionally, the demonstrated bi-orthogonality may aid in employing the eigenmodes as basis functions in a deterministic approach (e.g. GO-ROM), or as

control functions in a feedback loop (e.g. plasma actuation).

It was shown that the LST eigenvalue spectrum for the Falkner-Skan-Cooke boundary layer flow is not uniformly affected by matrix perturbations, or perturbations in the base flow. Some eigenvalues shift by orders of magnitude greater than the perturbations imposed, whereas other eigenvalues remain relatively close to their unperturbed position. Especially the discrete wall modes, notably the 'most unstable' TS-mode, were found to be relatively unaffected by perturbations (in the base-flow). On a practical note, this may mean that the TS mode can confidently be used as an indication of long-term linear stability for experimental base flows, in spite of measuring difficulties in certain regions of the base flow. An application could be to base flows obtained by means of Hot-Wire-Anemometry (HWA) for which it is notoriously difficult to accurately measure the near-wall region.

Recommendations

In this work we have considered only the incompressible Tollmien-Schlichting instability case, with a relatively low Reynolds number. It might be worthwile to investigate how the findings for the base flow perturbations extend to the compressible regime. Yet another potential avenue might be to consider the effect of a completely different type of perturbation on the base flow. For example, superimposing a mode-like disturbance, e.g. the TS mode, or an adjoint mode on the base flow to not only investigate the response, but also the sensitivity of the eigenspectrum.

Future work on the adjoint systems and bi-orthogonality relations could focus on the structural sensitivity. We found for both wall mode, and 'middle region' modes, that the location of the maximum amplitude of the direct eigenmode was different spatially from that of the maximum amplitude of the discrete adjoint eigenmode. As a result, the spatial structure defining the overlap between the discrete adjoint mode and the direct mode had its maximum amplitude in a region (slightly) different from that of the direct mode. This overlap provides information "*about the region in space where a feedback-forcing proportional to the local velocity has the largest impact on eigenvalue drift*" [19]. It would be very interesting to investigate structural sensitivity in the context of specific base flow perturbations in the LST framework. This would effectively link the two topics in this thesis. The paper by Luchini et al. [9] provides results in this regard for a flow past a circular cylinder, which may prove a useful starting point.

Bibliography

[1] D Arnal and G Casalis. Laminar-turbulent transition prediction in three-dimensional flows. *Progress in Aerospace Sciences*, 36(2):173–191, 2000.

[2] Mark Embree. Pseudospectra and the behavior of dynamical systems. Lecture Slides, 2011.

[3] Valérie Fraysse, Michel Gueury, Frank Nicoud, and Vincent Toumazou. Spectral portraits for matrix pencils, 1996.

[4] Koen J. Groot. Derivation of and simulations with biglobal stability equations. Master's thesis, Faculty of Aerospace Engineering, Delft University of Technology, 2013.

[5] Koen J. Groot, Fernando Miro Miro, Ethan S. Beyak, Alexander J. Moyes, Fabio Pinna, and Helen L. Reed. Dekaf: Spectral multi-regime basic-state solver for boundary-layer stability. In *2018 Fluid Dynamics Conference [AIAA 2018- 3380]*. AIAA, 2018.

[6] M Yousuff Hussaini, David A Kopriva, and Anthony T Patera. Spectral collocation methods. *Applied Numerical Mathematics*, 5(3):177–208, 1989.

[7] Edward Kerschen. Boundary layer receptivity. In *12th Aeroacoustic Conference*, page 1109, 1989.

[8] Paolo Luchini and Alessandro Bottaro. Adjoint equations in stability analysis. *Annual Review of fluid mechanics*, 46, 2014.

[9] Paolo Luchini, Flavio Giannetti, and Jan Pralits. Structural sensitivity of linear and nonlinear global modes. In *5th AIAA Theoretical Fluid Mechanics Conference*, page 4227, 2008.

[10] Anders Lundbladh and Arne V Johansson. Direct simulation of turbulent spots in plane couette flow. *Journal of Fluid Mechanics*, 229:499–516, 1991.

[11] Mujeeb R Malik. Numerical methods for hypersonic boundary layer stability. *Journal of Computational Physics*, 86(2):376–413, 1990.

[12] M.V. Morkovin. On the many faces of transition. in: Viscous drag reduction. Springer, Boston, MA, 1969.

[13] M.V. Morkovin. Bypass transition to turbulence and research desiderata. NASA, Conference Publication 2386, 1985.

[14] Fabio Pinna. *Numerical study of stability of flows from low to high Mach number*. PhD thesis, Von Karman Institute for Fluid Dynamics & Universitá "La Sapienza" di Roma, 2012.

[15] Satish C. Reddy, Peter J. Schmid, and Dan S. Henningson. Pseudospectra of the orr-sommerfeld operator. *SIAM Journal on Applied Mathematics*, 53(1):15–47, 1993.

[16] Eli Reshotko. Boundary-layer stability and transition. *Annual Review of Fluid Mechanics*, 8(1):311–349, 1976.

[17] Valerii Aleksandrovich Romanov. Stability of plane-parallel couette flow. *Functional analysis and its applications*, 7(2):137–146, 1973.

[18] William S Saric, Edward B White, and Helen L Reed. Boundary-layer receptivity to freestream disturbances and its role in transition. *AIAA paper*, (99-3788), 1999.

[19] Peter J Schmid and Luca Brandt. Analysis of fluid systems: Stability, receptivity, sensitivity - lecture notes from the flow-nordita summer school on advanced instability methods for complex flows. *Applied Mechanics Reviews*, 66(2):024803, 2014.

[20] Peter J Schmid and Dan S Henningson. *Stability and transition in shear flows*, volume 142. Springer Science & Business Media, 2001.

[21] P.J. Schmid, D.S. Henningson, M.R. Khorrami, and Mujeeb R. Malik. A study of eigenvalue sensitivity for hydrodynamic stability operators. *Theoretical and Computational Fluid Dynamics*, 4(5):227–240, 1993.

[22] A.M.O. Smith and N. Gamberoni. Transition, pressure gradient and stability theory. Douglas Aircraft Co. Report ES 26388, El Segunelo, California, 1956.

[23] Vassilios Theofilis. Advances in global linear instability analysis of nonparallel and three-dimensional flows. *Progress in aerospace sciences*, 39(4):249–315, 2003.

[24] Nils Tillmark and P Henrik Alfredsson. An experimental study of transition in plane couette flow. In *Advances in Turbulence 3*, pages 235–242. Springer, 1991.

[25] L. N. Trefethen. Computation of pseudospectra. pages 247–295. Cambridge University Press, 1999.

[26] Lloyd N Trefethen, Anne E Trefethen, Satish C Reddy, and Tobin A Driscoll. Hydrodynamic stability without eigenvalues. *Science*, 261(5121):578–584, 1993.

[27] Lloyd Nicholas Trefethen and Mark Embree. *Spectra and pseudospectra: the behavior of nonnormal matrices and operators*. Princeton University Press, 2005.

[28] J.L. van Ingen. A suggested semi-empirical method for the calculation of the boundary layer transition region. Report VTH-74, Delft University of Technology, The Netherlands, 1956.

[29] Thomas G. Wright. Eigtool, 2002.

A

Derivation of the compressible adjoint LST operator

Compressible LST Equations

This appendix contains the compressible Linear Stability Theory (LST) equations in Cartesian, cylindrical, spherical and a specific curvilinear coordinate system.

Noting that $g_{ij} = \sum_{k=1}^{3} \frac{\partial y^k}{\partial x^i} \frac{\partial y^k}{\partial x^j}$ where x^i denote the (possibly) curvilinear coordinates and y^i are the Cartesian coordinates, the following conventions apply in the case of this system:

Streamwise:	$x^1 = x$	spectral (α)	Metric tensor:	$g = \begin{bmatrix} 1 & 0 & 0 \\ 0 & 1 & 0 \\ 0 & 0 & 1 \end{bmatrix}$
Wall-normal:	$x^2 = y$	differential		
Spanwise:	$x^3 = z$	spectral (β)		

Note that in this case global analysis is performed in the y-direction. This yields the following set of equations:

Continuity equation

$$-\frac{i\beta\tilde{T}\overline{P}\overline{W}}{\overline{T}} + i\beta\tilde{p}\overline{W} - \frac{i\alpha\tilde{T}\overline{P}\overline{U}}{\overline{T}} + i\alpha\tilde{p}\overline{U} - \frac{\tilde{v}\overline{P}\overline{T}_y}{\overline{T}} + \frac{i\omega\tilde{T}\overline{P}}{\overline{T}} - i\omega\tilde{p} + \tilde{v}\overline{P}_y + i\beta\tilde{w}\overline{P} + \tilde{v}_y\overline{P} + i\alpha\tilde{u}\overline{P} = 0 \tag{B.1}$$

x-Momentum equation

$$\frac{i\beta\gamma\tilde{u}M^2\overline{P}\overline{W}}{\overline{T}} + \frac{\gamma\tilde{u}M^2\overline{P}\overline{U}_y}{\overline{T}} + \frac{i\alpha\gamma\tilde{u}M^2\overline{P}\overline{U}}{\overline{T}} - \frac{i\gamma\omega\tilde{u}M^2\overline{P}}{\overline{T}} - \frac{\tilde{T}\overline{\mu}_{\overline{T}}\overline{U}_{yy}}{Re} + \frac{\tilde{T}\overline{\mu}_{\overline{T}\overline{T}}\overline{T}_y\overline{U}_y}{Re} + \frac{\tilde{T}_y\overline{\mu}_{\overline{T}}\overline{U}_y}{Re} + \frac{i\alpha\tilde{v}\overline{\mu}_{\overline{T}}\overline{T}_y}{Re} + \frac{\tilde{u}_y\overline{\mu}_{\overline{T}}\overline{T}_y}{Re} - i\alpha\tilde{p} - \frac{\alpha\beta\tilde{w}\overline{\mu}}{Re} + \frac{i\alpha\tilde{v}_y\overline{\mu}}{Re} + \frac{\tilde{u}_{yy}\overline{\mu}}{Re} - \frac{\beta^2\tilde{u}\overline{\mu}}{Re} - \frac{2\alpha^2\tilde{u}\overline{\mu}}{Re} - \frac{\alpha\beta\tilde{w}\overline{\lambda}}{Re} + \frac{i\alpha\tilde{v}_y\overline{\lambda}}{Re} - \frac{\alpha^2\tilde{u}\overline{\lambda}}{Re} \tag{B.2}$$

y-Momentum equation

$$\frac{i\beta\gamma\tilde{v}M^2\overline{P}\,\overline{W}}{\overline{T}}+\frac{i\alpha\gamma\tilde{v}M^2\overline{P}\,\overline{U}}{\overline{T}}-\frac{i\gamma\omega\tilde{v}M^2\overline{P}}{\overline{T}}-\frac{i\beta\tilde{T}\overline{\mu}_{\overline{T}}\overline{W}_y}{Re}+\frac{i\alpha\tilde{T}\overline{\mu}_{\overline{T}}\overline{U}_y}{Re}$$
$$+\frac{2\tilde{v}_y\overline{\mu}_{\overline{T}}\overline{T}_y}{Re}+\frac{i\beta\tilde{w}\overline{\lambda}_{\overline{T}}\overline{T}_y}{Re}+\frac{\tilde{v}_y\overline{\lambda}_{\overline{T}}\overline{T}_y}{Re}+\frac{i\alpha\tilde{u}\overline{\lambda}_{\overline{T}}\overline{T}_y}{Re}-\tilde{p}_y+\frac{i\beta\tilde{w}_y\overline{\mu}}{Re}+\frac{2\tilde{v}_{yy}\overline{\mu}}{Re}$$
$$-\frac{\beta^2\tilde{v}\overline{\mu}}{Re}-\frac{\alpha^2\tilde{v}\overline{\mu}}{Re}+\frac{i\alpha\tilde{u}_y\overline{\mu}}{Re}+\frac{i\beta\tilde{w}_y\overline{\lambda}}{Re}+\frac{\tilde{v}_{yy}\overline{\lambda}}{Re}+\frac{i\alpha\tilde{u}_y\overline{\lambda}}{Re} \tag{B.3}$$

z-Momentum equation

$$\frac{\gamma\tilde{v}M^2\overline{P}\,\overline{W}_y}{\overline{T}}+\frac{i\beta\gamma\tilde{w}M^2\overline{P}\,\overline{W}}{\overline{T}}+\frac{i\alpha\gamma\tilde{u}M^2\overline{P}\,\overline{U}}{\overline{T}}-\frac{i\gamma\omega\tilde{w}M^2\overline{P}}{\overline{T}}-\frac{\tilde{T}\overline{\mu}_{\overline{T}}\overline{W}_{yy}}{Re}$$
$$+\frac{\tilde{T}\overline{\mu}_{\overline{T}\overline{T}}\overline{T}_y\overline{W}_y}{Re}+\frac{\tilde{T}_y\overline{\mu}_{\overline{T}}\overline{W}_y}{Re}+\frac{\tilde{w}_y\overline{\mu}_{\overline{T}}\overline{T}_y}{Re}+\frac{i\beta\tilde{v}\overline{\mu}_{\overline{T}}\overline{T}_y}{Re}-i\beta\tilde{p}+\frac{\tilde{w}_{yy}\overline{\mu}}{Re}-\frac{2\beta^2\tilde{w}\overline{\mu}}{Re}$$
$$-\frac{\alpha^2\tilde{w}\overline{\mu}}{Re}+\frac{i\beta\tilde{v}_y\overline{\mu}}{Re}-\frac{\alpha\beta\tilde{u}\overline{\mu}}{Re}-\frac{\beta^2\tilde{w}\overline{\lambda}}{Re}+\frac{i\beta\tilde{v}_y\overline{\lambda}}{Re}-\frac{\alpha\beta\tilde{u}\overline{\lambda}}{Re} \tag{B.4}$$

Energy equation

$$\frac{i\beta\gamma\tilde{T}M^2\overline{P}\,\overline{W}}{\overline{T}}+\frac{i\alpha\gamma\tilde{T}M^2\overline{P}\,\overline{U}}{\overline{T}}+\frac{\gamma\tilde{v}M^2\overline{P}\,\overline{T}_y}{\overline{T}}-\frac{i\gamma\omega\tilde{T}M^2\overline{P}}{\overline{T}}$$
$$-\frac{(\gamma-1)\tilde{T}M^2\overline{\mu}_{\overline{T}}\left(\overline{W}_y\right)^2}{Re}+\frac{2(\gamma-1)\tilde{w}_yM^2\overline{\mu}\,\overline{W}_y}{Re}+\frac{2i\beta(\gamma-1)\tilde{v}M^2\overline{\mu}\,\overline{W}_y}{Re}$$
$$+i\beta(\gamma-1)M^2\tilde{p}\overline{W}+\frac{(\gamma-1)\tilde{T}M^2\overline{\mu}_{\overline{T}}\left(\overline{U}_y\right)^2}{Re}+\frac{2i\alpha(\gamma-1)\tilde{v}M^2\overline{\mu}\overline{U}_y}{Re}$$
$$+\frac{2(\gamma-1)\tilde{u}_yM^2\overline{\mu}\overline{U}_y}{Re}+i\alpha(\gamma-1)M^2\tilde{p}\overline{U}+\frac{\tilde{T}\overline{k}_{\overline{T}}\overline{T}_{yy}}{Pr\,Re}+\frac{\tilde{T}\overline{k}_{\overline{T}\overline{T}}\left(\overline{T}_y\right)^2}{Pr\,Re}$$
$$+\frac{2\tilde{T}_y\overline{k}_{\overline{T}}\overline{T}_y}{Pr\,Re}+\frac{\tilde{T}_{yy}\overline{k}}{Pr\,Re}-\frac{\beta^2\tilde{T}\overline{k}}{Pr\,Re}-\frac{\alpha^2\tilde{T}\overline{k}}{Pr\,Re}$$
$$-i(\gamma-1)\omega M^2\tilde{p}+(\gamma-1)\tilde{v}M^2\overline{P}_y \tag{B.5}$$

Compressible LST (streamwise: x, spectral (α); wall-normal: y, differential; spanwise: z, spectral (β))

x-MOMENTUM

$$\tilde{u}: \left\{ \underbrace{\frac{i\beta\gamma\Pi^2\bar{P}\bar{W}}{\bar{T}}}_{\text{I}} + \underbrace{\frac{i\alpha\gamma\Pi^2\bar{P}\bar{u}}{\bar{T}}}_{\text{II}} - \underbrace{\frac{\bar{\mu}_{\bar{T}}\bar{T}_y}{Re}}_{\text{III}}D - \underbrace{\frac{\bar{\mu}}{Re}}_{\text{IV}}D^2 + \underbrace{\frac{\beta^2\bar{\mu}}{Re}}_{\text{V}} + \underbrace{\frac{2\alpha^2\bar{\mu}}{Re}}_{\text{VI}} + \underbrace{\frac{\alpha^2\bar{\lambda}}{Re}}_{\text{VII}} = \underline{\underline{\omega}}\underbrace{\frac{i\gamma\Pi^2\bar{P}}{\bar{T}}}_{\text{VIII}} \right\}$$

$$\tilde{v}: \left\{ \underbrace{\frac{\gamma\Pi^2\bar{P}\bar{u}_y}{\bar{T}}}_{\text{I}} - \underbrace{\frac{i\alpha\bar{\mu}_{\bar{T}}\bar{T}_y}{Re}}_{\text{II}} - \underbrace{\frac{i\alpha\bar{\mu}}{Re}}_{\text{III}}D - \underbrace{\frac{i\alpha\bar{\lambda}}{Re}}_{\text{IV}}D \right\}$$

$$\tilde{p}: \left\{ \underbrace{i\alpha}_{\text{I}} \right\}$$

$$\tilde{w}: \left\{ \underbrace{\frac{\alpha\beta\bar{\mu}}{Re}}_{\text{I}} + \underbrace{\frac{\alpha\beta\bar{\lambda}}{Re}}_{\text{II}} \right\}$$

$$\tilde{T}: \left\{ \underbrace{-\frac{\bar{\mu}_{\bar{T}}\bar{u}_{yy}}{Re}}_{\text{I}} - \underbrace{\frac{\bar{\mu}_{\bar{T}\bar{T}}\bar{T}_y\bar{u}_y}{Re}}_{\text{II}} - \underbrace{\frac{\bar{\mu}_{\bar{T}}\bar{u}_y}{Re}}_{\text{III}}D \right\}$$

y-MOMENTUM

$$\tilde{u}: \left\{ \underbrace{-\frac{i\alpha\bar{\lambda}_{\bar{T}}\bar{T}_y}{Re}}_{\text{I}} - \underbrace{\frac{i\alpha\bar{\mu}}{Re}}_{\text{II}}D - \underbrace{\frac{i\alpha\bar{\lambda}}{Re}}_{\text{III}}D \right\}$$

$$\tilde{v}: \left\{ \underbrace{\frac{i\beta\gamma\Pi^2\bar{P}\bar{W}}{\bar{T}}}_{\text{I}} + \underbrace{\frac{i\alpha\gamma\Pi^2\bar{P}\bar{u}}{\bar{T}}}_{\text{II}} - \underbrace{\frac{2\bar{\mu}_{\bar{T}}\bar{T}_y}{Re}}_{\text{III}}D - \underbrace{\frac{\bar{\lambda}_{\bar{T}}\bar{T}_y}{Re}}_{\text{IV}}D - \underbrace{\frac{2\bar{\mu}}{Re}}_{\text{VI}}D^2 + \underbrace{\frac{\beta^2\bar{\mu}}{Re}}_{\text{VI}} + \underbrace{\frac{\alpha^2\bar{\mu}}{Re}}_{\text{VII}} - \underbrace{\frac{\bar{\lambda}}{Re}}_{\text{VIII}}D^2 = \underline{\underline{\omega}}\underbrace{\frac{i\gamma\Pi^2\bar{P}}{\bar{T}}}_{\text{IX}} \right\}$$

$$\tilde{p}: \left\{ \underbrace{D}_{\text{I}} \right\}$$

$$\tilde{w}: \left\{ \underbrace{-\frac{i\beta\bar{\lambda}_{\bar{T}}\bar{T}_y}{Re}}_{\text{I}} - \underbrace{\frac{i\beta\bar{\mu}}{Re}}_{\text{II}}D - \underbrace{\frac{i\beta\bar{\lambda}}{Re}}_{\text{III}}D \right\}$$

$$\tilde{T}: \left\{ \underbrace{-\frac{i\beta\bar{\mu}_{\bar{T}}\bar{w}_y}{Re}}_{\text{I}} - \underbrace{\frac{i\alpha\bar{\mu}_{\bar{T}}\bar{u}_y}{Re}}_{\text{II}} \right\}$$

z-momentum

$$\hat{u}: \quad \left\{ \frac{\alpha\beta\bar{\mu}}{Re}^{I} + \frac{\alpha\beta\bar{\lambda}}{Re}^{II} \right\}$$

$$\hat{v}: \quad \left\{ \frac{\gamma\Pi^2\bar{P}\bar{W}_y}{\bar{T}}^{I} - \frac{i\beta\bar{\mu}_{\bar{T}}\bar{T}_y}{Re}^{II} - \frac{i\beta\bar{\mu}}{Re}D^{III} - \frac{i\beta\bar{\lambda}}{Re}D^{IV} \right\}$$

$$\hat{p}: \quad \left\{ i\beta^{I} \right\}$$

$$\hat{w}: \quad \left\{ \frac{i\beta\gamma\Pi^2\bar{P}\bar{W}}{\bar{T}}^{I} + \frac{i\alpha\gamma\Pi^2\bar{P}\bar{u}}{\bar{T}}^{II} - \frac{\bar{\mu}_{\bar{T}}\bar{T}_y}{Re}D^{III} - \frac{\bar{\mu}}{Re}D^{2\,IV} + \frac{2\beta^2\bar{\mu}}{Re}^{V} + \frac{\alpha^2\bar{\mu}}{Re}^{VI} + \frac{\beta^2\bar{\lambda}}{Re}^{VII} = \underline{\omega}\,\frac{i\gamma\Pi^2\bar{P}}{\bar{T}}^{VIII} \right\}$$

$$\hat{T}: \quad \left\{ -\frac{\bar{\mu}_{\bar{T}}\bar{W}_{yy}}{Re}^{I} - \frac{\bar{\mu}_{\bar{T}\bar{T}}\bar{T}_y\bar{W}_y}{Re}^{II} - \frac{\bar{\mu}_{\bar{T}}\bar{W}_y}{Re}D^{III} \right\}$$

Energy

$$\hat{u}: \quad \left\{ -\frac{2(\gamma-1)\Pi^2\bar{\mu}\bar{u}_y}{Re}D^{I} \right\}$$

$$\hat{v}: \quad \left\{ \frac{\gamma\Pi^2\bar{P}\bar{T}_y}{\bar{T}}^{I} - \frac{2i\beta(\gamma-1)\Pi^2\bar{\mu}\bar{W}_y}{Re}^{II} - \frac{2i\alpha(\gamma-1)\Pi^2\bar{\mu}\bar{u}_y}{Re}^{III} - (\gamma-1)\Pi^2\bar{P}_y^{IV} \right\}$$

$$\hat{p}: \quad \left\{ -i\beta(\gamma-1)\Pi^2\bar{W}^{I} - i\alpha(\gamma-1)\Pi^2\bar{u}^{II} = -\underline{\omega}\,i(\gamma-1)\Pi^{2\,III} \right\}$$

$$\hat{w}: \quad \left\{ -\frac{2(\gamma-1)\Pi^2\bar{\mu}\bar{W}_y}{Re}D^{I} \right\}$$

$$\hat{T}: \quad \left\{ \frac{i\beta\gamma\Pi^2\bar{P}\bar{W}}{\bar{T}}^{I} + \frac{i\alpha\gamma\Pi^2\bar{P}\bar{u}}{\bar{T}}^{II} - \frac{(\gamma-1)\Pi^2\bar{\mu}_{\bar{T}}(\bar{W}_y)^{2\,III}}{Re} - \frac{(\gamma-1)\Pi^2\bar{\mu}_{\bar{T}}(\bar{u}_y)^{2\,IV}}{Re} - \frac{\bar{k}_{\bar{T}}\bar{T}_{yy}}{Pr\,Re}^{V} - \frac{\bar{k}_{\bar{T}\bar{T}}(\bar{T}_y)^{2\,VI}}{Pr\,Re} - \frac{2\bar{k}_{\bar{T}}\bar{T}_y}{Pr\,Re}D^{VII} - \frac{\bar{k}}{Pr\,Re}D^{2\,VIII} + \frac{\beta^2\bar{k}}{Pr\,Re}^{IX} + \frac{\alpha^2\bar{k}}{Pr\,Re}^{X} = \underline{\omega}\,\frac{i\gamma\Pi^2\bar{P}}{\bar{T}}^{XI} \right\}$$

CONTINUITY

$$\tilde{u}: \quad \left\{ \underline{i\alpha}\,\overline{\tilde{p}}^{\,I} \right\}$$

$$\tilde{v}: \quad \left\{ -\frac{\overline{\tilde{p}}\,\overline{\tilde{T}_y}^{\,I}}{\overline{\overline{T}}} + \overline{\tilde{p}_y}^{\,II} + \overline{\tilde{p}}\,\overline{D}^{\,III} \right\}$$

$$\tilde{p}: \quad \left\{ \underline{i\beta}\,\overline{\tilde{w}}^{\,I} + \underline{i\alpha}\,\overline{\tilde{u}}^{\,II} = \underline{\underline{\omega}}\,\underline{i}^{\,III} \right\}$$

$$\tilde{w}: \quad \left\{ \underline{i\beta}\,\overline{\tilde{p}}^{\,I} \right\}$$

$$\tilde{T}: \quad \left\{ -\frac{\underline{i\beta}\,\overline{\tilde{p}}\,\overline{\tilde{w}}^{\,I}}{\overline{\overline{T}}} - \frac{\underline{i\alpha}\,\overline{\tilde{p}}\,\overline{\tilde{u}}^{\,II}}{\overline{\overline{T}}} = -\underline{\underline{\omega}}\,\frac{\underline{i}\,\overline{\tilde{p}}^{\,III}}{\overline{\overline{T}}} \right\}$$

Inner product $(\tilde{q}^+, \mathcal{C}\tilde{q})$:

$$\left[(\tilde{u}^+)^*\ (\tilde{v}^+)^*\ (\tilde{p}^+)^*\ (\tilde{T}^+)^*\ (\tilde{w}^+)^*\right] \underbrace{\begin{bmatrix} [x\text{-mom}] \\ [y\text{-mom}] \\ [\text{CONTIN}] \\ [\text{ENERGY}] \\ [z\text{-mom}] \end{bmatrix}}_{(A-\omega B)=C} \begin{bmatrix} \tilde{u} \\ \tilde{v} \\ \tilde{p} \\ \tilde{T} \\ \tilde{w} \end{bmatrix} = 0$$

$(A-\omega B) = C \rightarrow$ (same system as in VESTA)

$$A^H (\tilde{q}^+)^* = \begin{bmatrix} A_{11} & A_{12} & A_{13} & A_{14} & A_{15} \\ A_{21} & A_{22} & A_{23} & A_{24} & A_{25} \\ A_{31} & A_{32} & A_{33} & A_{34} & A_{35} \\ A_{41} & A_{42} & A_{43} & A_{44} & A_{45} \\ A_{51} & A_{52} & A_{53} & A_{54} & A_{55} \end{bmatrix} \begin{bmatrix} (\tilde{u}^+)^* \\ (\tilde{v}^+)^* \\ (\tilde{p}^+)^* \\ (\tilde{T}^+)^* \\ (\tilde{w}^+)^* \end{bmatrix}$$

(similarly for $B^H(\tilde{q}^+)^*$)

LASER VISION
Tel.: +31 (0)529-428000
www.laservision.nl

Compressible Primitive Variable Formulation - Adjoint system

Derivation by means of the complex conjugate transpose of operator C,
where $C = (A - \omega B)$ ↳ from Gen. EVP $A\square = \omega B\square$

⟹ STEP 1 : Inner product (projection) of $(\tilde{q}^+, C\tilde{q}) = (\tilde{q}^+)^H C\tilde{q}$

⟹ STEP 2 : Substitution of complex conjugates into $C^H \rightarrow C^H$
(NOTE : in derivation below matrix entries for "A" and "B" are given separately)

1. x-MOMENTUM TERMS

$\tilde{u}$: I : $\int (\tilde{u}^+)^* \frac{i\beta\gamma \Pi^2 \bar{P} \tilde{w}}{\bar{T}} \tilde{u}\, dy = \int \tilde{u} \frac{i\beta\gamma \Pi^2 \bar{P} \tilde{w}}{\bar{T}} (\tilde{u}^+)^*\, dy$

II : $\int (\tilde{u}^+)^* \frac{i\alpha\gamma \Pi^2 \bar{P} \tilde{u}}{\bar{T}} \tilde{u}\, dy = \int \tilde{u} \frac{i\alpha\gamma \Pi^2 \bar{P} \tilde{u}}{\bar{T}} (\tilde{u}^+)^*\, dy$

III : $-\int (\tilde{u}^+)^* \frac{\bar{\mu}_T \bar{T}_y}{Re} D\tilde{u}\, dy$ Integration by parts:

↳ $-(\tilde{u}^+)^* \frac{\bar{\mu}_T \bar{T}_y}{Re} \tilde{u}\Big|^0 + \int \tilde{u}\, D\left\{(\tilde{u}^+)^* \frac{\bar{\mu}_T \bar{T}_y}{Re}\right\} dy$

↳ $\int \tilde{u} \left\{\frac{\bar{\mu}_T \bar{T}_y}{Re} D(\tilde{u}^+)^* + (\tilde{u}^+)^* D\left(\frac{\bar{\mu}_T \bar{T}_y}{Re}\right)\right\} dy$

↳ $\int \tilde{u} \left\{\frac{\bar{\mu}_T \bar{T}_y}{Re} D(\tilde{u}^+)^* + (\tilde{u}^+)^* \frac{\bar{\mu}_{TT} \bar{T}_y^2}{Re} + (\tilde{u}^+)^* \frac{\bar{\mu}_T \bar{T}_{yy}}{Re}\right\} dy$

IV : $-\int (\tilde{u}^+)^* \frac{\bar{\mu}}{Re} D^2\tilde{u}\, dy$ Integration by parts:

↳ $-(\tilde{u}^+)^* \frac{\bar{\mu}}{Re} D\tilde{u}\Big|^0 + \int D\left\{(\tilde{u}^+)^* \frac{\bar{\mu}}{Re}\right\} D\tilde{u}\, dy$

↳ $(= \int D\tilde{u} \left\{\frac{\bar{\mu}}{Re} D(\tilde{u}^+)^* + (\tilde{u}^+)^* \frac{\bar{\mu}_T \bar{T}_y}{Re}\right\} dy)$

↳ $\int \frac{\bar{\mu}}{Re} D(\tilde{u}^+)^* D\tilde{u}\, dy + \int \frac{\bar{\mu}_T \bar{T}_y}{Re} (\tilde{u}^+)^* D\tilde{u}\, dy$

↳ $\frac{\bar{\mu}}{Re} D(\tilde{u}^+)^* \tilde{u}\Big|^0 - \int \alpha D\left\{\frac{\bar{\mu}}{Re} D(\tilde{u}^+)^*\right\} dy$
$+ \frac{\bar{\mu}_T \bar{T}_y}{Re} (\tilde{u}^+)^* D\tilde{u}\Big|^0 - \int \tilde{u}\, D\left\{\frac{\bar{\mu}_T \bar{T}_y}{Re} (\tilde{u}^+)^*\right\} dy$

LASER VISION
Tel.: +31 (0)529-428000
www.laservision.nl

IV cont'd: $\Rightarrow -\int \tilde{u}\left\{\beta^2(\tilde{u}^+)^*\frac{\bar{\mu}}{Re}+\frac{\bar{\mu}_T\bar{T}_y}{Re}D(\tilde{u}^+)^*\right\}dy$
$-\int\tilde{u}\left\{D(\tilde{u}^+)^*\frac{\bar{\mu}_T\bar{T}_y}{Re}+(\tilde{u}^+)^*\frac{\bar{\mu}_{TT}\bar{T}_y^2}{Re}+(\tilde{u}^+)^*\frac{\bar{\mu}_T\bar{T}_{yy}}{Re}\right\}dy$

V: $\int(\tilde{u}^+)^*\frac{\beta^2\bar{\mu}}{Re}\tilde{u}\,dy=\int\tilde{u}\frac{\beta^2\bar{\mu}}{Re}(\tilde{u}^+)^*dy$

VI: $\int(\tilde{u}^+)^*\frac{2\alpha^2\bar{\mu}}{Re}\tilde{u}\,dy=\int\tilde{u}\frac{2\alpha^2\bar{\mu}}{Re}(\tilde{u}^+)^*dy$

VII: $\int(\tilde{u}^+)^*\frac{\alpha^2\bar{\lambda}}{Re}\tilde{u}\,dy=\int\tilde{u}\frac{\alpha^2\bar{\lambda}}{Re}(\tilde{u}^+)^*dy$

VIII: $\int(\tilde{u}^+)^*\frac{i\gamma\Pi^2\bar{P}}{\bar{T}}\tilde{u}\,dy=\int\tilde{u}\frac{i\gamma\Pi^2\bar{P}}{\bar{T}}(\tilde{u}^+)^*dy$

So for $(\tilde{u}^+)^*$: $A_{11}=\frac{-i\beta\gamma\Pi^2\bar{P}\bar{W}}{\bar{T}}+\frac{-i\alpha\gamma\Pi^2\bar{P}\bar{u}}{\bar{T}}+\frac{-\bar{\mu}_T\bar{T}_y}{Re}D$
$+\frac{\bar{\mu}_{TT}\bar{T}_y^2}{Re}+\frac{\bar{\mu}_T\bar{T}_{yy}}{Re}-\frac{\bar{\mu}}{Re}D^2-\frac{2\bar{\mu}_T\bar{T}_y}{Re}D$
$-\frac{\bar{\mu}_{TT}\bar{T}_y^2}{Re}-\frac{\bar{\mu}_T\bar{T}_{yy}}{Re}+\frac{\beta^2\bar{\mu}}{Re}+\frac{2\alpha^2\bar{\mu}}{Re}$
$+\frac{\alpha^2\bar{\lambda}}{Re}$

$B_{11}=\frac{-i\gamma\Pi^2\bar{P}}{\bar{T}}$

$\tilde{v}$: I: $\int(\tilde{u}^+)^*\frac{\gamma\Pi^2\bar{P}\bar{u}_y}{\bar{T}}\tilde{v}\,dy=\int\tilde{v}\frac{\gamma\Pi^2\bar{P}\bar{u}_y}{\bar{T}}(\tilde{u}^+)^*dy$
NOTE: transp. $\rightarrow A_{21}$

II: $-\int(\tilde{u}^+)^*\frac{i\alpha\bar{\mu}_T\bar{T}_y}{Re}\tilde{v}\,dy=-\int\tilde{v}\frac{i\alpha\bar{\mu}_T\bar{T}_y}{Re}(\tilde{u}^+)^*dy$

III: $-\int(\tilde{u}^+)^*\frac{i\alpha\bar{\mu}}{Re}D\tilde{v}\,dy$ Integration by parts:

$\hookrightarrow -(\tilde{u}^+)^*\frac{i\alpha\bar{\mu}}{Re}\tilde{v}\Big|^{\infty}+\int\tilde{v}\left\{\frac{i\alpha\bar{\mu}}{Re}D(\tilde{u}^+)^*+\frac{i\alpha\bar{\mu}_T\bar{T}_y}{Re}(\tilde{u}^+)^*\right\}dy$

LASER VISION
Tel.: +31 (0)529-428000
www.laservision.nl

III : $-\int(\tilde{u}^+)^* \frac{i\alpha\bar{\lambda}}{Re} D\tilde{v}\, dy$ Integration by parts :

$\Rightarrow -(\tilde{u}^+)^* \frac{i\alpha\bar{\lambda}}{Re}\tilde{v}\Big|^0 + \int \tilde{v}\left\{\frac{i\alpha\bar{\lambda}}{Re} D(\tilde{u}^+)^* + \frac{i\alpha\bar{\lambda}_T\bar{T}_y}{Re}(\tilde{u}^+)^*\right\} dy$

So for $(\tilde{u}^+)^*$: $A_{21} = \frac{\gamma\Pi^2\bar{P}\bar{u}_y}{\bar{T}} + \frac{i\alpha\bar{\mu}_T\bar{T}_y}{Re} + \frac{-i\alpha\bar{\mu}}{Re} D$

$(\tilde{v})$ $+ \frac{-i\alpha\bar{\mu}_T\bar{T}_y}{Re} + \frac{-i\alpha\bar{\lambda}}{Re} D + \frac{-i\alpha\bar{\lambda}_T\bar{T}_y}{Re}$

$B_{21} = 0$

$\hat{p}$: I: $\int(\tilde{u}^+)^* i\alpha\tilde{p}\, dy = \int\tilde{p}\, i\alpha(\tilde{u}^+)^* dy$

So for $(\tilde{u}^+)^*$: $A_{31} = -i\alpha$

$(\tilde{p})$ $B_{31} = 0$

$\tilde{w}$: I: $\int(\tilde{u}^+)^* \frac{\alpha\beta\bar{\mu}}{Re}\tilde{w}\, dy = \int\tilde{w}\frac{\alpha\beta\bar{\mu}}{Re}(\tilde{u}^+)^* dy$

II: $\int(\tilde{u}^+)^* \frac{\alpha\beta\bar{\lambda}}{Re}\tilde{w}\, dy = \int\tilde{w}\frac{\alpha\beta\bar{\lambda}}{Re}(\tilde{u}^+)^* dy$

So for $(\tilde{u}^+)^*$: $A_{g1} = \frac{\alpha\beta}{Re}(\bar{\mu}+\bar{\lambda})$

$(\tilde{w})$ $B_{g1} = 0$

$\tilde{T}$: I : $-\int(\tilde{u}^+)^* \frac{\bar{\mu}_T\bar{u}_{yy}}{Re}\tilde{T}\, dy = -\int\tilde{T}\frac{\bar{\mu}_T\bar{u}_{yy}}{Re}(\tilde{u}^+)^* dy$

II : $-\int(\tilde{u}^+)^* \frac{\bar{\mu}_T\bar{T}_y\bar{u}_y}{Re}\tilde{T}\, dy = -\int\tilde{T}\frac{\bar{\mu}_T\bar{T}_y\bar{u}_y}{Re}(\tilde{u}^+)^* dy$

III : $-\int(\tilde{u}^+)^* \frac{\bar{\mu}_T\bar{u}_y}{Re} D\tilde{T}\, dy$ Integration by parts :

$\Rightarrow -(\tilde{u}^+)^* \frac{\bar{\mu}_T\bar{u}_y}{Re}\tilde{T}\Big|^0 + \int\tilde{T}\left\{\frac{\bar{\mu}_T\bar{u}_y}{Re} D(\tilde{u}^+)^* + (\tilde{u}^+)^* \frac{\bar{\mu}_T\bar{u}_{yy}}{Re} + (\tilde{u}^+)^* \frac{\bar{\mu}_T\bar{T}_y\bar{u}_y}{Re}\right\} dy$

LASER VISION
Tel.: +31 (0)529-428000
www.laservision.nl

So for $(\tilde{u}^+)^*$: $A_{\tilde{T}1} = -\frac{\bar{\mu}_{\bar{T}}\bar{u}_{yy}}{Re} - \frac{\bar{\mu}_{\bar{T}\bar{T}}\bar{T}_y\bar{u}_y}{Re}$

$$+\frac{\bar{\mu}_{\bar{T}}\bar{u}_y}{Re}D + \frac{\bar{\mu}_{\bar{T}}\bar{u}_{yy}}{Re} + \frac{\bar{\mu}_{\bar{T}\bar{T}}\bar{T}_y\bar{u}_y}{Re}$$

$$B_{\tilde{T}1} = 0$$

2. y-MOMENTUM TERMS

$\tilde{u}$: I: $-\int (\tilde{v}^+)^* \frac{i\alpha\bar{\lambda}_{\bar{T}}\bar{T}_y}{Re}\tilde{u}\,dy = -\int \tilde{u}\frac{i\alpha\bar{\lambda}_{\bar{T}}\bar{T}_y}{Re}(\tilde{v}^+)^*\,dy$

II: $-\int (\tilde{v}^+)^* \frac{i\alpha\bar{\mu}}{Re}D\tilde{u}\,dy$ Integration by parts:

$$\hookrightarrow -(\tilde{v}^+)^*\frac{i\alpha\bar{\mu}}{Re}\tilde{u}\Big|^0 + \int\tilde{u}\left\{\frac{i\alpha\bar{\mu}}{Re}D(\tilde{v}^+)^* + (\tilde{v}^+)^*\frac{i\alpha\bar{\mu}_{\bar{T}}\bar{T}_y}{Re}\right\}dy$$

III: $-\int (\tilde{v}^+)^* \frac{i\alpha\bar{\lambda}}{Re}D\tilde{u}\,dy$ Integration by parts:

$$\hookrightarrow -(\tilde{v}^+)^*\frac{i\alpha\bar{\lambda}}{Re}\tilde{u}\Big|^0 + \int\tilde{u}\left\{\frac{i\alpha\bar{\lambda}}{Re}D(\tilde{v}^+)^* + (\tilde{v}^+)^*\frac{i\alpha\bar{\lambda}_{\bar{T}}\bar{T}_y}{Re}\right\}dy$$

So for $(\tilde{v}^+)^*$: $A_{12} = +\frac{i\alpha\bar{\lambda}_{\bar{T}}\bar{T}_y}{Re} + \frac{-i\alpha\bar{\mu}}{Re}D + \frac{-i\alpha\bar{\mu}_{\bar{T}}\bar{T}_y}{Re}$

$$+\frac{-i\alpha\bar{\lambda}}{Re}D + \frac{-i\alpha\bar{\lambda}_{\bar{T}}\bar{T}_y}{Re}$$

$$B_{12} = 0$$

$\tilde{v}$: I: $\int (\tilde{v}^+)^* \frac{i\beta\gamma\Pi^2\bar{P}\tilde{w}}{\bar{T}}\tilde{v}\,dy = \int\tilde{v}\frac{i\beta\gamma\Pi^2\bar{P}\tilde{w}}{\bar{T}}(\tilde{v}^+)^*\,dy$

II: $\int (\tilde{v}^+)^* \frac{i\alpha\gamma\Pi^2\bar{P}\tilde{u}}{\bar{T}}\tilde{v}\,dy = \int\tilde{v}\frac{i\alpha\gamma\Pi^2\bar{P}\tilde{u}}{\bar{T}}(\tilde{v}^+)^*\,dy$

III: $-\int (\tilde{v}^+)^* \frac{2\bar{\mu}_{\bar{T}}\bar{T}_y}{Re}D\tilde{v}\,dy$ Integration by parts:

$$\hookrightarrow -(\tilde{v}^+)^*\frac{2\bar{\mu}_{\bar{T}}\bar{T}_y}{Re}\tilde{v}\Big|^0 + \int\tilde{v}\left\{\frac{2\bar{\mu}_{\bar{T}}\bar{T}_y}{Re}D(\tilde{v}^+)^* + (\tilde{v}^+)^*\frac{2\bar{\mu}_{\bar{T}}\bar{T}_{yy}}{Re} + (\tilde{v}^+)^*\frac{2\bar{\mu}_{\bar{T}\bar{T}}\bar{T}_y^2}{Re}\right\}dy$$

LASER VISION
Tel.: +31 (0)529-428000
www.laservision.nl

IV : $-\int (\tilde{v}^+)^* \frac{\bar{\lambda}_T \bar{T}_y}{Re} D\tilde{v}\, dy$ Integration by parts :

$\Rightarrow -(v^+)^* \frac{\bar{\lambda}_T \bar{T}_y}{Re} \tilde{v}\Big|^0 + \int \tilde{v} \left\{ \frac{\bar{\lambda}_T \bar{T}_y}{Re} D(\tilde{v}^+)^* + (\tilde{v}^+)^* \frac{\bar{\lambda}_T \bar{T}_{yy}}{Re} + (\tilde{v}^+)^* \frac{\bar{\lambda}_{TT} \bar{T}_y^2}{Re} \right\} dy$

V : $-\int (\tilde{v}^+)^* \frac{2\bar{\mu}}{Re} D^2\tilde{v}\, dy$ Integration by parts :

$\Rightarrow -(v^+)^* \frac{2\bar{\mu}}{Re} \tilde{v}\Big|^0 + \int \tilde{v} \left\{ \frac{2\bar{\mu}}{Re} D(\tilde{v}^+)^* + (\tilde{v}^+)^* \frac{2\bar{\mu}_T \bar{T}_y}{Re} \right\} dy$

$\Rightarrow \left\{ \frac{2\bar{\mu}}{Re} D(\tilde{v}^+)^* + (\tilde{v}^+)^* \frac{2\bar{\mu}_T \bar{T}_y}{Re} \right\} \tilde{v}\Big|^0 -$

VI : $\int (\tilde{v}^+)^* \frac{\beta^2 \bar{\mu}}{Re} \tilde{v}\, dy = \int \tilde{v} \frac{\beta^2 \bar{\mu}}{Re} (\tilde{v}^+)^*\, dy$

VII : $\int (\tilde{v}^+)^* \frac{\alpha^2 \bar{\mu}}{Re} \tilde{v}\, dy = \int \tilde{v} \frac{\alpha^2 \bar{\mu}}{Re} (\tilde{v}^+)^*\, dy$

$\int \tilde{v} \left\{ \frac{2\bar{\mu}}{Re} D^2(\tilde{v}^+)^* + \frac{4\bar{\mu}_T \bar{T}_y}{Re} D(\tilde{v}^+)^* + (\tilde{v}^+)^* \frac{2\bar{\mu}_{TT} \bar{T}_y^2}{Re} + (\tilde{v}^+)^* \frac{2\bar{\mu}_T \bar{T}_{yy}}{Re} \right\} dy$

VIII : $-\int (\tilde{v}^+)^* \frac{\bar{\lambda}}{Re} D^2\tilde{v}\, dy$ Integration by parts :

$\Rightarrow -(v^+)^* \frac{\bar{\lambda}}{Re} D\tilde{v}\Big|^0 + \int D\tilde{v} \left\{ \frac{\bar{\lambda}}{Re} D(\tilde{v}^+)^* + (\tilde{v}^+)^* \frac{\bar{\lambda}_T \bar{T}_y}{Re} \right\} dy$

$\Rightarrow \left\{ \frac{\bar{\lambda}}{Re} D(\tilde{v}^+)^* + (\tilde{v}^+)^* \frac{\bar{\lambda}_T \bar{T}_y}{Re} \right\} \tilde{v}\Big|^0$

$-\int \tilde{v} \left\{ \frac{\bar{\lambda}}{Re} D^2(\tilde{v}^+)^* + 2\frac{\bar{\lambda}_T \bar{T}_y}{Re} D(\tilde{v}^+)^* + (\tilde{v}^+)^* \frac{\bar{\lambda}_{TT} \bar{T}_y^2}{Re} + (\tilde{v}^+)^* \frac{\bar{\lambda}_T \bar{T}_{yy}}{Re} \right\} dy$

IX : $\int (\tilde{v}^+)^* \frac{i\gamma \Pi^2 \bar{P}}{\bar{T}} \tilde{v}\, dy = \int \tilde{v} \frac{i\gamma \Pi^2 \bar{P}}{\bar{T}} (\tilde{v}^+)^*\, dy$

So for $(\tilde{v}^+)^*$: $A_{zz} = -\frac{i\beta\gamma \Pi^2 \bar{P} \tilde{w}}{\bar{T}} + \frac{-i\alpha\gamma \Pi^2 \bar{P} \tilde{u}}{\bar{T}} - \frac{2\bar{\mu}_T \bar{T}_y}{Re} D$

$(\tilde{v})$

$+ \frac{2\bar{\mu}_T \bar{T}_{yy}}{Re} + \frac{2\bar{\mu}_{TT} \bar{T}_y^2}{Re}$

$- \frac{\bar{\lambda}_T \bar{T}_y}{Re} D + \frac{\bar{\lambda}_T \bar{T}_{yy}}{Re} + \frac{\bar{\lambda}_{TT} \bar{T}_y^2}{Re}$

$- \frac{2\bar{\mu}}{Re} D^2 - \frac{4\bar{\mu}_T \bar{T}_y}{Re} D + \frac{\beta^2 \bar{\mu}}{Re} + \frac{\alpha^2 \bar{\mu}}{Re} - \frac{2\bar{\mu}_{TT} \bar{T}_y^2}{Re} - \frac{2\bar{\mu}_T \bar{T}_{yy}}{Re}$

$- \frac{\bar{\lambda}}{Re} D^2 - \frac{2\bar{\lambda}_T \bar{T}_y}{Re} D - \frac{\bar{\lambda}_{TT} \bar{T}_y^2}{Re} - \frac{\bar{\lambda}_T \bar{T}_{yy}}{Re}$

LASER VISION
Tel.: +31 (0)529-428000
www.laservision.nl

cont'd. $B_{22} = \dfrac{-i\gamma\Pi^2\bar{p}}{\bar{T}}$

$\tilde{p}$: I : $\int (\tilde{v}^+)^* D\tilde{p}\, dy$ Integration by parts:

$\Rightarrow (\tilde{v}^+)^*\tilde{p}\Big|_0^0 - \int \tilde{p}\, D(\tilde{v}^+)^*\, dy$

So for $(\tilde{v}^+)^*$: $A_{32} = -D$

$(\tilde{p})$ $B_{32} = 0$

$\tilde{w}$: I: $-\int (\tilde{v}^+)^* \dfrac{i\beta\bar{\lambda}_T\bar{T}_y}{Re}\tilde{w}\, dy = -\int \tilde{w}\dfrac{i\beta\bar{\lambda}_T\bar{T}_y}{Re}(\tilde{v}^+)^*\, dy$

II: $-\int (\tilde{v}^+)^* \dfrac{i\beta\bar{\mu}}{Re} D\tilde{w}\, dy$ Integration by parts:

$\Rightarrow -(\tilde{v}^+)^*\dfrac{i\beta\bar{\mu}}{Re}\tilde{w}\Big|_0^0 + \int \tilde{w}\left\{\dfrac{i\beta\bar{\mu}}{Re}D(\tilde{v}^+)^* + (\tilde{v}^+)^*\dfrac{i\beta\bar{\mu}_T\bar{T}_y}{Re}\right\} dy$

III: $-\int (\tilde{v}^+)^* \dfrac{i\beta\bar{\lambda}}{Re} D\tilde{w}\, dy$ Integration by parts:

$\Rightarrow -(\tilde{v}^+)^*\dfrac{i\beta\bar{\lambda}}{Re}\tilde{w}\Big|_0^0 + \int \tilde{w}\left\{\dfrac{i\beta\bar{\lambda}}{Re}D(\tilde{v}^+)^* + (\tilde{v}^+)^*\dfrac{i\beta\bar{\lambda}_T\bar{T}_y}{Re}\right\} dy$

So for $(\tilde{v}^+)^*$: $A_{52} = +\dfrac{i\beta\bar{\lambda}_T\bar{T}_y}{Re} + \dfrac{-i\beta\bar{\mu}}{Re}D + \dfrac{-i\beta\bar{\mu}_T\bar{T}_y}{Re}$

$(\tilde{w})$ $+\dfrac{-i\beta\bar{\lambda}}{Re}D + \dfrac{-i\beta\bar{\lambda}_T\bar{T}_y}{Re}$

$B_{52} = 0$

$\tilde{T}$: I : $-\int (\tilde{v}^+)^* \dfrac{i\beta\bar{\mu}_T\bar{w}_y}{Re}\tilde{T}\, dy = -\int \tilde{T}\dfrac{i\beta\bar{\mu}_T\bar{w}_y}{Re}(\tilde{v}^+)^*\, dy$

II : $-\int (\tilde{v}^+)^* \dfrac{i\alpha\bar{\mu}_T\bar{u}_y}{Re}\tilde{T}\, dy = -\int \tilde{T}\dfrac{i\alpha\bar{\mu}_T\bar{u}_y}{Re}(\tilde{v}^+)^*\, dy$

So for $(\tilde{v}^+)^*$: $A_{42} = +\dfrac{i\beta\bar{\mu}_T\bar{w}_y}{Re} + \dfrac{i\alpha\bar{\mu}_T\bar{u}_y}{Re}$

$(\tilde{T})$ $B_{42} = 0$

LASER VISION
Tel.: +31 (0)529-428000
www.laservision.nl

3. CONTINUITY TERMS

$\tilde{u}$: I : $\int (\tilde{p}^+)^* i\alpha \bar{P} \tilde{u}\, dy = \int \tilde{u}\, i\alpha \bar{P} (\tilde{p}^+)^*\, dy$

So for $(\tilde{p}^+)^*$: $A_{13} = -i\alpha \bar{P}$

$(\tilde{u})$ $B_{13} = 0$

$\tilde{v}$: I : $-\int (\tilde{p}^+)^* \frac{\overline{PT}_y}{\bar{T}} \tilde{v}\, dy = -\int \tilde{v} \frac{\overline{PT}_y}{\bar{T}} (\tilde{p}^+)^*\, dy$

II : $\int (\tilde{p}^+)^* \bar{P}_y \tilde{v}\, dy = \int \tilde{v} \bar{P}_y (\tilde{p}^+)^*\, dy$

III : $\int (\tilde{p}^+)^* \bar{P} D\tilde{v}\, dy$ Integration by parts :

$\hookrightarrow (\tilde{p}^+)^* \bar{P} \tilde{v}\Big|^{\infty} - \int \tilde{v} \{ \bar{P} D(\tilde{p}^+)^* + (\tilde{p}^+)^* \bar{P}_y \}\, dy$

So for $(\tilde{p}^+)^*$: $A_{23} = -\frac{\overline{PT}_y}{\bar{T}} + \cancel{\bar{P}_y} - \cancel{\bar{P}_y} - \bar{P}D$

$(\tilde{v})$ $B_{23} = 0$

$\tilde{p}$: I : $\int (\tilde{p}^+)^* i\beta \bar{W} \tilde{p}\, dy = \int \tilde{p}\, i\beta \bar{W} (\tilde{p}^+)^*\, dy$

II : $\int (\tilde{p}^+)^* i\alpha \bar{u} \tilde{p}\, dy = \int \tilde{p}\, i\alpha \bar{u} (\tilde{p}^+)^*\, dy$

III : $\int (\tilde{p}^+)^* i\tilde{p}\, dy = \int \tilde{p}\, i (\tilde{p}^+)^*\, dy$

So for $(\tilde{p}^+)^*$: $A_{33} = -i\beta \bar{W} - i\alpha \bar{u}$

$(\tilde{p})$ $B_{33} = -i$

$\tilde{w}$: I : $\int (\tilde{p}^+)^* i\beta \bar{P} \tilde{w}\, dy = \int \tilde{w}\, i\beta \bar{P} (\tilde{p}^+)^*\, dy$

So for $(\tilde{p}^+)^*$: $A_{53} = -i\beta \bar{P}$

$(\tilde{w})$ $B_{53} = 0$

LASER VISION
Tel.: +31 (0)529-428000
www.laservision.nl

$\tilde{T}$: I : $-\int (\tilde{p}^+)^* \frac{i\beta \bar{p}\bar{w}}{\bar{T}} \tilde{T}\, dy = -\int \tilde{T} \frac{i\beta \bar{p}\bar{w}}{\bar{T}} (\tilde{p}^+)^*\, dy$

II : $-\int (\tilde{p}^+)^* \frac{i\alpha \bar{p}\bar{u}}{\bar{T}} \tilde{T}\, dy = -\int \tilde{T} \frac{i\alpha \bar{p}\bar{u}}{\bar{T}} (\tilde{p}^+)^*\, dy$

III : $\int (\tilde{p}^+)^* \frac{i\bar{p}}{\bar{T}} \tilde{T}\, dy = \int \tilde{T} \frac{i\bar{p}}{\bar{T}} (\tilde{p}^+)^*\, dy$

So for $(\tilde{p}^+)^*$: $A_{43} = + \frac{i\beta \bar{p}\bar{w}}{\bar{T}} + \frac{i\alpha \bar{p}\bar{u}}{\bar{T}}$

$(\tilde{T})$ $B_{43} = + \frac{i\bar{p}}{\bar{T}}$

4. ENERGY TERMS

$\tilde{u}$: I : $-\int (\tilde{T}^+)^* \frac{2(\gamma-1)\Pi^2 \bar{\mu}\bar{u}_y}{Re} D\tilde{u}\, dy$ Integration by parts:

$\rightarrow -(\tilde{T}^+)^* \frac{2(\gamma-1)\Pi^2 \bar{\mu}\bar{u}_y}{Re} \tilde{u}\Big|^0 + \int \tilde{u} \Big\{ \frac{2(\gamma-1)\Pi^2 \bar{\mu}\bar{u}_y}{Re} D(\tilde{T}^+)^*$

$+ (\tilde{T}^+)^* \frac{2(\gamma-1)\Pi^2 \bar{\mu}\bar{u}_{yy}}{Re}$

$+ (\tilde{T}^+)^* \frac{2(\gamma-1)\Pi^2 \bar{\mu}_T \bar{T}_y \bar{u}_y}{Re} \Big\}\, dy$

So for $(\tilde{T}^+)^*$: $A_{14} = \frac{2(\gamma-1)\Pi^2}{Re} \{ \bar{\mu}\bar{u}_y D + \bar{\mu}\bar{u}_{yy} + \bar{\mu}_T \bar{T}_y u_y \}$

$(\tilde{u})$ $B_{14} = 0$

$\tilde{v}$: I : $\int (\tilde{T}^+)^* \frac{\gamma \Pi^2 \bar{p}\bar{T}_y}{\bar{T}} \tilde{v}\, dy = \int \tilde{v} \frac{\gamma \Pi^2 \bar{p}\bar{T}_y}{\bar{T}} (\tilde{T}^+)^*\, dy$

II : $-\int (\tilde{T}^+)^* \frac{2i\beta(\gamma-1)\Pi^2 \bar{\mu}\bar{w}_y}{Re} \tilde{v}\, dy = -\int \tilde{v} \frac{2i\beta(\gamma-1)\Pi^2 \bar{\mu}\bar{w}_y}{Re} (\tilde{T}^+)^*\, dy$

III : $-\int (\tilde{T}^+)^* \frac{2i\alpha(\gamma-1)\Pi^2 \bar{\mu}\bar{u}_y}{Re} \tilde{v}\, dy = -\int \tilde{v} \frac{2i\alpha(\gamma-1)\Pi^2 \bar{\mu}\bar{u}_y}{Re} (\tilde{T}^+)^*\, dy$

IV : $-\int (\tilde{T}^+)^* (\gamma-1)\Pi^2 \bar{p}_y \tilde{v}\, dy = -\int \tilde{v} (\gamma-1)\Pi^2 \bar{p}_y (\tilde{T}^+)^*\, dy$

LASER VISION
Tel.: +31 (0)529-428000
www.laservision.nl

So for $(\tilde{T}^+)^*$: $A_{24} = \frac{\gamma \Pi^2 \bar{p} \bar{T}_y}{\bar{T}} + \frac{2i\beta(\gamma-1)\Pi^2 \bar{\mu} \bar{W}_y}{Re}$

$(\tilde{v})$ $+ \frac{2i\alpha(\gamma-1)\Pi^2 \bar{\mu} \bar{u}_y}{Re} - (\gamma-1)\Pi^2 \bar{p}_y$

$B_{24} = 0$

$\tilde{p}$: I : $-\int (\tilde{T}^+)^* i\beta(\gamma-1)\Pi^2 \bar{W} \tilde{p}\, dy = -\int \tilde{p}\, i\beta(\gamma-1)\Pi^2 \bar{W} (\tilde{T}^+)^* dy$

II : $-\int (\tilde{T}^+)^* i\alpha(\gamma-1)\Pi^2 \bar{u} \tilde{p}\, dy = -\int \tilde{p}\, i\alpha(\gamma-1)\Pi^2 \bar{u} (\tilde{T}^+)^* dy$

III : $-\int (\tilde{T}^+)^* i(\gamma-1)\Pi^2 \tilde{p}\, dy = -\int \tilde{p}\, i(\gamma-1)\Pi^2 (\tilde{T}^+)^* dy$

So for $(\tilde{T}^+)^*$: $A_{34} = +i\beta(\gamma-1)\Pi^2 \bar{W} + i\alpha(\gamma-1)\Pi^2 \bar{u}$

$(\tilde{p})$ $B_{34} = +i(\gamma-1)\Pi^2$

$\tilde{W}$: I : $-\int (\tilde{T}^+)^* \frac{2(\gamma-1)\Pi^2 \bar{\mu} \bar{W}_y}{Re} D\tilde{W}\, dy$ Integration by parts

$\hookrightarrow -(\tilde{T}^+)^* \frac{2(\gamma-1)\Pi^2 \bar{\mu} \bar{W}_y}{Re} \tilde{W}\Big|^0 + \int \tilde{W} \Big\{ \frac{2(\gamma-1)\Pi^2 \bar{\mu} \bar{W}_y}{Re} D(\tilde{T}^+)^*$

$+ (\tilde{T}^+)^* \frac{2(\gamma-1)\Pi^2 \bar{\mu} \bar{W}_{yy}}{Re}$

$+ (\tilde{T}^+)^* \frac{2(\gamma-1)\Pi^2 \bar{\mu}_T \bar{T}_y \bar{W}_y}{Re} \Big\} dy$

So for $(\tilde{T}^+)^*$: $A_{54} = \frac{2(\gamma-1)\Pi^2}{Re} \{ \bar{\mu} \bar{W}_y D + \bar{\mu} \bar{W}_{yy} + \bar{\mu}_T \bar{T}_y \bar{W}_y \}$

$(\tilde{w})$ $B_{54} = 0$

$\tilde{T}$: I : $\int (\tilde{T}^+)^* \frac{i\beta\gamma \Pi^2 \bar{p} \bar{W}}{\bar{T}} \tilde{T}\, dy = \int \tilde{T} \frac{i\beta\gamma \Pi^2 \bar{p} \bar{W}}{\bar{T}} (\tilde{T}^+)^* dy$

II : $\int (\tilde{T}^+)^* \frac{i\alpha\gamma \Pi^2 \bar{p} \bar{u}}{\bar{T}} \tilde{T}\, dy = \int \tilde{T} \frac{i\alpha\gamma \Pi^2 \bar{p} \bar{u}}{\bar{T}} (\tilde{T}^+)^* dy$

III : $-\int (\tilde{T}^+)^* \frac{(\gamma-1)\Pi^2 \bar{\mu}_T \bar{W}_y^2}{Re} \tilde{T}\, dy = -\int \tilde{T} \frac{(\gamma-1)\Pi^2 \bar{\mu}_T \bar{W}_y^2}{Re} (\tilde{T}^+)^* dy$

LASER VISION
Tel.: +31 (0)529-428000
www.laservision.nl

IV : $-\int (\tilde{T}^+)^* \frac{(\gamma-1)\Pi^2 \bar{\mu}_T (\bar{u}_y)^2}{Re} \tilde{T}\, dy = -\int \tilde{T} \frac{(\gamma-1)\Pi^2 \bar{\mu}_T \bar{u}_y^2}{Re} (\tilde{T}^+)^*\, dy$

V : $-\int (\tilde{T}^+)^* \frac{\bar{K}_T \bar{T}_{yy}}{Pr\, Re} \tilde{T}\, dy = -\int \tilde{T} \frac{\bar{K}_T \bar{T}_{yy}}{Pr\, Re} (\tilde{T}^+)^*\, dy$

VI : $-\int (\tilde{T}^+)^* \frac{\bar{K}_{TT} \bar{T}_y^2}{Pr\, Re} \tilde{T}\, dy = -\int \tilde{T} \frac{\bar{K}_{TT} \bar{T}_y^2}{Pr\, Re} (\tilde{T}^+)^*\, dy$

VII : $-\int (\tilde{T}^+)^* \frac{2\bar{K}_T \bar{T}_y}{Pr\, Re} D\tilde{T}\, dy$ Integration by parts:

$\Rightarrow -(\tilde{T}^+)^* \frac{2\bar{K}_T \bar{T}_y}{Pr\, Re} \tilde{T}\Big|^0 + \int \tilde{T} \Big\{ \frac{2\bar{K}_T \bar{T}_y}{Pr\, Re} D(\tilde{T}^+)^* + (\tilde{T}^+)^* \frac{2\bar{K}_T \bar{T}_{yy}}{Pr\, Re} + (\tilde{T}^+)^* \frac{2\bar{K}_{TT} \bar{T}_y^2}{Pr\, Re} \Big\}\, dy$

VIII : $-\int (\tilde{T}^+)^* \frac{\bar{K}}{Pr\, Re} D^2\tilde{T}\, dy$ Integration by parts:

$\Rightarrow -(\tilde{T}^+)^* \frac{\bar{K}}{Pr\, Re} D\tilde{T}\Big|^0 + \int D\tilde{T} \Big\{ \frac{\bar{K}}{Pr\, Re} D(\tilde{T}^+)^* + (\tilde{T}^+)^* \frac{\bar{K}_T \bar{T}_y}{Pr\, Re} \Big\}\, dy$

$\Rightarrow \Big\{ \frac{\bar{K}}{Pr\, Re} D(\tilde{T}^+)^* + (\tilde{T}^+)^* \frac{\bar{K}_T \bar{T}_y}{Pr\, Re} \Big\} \tilde{T}\Big|^0$

$- \int \tilde{T} \Big\{ \frac{\bar{K}}{Pr\, Re} D^2(\tilde{T}^+)^* + 2\frac{\bar{K}_T \bar{T}_y}{Pr\, Re} D(\tilde{T}^+)^* + (\tilde{T}^+)^* \frac{\bar{K}_T \bar{T}_{yy}}{Pr\, Re} + (\tilde{T}^+)^* \frac{\bar{K}_{TT} \bar{T}_y^2}{Pr\, Re} \Big\}\, dy$

IX : $\int (\tilde{T}^+)^* \frac{\beta^2 \bar{K}}{Pr\, Re} \tilde{T}\, dy = \int \tilde{T} \frac{\beta^2 \bar{K}}{Pr\, Re} (\tilde{T}^+)^*\, dy$

X : $\int (\tilde{T}^+)^* \frac{\alpha^2 \bar{K}}{Pr\, Re} \tilde{T}\, dy = \int \tilde{T} \frac{\alpha^2 \bar{K}}{Pr\, Re} (\tilde{T}^+)^*\, dy$

XI : $\int (\tilde{T}^+)^* \frac{i\gamma \Pi^2 \bar{P}}{\bar{T}} \tilde{T}\, dy = \int \tilde{T} \frac{i\gamma \Pi^2 \bar{P}}{\bar{T}} (\tilde{T}^+)^*\, dy$

LASER VISION
Tel.: +31 (0)529-428000
www.laservision.nl

So for $(\tilde{T}^+)^*$: $A_{44} = -\frac{i\beta\gamma\Pi^2\bar{P}\bar{w}}{\bar{T}} + \frac{i\alpha\gamma\Pi^2\bar{P}\bar{u}}{\bar{T}} - \frac{(\gamma-1)\Pi^2\bar{\mu}_T\bar{w}_y^2}{Re}$

$(\tilde{T})$

$$- \frac{(\gamma-1)\Pi^2\bar{\mu}_T\bar{u}_y^2}{Re} - \frac{\bar{k}_T\bar{T}_{yy}}{Pr\,Re} - \frac{\bar{k}_{TT}\bar{T}_y^2}{Pr\,Re}$$

$$+ \frac{2\bar{k}_T\bar{T}_y}{Pr\,Re}D + \frac{2\bar{k}_T\bar{T}_{yy}}{Pr\,Re} + \frac{2\bar{k}_{TT}\bar{T}_y^2}{Pr\,Re}$$

$$- \frac{\bar{k}}{Pr\,Re}D^2 - \frac{2\bar{k}_T\bar{T}_y}{Pr\,Re}D - \frac{\bar{k}_T\bar{T}_{yy}}{Pr\,Re}$$

$$- \frac{\bar{k}_T\bar{T}_y^2}{Pr\,Re} + \frac{\beta^2\bar{k}}{Pr\,Re} + \frac{\alpha^2\bar{k}}{Pr\,Re}$$

$$B_{44} = -\frac{i\gamma\Pi^2\bar{P}}{\bar{T}}$$

5. Z-MOMENTUM TERMS

$\tilde{u}$: I : $\int(\tilde{w}^+)^*\frac{\alpha\beta\bar{\mu}}{Re}\tilde{u}\,dy = \int\tilde{u}\frac{\alpha\beta\bar{\mu}}{Re}(\tilde{w}^+)^*\,dy$

II : $\int(\tilde{w}^+)^*\frac{\alpha\beta\bar{\lambda}}{Re}\tilde{u}\,dy = \int\tilde{u}\frac{\alpha\beta\bar{\lambda}}{Re}(\tilde{w}^+)^*\,dy$

So for $(\tilde{w}^+)^*$: $A_{15} = \frac{\alpha\beta\bar{\mu}}{Re} + \frac{\alpha\beta\bar{\lambda}}{Re}$

$(\tilde{u})$ $B_{15} = 0$

$\tilde{v}$: I : $\int(\tilde{w}^+)^*\frac{\gamma\Pi^2\bar{P}\bar{w}_y}{\bar{T}}\tilde{v}\,dy = \int\tilde{v}\frac{\gamma\Pi^2\bar{P}\bar{w}_y}{\bar{T}}(\tilde{w}^+)^*\,dy$

II : $-\int(\tilde{w}^+)^*\frac{i\beta\bar{\mu}_T\bar{T}_y}{Re}\tilde{v}\,dy = -\int\tilde{v}\frac{i\beta\bar{\mu}_T\bar{T}_y}{Re}(\tilde{w}^+)^*\,dy$

III : $-\int(\tilde{w}^+)^*\frac{i\beta\bar{\mu}}{Re}D\tilde{v}\,dy$ Integration by parts :

$$\hookrightarrow -(\tilde{w}^+)^*\frac{i\beta\bar{\mu}}{Re}\tilde{v}\Big|^0 + \int\tilde{v}\left\{\frac{i\beta\bar{\mu}}{Re}D(\tilde{w}^+)^* + (\tilde{w}^+)^*\frac{i\beta\bar{\mu}_T\bar{T}_y}{Re}\right\}dy$$

LASER VISION
Tel.: +31 (0)529-428000
www.laservision.nl

IV : $-\int (\tilde{w}^+)^* \frac{i\beta\bar{\lambda}}{Re} D\tilde{v}\, dy$ Integration by parts :

$\Rightarrow -(\tilde{w}^+)^* \frac{i\beta\bar{\lambda}}{Re}\tilde{v}\Big|^0 + \int \tilde{v}\left\{\frac{i\beta\bar{\lambda}}{Re} D(\tilde{w}^+)^* + (\tilde{w}^+)^* \frac{i\beta\bar{\lambda}_T\bar{T}_y}{Re}\right\} dy$

So for $(\tilde{w}^+)^*$: $A_{25} = \frac{\gamma\Pi^2\bar{P}\bar{W}_y}{\bar{T}} + \frac{i\beta\bar{\mu}_T\bar{T}_y}{Re} - \frac{i\beta\bar{\mu}}{Re} D - \frac{i\beta\bar{\mu}_T\bar{T}_y}{Re} - \frac{i\beta\bar{\lambda}}{Re} D - \frac{i\beta\bar{\lambda}_T\bar{T}_y}{Re}$

$(\tilde{v})$

$B_{25} = 0$

$\tilde{p}$: I : $\int (\tilde{w}^+)^* i\beta\tilde{p}\, dy = \int \tilde{p}\, i\beta (\tilde{w}^+)^* dy$

So for $(\tilde{w}^+)^*$: $A_{35} = -i\beta$

$(\tilde{p})$ $B_{35} = 0$

$\tilde{w}$: I : $\int (\tilde{w}^+)^* \frac{i\beta\gamma\Pi^2\bar{P}\bar{W}}{\bar{T}}\tilde{w}\, dy = \int \tilde{w} \frac{i\beta\gamma\Pi^2\bar{P}\bar{W}}{\bar{T}} (\tilde{w}^+)^* dy$

II : $\int (\tilde{w}^+)^* \frac{i\alpha\gamma\Pi^2\bar{P}\bar{u}}{\bar{T}}\tilde{w}\, dy = \int \tilde{w} \frac{i\alpha\gamma\Pi^2\bar{P}\bar{u}}{\bar{T}} (\tilde{w}^+)^* dy$

III : $-\int (\tilde{w}^+)^* \frac{\bar{\mu}_T\bar{T}_y}{Re} D\tilde{w}\, dy$ Integration by parts :

$\Rightarrow -(\tilde{w}^+)^* \frac{\bar{\mu}_T\bar{T}_y}{Re}\tilde{w}\Big|^0 + \int \tilde{w}\left\{\frac{\bar{\mu}_T\bar{T}_y}{Re} D(\tilde{w}^+)^* + (\tilde{w}^+)^* \frac{\bar{\mu}_T\bar{T}_{yy}}{Re} + (\tilde{w}^+)^* \frac{\bar{\mu}_{TT}\bar{T}_y^2}{Re}\right\} dy$

IV : $-\int (\tilde{w}^+)^* \frac{\bar{\mu}}{Re} D^2\tilde{w}\, dy$ Integration by parts :

$\Rightarrow -(\tilde{w}^+)^* \frac{\bar{\mu}}{Re} D\tilde{w}\Big|^0 + \int D\tilde{w}\left\{\frac{\bar{\mu}}{Re} D(\tilde{w}^+)^* + (\tilde{w}^+)^* \frac{\bar{\mu}_T\bar{T}_y}{Re}\right\} dy$

$\Rightarrow \left\{\frac{\bar{\mu}}{Re} D(\tilde{w}^+)^* + (\tilde{w}^+)^* \frac{\bar{\mu}_T\bar{T}_y}{Re}\right\}\tilde{w}\Big|^0 - \int \tilde{w}\left\{\frac{\bar{\mu}}{Re} D^2(\tilde{w}^+)^* + 2\frac{\bar{\mu}_T\bar{T}_y}{Re} D(\tilde{w}^+)^* + (\tilde{w}^+)^* \frac{\bar{\mu}_T\bar{T}_{yy}}{Re} + (\tilde{w}^+)^* \frac{\bar{\mu}_{TT}\bar{T}_y^2}{Re}\right\} dy$

LASER VISION
Tel.: +31 (0)529-428000
www.laservision.nl

V: $\int (\tilde{w}^+)^* \frac{2\beta^2\bar{\mu}}{Re}\tilde{w}\,dy = \int \tilde{w}\frac{2\beta^2\bar{\mu}}{Re}(\tilde{w}^+)^*\,dy$

VI: $\int (\tilde{w}^+)^* \frac{\alpha^2\bar{\mu}}{Re}\tilde{w}\,dy = \int \tilde{w}\frac{\alpha^2\bar{\mu}}{Re}(\tilde{w}^+)^*\,dy$

VII: $\int (\tilde{w}^+)^* \frac{\beta^2\bar{\lambda}}{Re}\tilde{w}\,dy = \int \tilde{w}\frac{\beta^2\bar{\lambda}}{Re}(\tilde{w}^+)^*\,dy$

VIII: $\int (\tilde{w}^+)^* \frac{i\gamma\Pi^2\bar{p}}{\bar{T}}\tilde{w}\,dy = \int \tilde{w}\frac{i\gamma\Pi^2\bar{p}}{\bar{T}}(\tilde{w}^+)^*\,dy$

So for $(\tilde{w}^+)^*$: $A_{55} = \frac{-i\beta\gamma\Pi^2\bar{p}\bar{w}}{\bar{T}} + \frac{-i\alpha\gamma\Pi^2\bar{p}\bar{u}}{\bar{T}} + \frac{-\bar{\mu}_T\bar{T}_y}{Re}D$

$(\tilde{w})$

$+\frac{\bar{\mu}_T\bar{T}_{yy}}{Re} + \frac{\bar{\mu}_{TT}\bar{T}_y^2}{Re} - \frac{\bar{\mu}}{Re}D^2$

$+2\frac{\bar{\mu}_T\bar{T}_y}{Re}D - \frac{\bar{\mu}_T\bar{T}_{yy}}{Re} - \frac{\bar{\mu}_{TT}\bar{T}_y^2}{Re}$

$+\frac{2\beta^2\bar{\mu}}{Re} + \frac{\alpha^2\bar{\mu}}{Re} + \frac{\beta^2\bar{\lambda}}{Re}$

$B_{55} = -\frac{i\gamma\Pi^2\bar{p}}{\bar{T}}$

$\tilde{T}$: I: $-\int (\tilde{w}^+)^* \frac{\bar{\mu}_T\bar{w}_{yy}}{Re}\tilde{T}\,dy = -\int \tilde{T}\frac{\bar{\mu}_T\bar{w}_{yy}}{Re}(\tilde{w}^+)^*\,dy$

II: $-\int (\tilde{w}^+)^* \frac{\bar{\mu}_{TT}\bar{T}_y\bar{w}_y}{Re}\tilde{T}\,dy = -\int \tilde{T}\frac{\bar{\mu}_{TT}\bar{T}_y\bar{w}_y}{Re}(\tilde{w}^+)^*\,dy$

III: $-\int (\tilde{w}^+)^* \frac{\bar{\mu}_T\bar{w}_y}{Re}D\tilde{T}\,dy$ Integrations by parts:

$\hookrightarrow -(\tilde{w}^+)^*\frac{\bar{\mu}_T\bar{w}_y}{Re}\tilde{T}\Big|^{y0} + \int \tilde{T}\left\{\frac{\bar{\mu}_T\bar{w}_y}{Re}D(\tilde{w}^+)^* + (\tilde{w}^+)^*\frac{\bar{\mu}_T\bar{w}_{yy}}{Re} + (\tilde{w}^+)^*\frac{\bar{\mu}_{TT}\bar{T}_y\bar{w}_y}{Re}\right\}dy$

So for $(\tilde{w}^+)^*$: $A_{45} = -\frac{\bar{\mu}_T\bar{w}_{yy}}{Re} - \frac{\bar{\mu}_{TT}\bar{T}_y\bar{w}_y}{Re}$

$(\tilde{T})$

$+\frac{\bar{\mu}_T\bar{w}_y}{Re}D + \frac{\bar{\mu}_T\bar{w}_{yy}}{Re} + \frac{\bar{\mu}_{TT}\bar{T}_y\bar{w}_y}{Re}$

$B_{45} = 0$